A COUPLED HYGROTHERMAL COHESIVE LAYER MODEL FOR SIMULATING DEBOND GROWTH IN BIMATERIAL INTERFACE

By

YONG WANG

Bachelor of Science
Tsinghua University
Beijing, China
1986

Master of Science
Tsinghua University
Beijing, China
1989

Submitted to the Faculty of the
Graduate College of the
Oklahoma State University
in partial fulfillment of
the requirements for
the Degree of
DOCTOR OF PHILOSOPHY
July, 2006

A COUPLED HYGROTHERMAL COHESIVE
LAYER MODEL FOR SIMULATING
DEBOND GROWTH IN
BIMATERIAL
INTERFACE

Thesis Approved:

Thesis Adviser

Dean of the Graduate College

ACKNOWLEDGMENTS

I would like to express my sincere thanks to my advisor, Professor Samit Roy, for his supervision, constructive guidance, financial support and inspiration throughout the study. His profound contribution to my development, professional and otherwise, is deeply appreciated. My appreciation extends as well to the members of my supervisory committee Dr. Hongbing Lu and Dr. Andrew S. Arena, Jr. from Department of Mechanical and Aerospace Engineering, Dr. Roger Zierau from Department of Mathematics, and to the faculty of the Department of Mechanical and Aerospace Engineering.

I also would like to express my thanks to Professor Kenneth M. Liechti and his group member Dr. Soojae Park and Mr. Dewei Xu from The University of Texas at Austin for providing test data and valuable suggestions for this study.

I wish to express my sincere gratitude to my parents for their unconditional love and confidence in me all the time.

This dissertation is dedicated to my beloved wife Bo Lan and my daughter Hongfan Wang, without their love and support this work would have not been possible. I would like to thank them for their consistent encouragement and love, and for all that they have given to me in my life.

Finally, the financial support of the National Science Foundation (Grant No. CMS-0296167) is acknowledged with thanks.

TABLE OF CONTENTS

Chapter Page

LIST OF TABLES

Table Page

LIST OF FIGURES

Figure Page

NOMENCLATURE

σ_{ij}	Stress component (Pa)
ε_{ij}	Strain component
σ	Normal stress (Pa)
τ	Shear stress (Pa)
$\sigma_{\max}$	Maximum normal stress in cohesive layer (Pa)
$\tau_{\max}$	Maximum shear stress in cohesive layer (Pa)
$\varepsilon_{\max}$	Maximum normal strain in cohesive layer
$\gamma_{\max}$	Maximum shear strain in cohesive layer
h_c	Cohesive layer thickness (m)
ϕ_{sep}	Cohesive layer work-of-separation (J/m^2)
G	Strain energy release rate (J/m^2)
E	Young's modulus (Pa)
υ	Poisson's ratio
ρ	Material density (Kg/m^3)
ψ	Helmholtz free energy (J/m^3)
m	Moisture concentration (Kg/m^3)

Γ	Fracture energy (J/m^2)
$\boldsymbol{R}$	External nodal force vector (N)
$\boldsymbol{F}$	Internal nodal force vector (N)
$\boldsymbol{M}$	Mass matrix
$\boldsymbol{K}$	Stiffness matrix
Δt	Time step (sec)
$\boldsymbol{D}$	Elasticity matrix
$\boldsymbol{D}_{ep}$	Elasto-plastic stiffness matrix
c_{ys}	Yield stress (Pa)
H'	Strain hardening function (Pa)
$\bar{\varepsilon}_p$	Equivalent plastic strain
$\bar{c}$	Equivalent stress (Pa)
J_i	Stress invariant
J_i'	Deviatoric stress invariant

CHAPTER I

INTRODUCTION

1.1 Applications of Adhesive Material

The use of structural adhesives is rapidly increasing as they offer distinct advantages over conventional mechanical fastening technique. Laminated composites and thin film structures are some of the most popular applications in industry. Fiber reinforced polymer (FRP) composite is a new application of cohesive material in industry and civil engineering. It is necessary to better understand the nature and the reliability of the bonding between the layers or at the bimaterial interface. Many polymeric materials, including structural adhesives, exhibit nonlinear and time-dependent behaviors and quite sensitive to the change of temperature and moisture penetrant concentration. Therefore the load-carrying requirements of the cohesive layer, time-dependent material properties, and coupled hygrothermal effect in the adhesive layer, stress concentration and non-linear deformation near the crack tip, crack initiation and propagation (debond) within the interface between two materials are some of the essential factors that should be considered to get a reliable solution.

Fiber reinforced polymers are a class of advanced composite materials that have been extensively used as lightweight, performance-enhancing materials in aerospace, automobile, and defense industries for quite some time. Over the past few years there has been extensive research into their potential applications in the construction industry.

However, the actual application of FRP composite in civil engineering sector has been slow especially as concrete reinforcement. One of the chief reasons for their slow acceptance is because of a lack of reliable predictive models and sound design guidelines for their use in civil infrastructure applications.

One promising prospect of the application of FRP composite materials in civil engineering is infrastructure repair and retrofit. FRP materials have been used to strengthen the concrete beam element of buildings and bridges with low cost and high strengthening effect [1]. This allowed increasing the strength and/or ductility of these structures while benefiting from the FRP material advantages including: ease of application, high strength-to-weight ratio, and excellent resistance against corrosion and chemical attacks. Ritchie et al. [2] studied the behavior of concrete beams strengthened by bonding FRP (glass, carbon, and aramid) plates to the tension zone and showed that FRP reinforcement increased beam stiffness by 17-79% and beam ultimate strength by 40-97%. New uses of FRP sheets to upgrade the resistance of steel structures have recently been studied. A considerable increase in the strength and stiffness of the rehabilitated steel bridge girders was observed [3]. A major concern for such retrofitting is the debonding of polymeric adhesive that could compromise the reinforcing effect of the FRP. When exposed to harsh environments, degradation of the adhesive bond could lead to delamination of the FRP reinforcement that could ultimately lead to catastrophic failure.

Thin film structure appears mainly as coating in a wide variety of applications and in multilayer structures in microelectronic devices and package. Since poor bonding results in crack or delamination, fracture mechanics is a natural approach for

characterizing the resistance to failure and making durability or reliability prediction. At the same time, several experimental methods, including peel test, blister test, indentation test, and scratch test etc., have been used to determine the interfacial bond strength or toughness. One problem common to all of these methods is that global plastic dissipation makes it difficult to extract the true toughness of the interface. A new test method, peninsula blister test, can minimize the plastic dissipation and hence be an effective approach to measure the fracture toughness of the thin film structures.

Laminated composites have the advantage of low weight and high strength compared to the structural metals, and hence obtain an increasing application in aerospace industry. Delamination, which is created when two layers debond from each other, is a common type of failure mode in layered composites without the through-the-thickness reinforcement. The initiation of delamination growth is usually controlled by mode I and mode II fracture toughness. Numerical approach with mixed mode failure criterion is an effective way to investigate the delamination of the layered composites.

1.2 Cohesive Zone Model

An important issue when considering failure is the observation that most engineering materials are not perfectly brittle in the Griffith sense but display some ductility after reaching the strength limit. In fact, for most engineering materials there exists a small zone in front of the crack tip, in which small-scale yielding, micro cracking and void initiation, growth and coalescence take place. If this fracture process zone is sufficiently small compared to the structural dimensions, linear-elastic fracture mechanics concept can apply. However, if this is not the case, the cohesive forces that exist in this

fracture process zone must be taken into account. The most powerful and natural way is to use cohesive zone model, which was introduced by Barenblatt [4] and Dugdale [5] for elastic-plastic fracture in ductile metals, and for quasi-brittle materials by Hillerborg et al. [6] in his so-called fictitious crack model.

The fracture process zone approach of Needleman [7, 8] and Tvergaard and Hutchinson [9, 10] involves attributing a prescribed traction-separation law to the interface and, because it allows crack growth to occur, the associated plastic dissipation from loading and unloading of points that are passed by the crack front is rigorously accounted for. As a result, the selected traction-separation law determines the work-of-separation (or adhesive fracture energy), which is the work required to create a unit area of fully developed crack [11].

In the past two decades or so, cohesive zone models have become very popular and have been recognized to be an important tool for describing fracture in engineering materials. Especially when the crack path is known in advance, either from experimental evidence or because of the structure of the material (such as in laminated composites), cohesive zone model has been used with great success. Song and Waas [12], Shawan and Waas [13], and El-Sayed and Sridharan [14] successfully employed cohesive zone model to investigate the fracture properties in laminated composites. In those cases, the finite element mesh was constructed such that the known crack path coincides with the element boundaries.

The most common failure form of FRP composite plate bonded concrete structure is the delamination of the FRP plate from the concrete component. The debond process of FRP plate usually initiates and propagates along the adhesive-concrete or adhesive-FRP

interface, which is known in advance. The cohesive zone model is thus a good tool for investigation of local fracture processes in FRP delamination.

Fatigue crack growth is traditionally characterized via linear elastic fracture mechanics concepts where crack growth rates are correlated with the change in energy release rate or the maximum value of the energy release rate in a cycle. This approach has worked well for metals and polymers alike, especially in dry, room temperature environments, where conditions are still generally linearly elastic. Correlation between crack growth rates and elastic fracture parameters do become suspect in polymers near their glass transition and when saturated by a solvent. Cohesive zone modeling offers a solution to this difficulty in the sense that if the near-tip damage can be accounted for in the traction-separation law of the interphase then the local non-linear inelastic behavior of the material can be coupled into any analysis directly [15].

1.3 Coupled Hygrothermal Effect on Cohesive Layer

Moisture can cause a host of reliability problems at interfaces including interface bond degradation and debonding. Two mechanisms can be identified. First, moisture at an interface can reduce the interface bonding strength dramatically by altering the chemical bonds. Second, when an interface with a crack or a crack-like defect is under tensile stress, stress corrosion may allow crack growth at stresses much lower than critical fracture would require [16].

The influence of moisture diffusion on crack growth along an interface is not yet fully understood. Environmental cracking in a polymer typically occurs in the presence of a penetrant, such as moisture, and mechanical strain. It has been postulated that the

mechanism involved in environmental crack growth in a polymer involves a small zone of craze formation and/or plasticization at the crack tip. For thermoset resins, such as epoxy, energy absorption at the crack tip is primarily by a shear yielding process and not by crazing. Consequently, for a thermoset epoxy, the zone of plasticization ahead of the crack tip must be determined using a diffusion law for non-porous media, such as Fick's law. However, quite frequently, polymer composites exhibit deviations from the classical Fickian treatment, termed as anomalous or non-Fickian diffusion, especially at elevated temperatures and stress levels, and at high relative humidity. Sophisticated hygrothermal models have been developed and verified by Roy [17-20] to account for anomalous diffusion.

1.4 Cohesive Layer Model

Cohesive layer model employs a thin layer of material, which is placed between two adjacent layers for laminated structures and multi-layer structures, or along the bimaterial interface, or along a predicted cracking path in a single material (e.g. concrete and metal) to simulate the elastic-plastic failure in ductile or quasi-brittle material in the vicinity of the debond tip. It allows debond (or failure) to initiate and grow in these elements along a prescribed debond path. The vicinity of debond tip can be divided into three characteristic zones: elastic zone, damage zone, and debonded zone. The corresponding stress-strain traction-separation relation may take different forms in each zone for different materials, different loading and environmental conditions to cope with any particular nonlinear behavior in front of the debond tip.

The thickness of cohesive layer is an important parameter in the cohesive layer model. It should be noted that the cohesive layer thickness is not arbitrary in cohesive layer model, and it is related to some characteristic length-scale of the debond process, such as crack opening displacement (COD). Cohesive layer thickness can be determined from the maximum deformation at the debond tip and the maximum strain $\varepsilon_{\max}$ in cohesive layer at failure.

Environmental degradation is usually found in adhesive material and therefore results in the change of the material properties such as $\varepsilon_{\max}$ and $c_{\max}$ (maximum stress) When investigating the moisture degradation, two-dimensional and three-dimensional moisture diffusion in the cohesive layer can be directly simulated in a two-dimensional or three-dimensional cohesive layer. Mixed mode I and mode II fracture is the common failure form of cohesive layer and sometimes even includes mode III. Mixed mode failure and corresponding failure criteria can also be easily implemented in cohesive layer model to predict the debond process in adhesive layer.

1.5 Objective and Contents

The objective of this research is to construct a cohesive layer model from fundamental principles of continuum mechanics and thermodynamics, take into account the strain rate dependent material properties, non-Fickian Hygrothermal effects as well as diffusion-induced degradation in the cohesive layer. By means of the cohesive layer model, the effect of rate-dependent material properties, environmental degradation of the adhesive material, dynamic response involving material and geometric nonlinearity under blast load, quasi-static debond initiation and propagation of the adhesive layer were

studied to provide a better understanding of the strengthening effect and reliability of FRP plated structures.

In Chapter I, a brief literature review of the application and research status of structural adhesive and FRP bonded structure, and the motivations of this research are presented.

In Chapter II, two-dimensional and three-dimensional cohesive layer constitutive models with prescribed traction-separation laws were constructed from fundamental principles of continuum mechanics and thermodynamics. Based on debond tip deformation, work-of-separation or strain energy release rate, criteria for mixed mode I and mode II debond (and even includes mode III) were developed to predict the debond initiation and propagation of the cohesive layer.

In Chapter III, an analytical solution was derived by introducing a correction term into the original Williams' solution to predict the transverse stress in a cohesive layer when considering the deformation of a stiff substrate. Implementation of the cohesive layer model into a test-bed finite element code was carried out and code verification was performed. Benchmark comparisons of finite element prediction of both global critical load and local stress field with analytical solution for a DCB specimen resulted in good agreement after modifications were made to the original Williams' solution. A sensitivity study was conducted to evaluate the influence of cohesive layer thickness on local parameters such as damage zone length, and global parameter such as critical force.

In Chapter IV, a two-dimensional cohesive layer constitutive model involving strain dependent, non-Fickian hygrothermal effects as well as diffusion induced degradation in the cohesive layer was constructed. Numerical simulation of a wedge-test

including debond growth caused by synergistic interactions between local stress and diffusing moisture was also presented to demonstrate the ability of the cohesive layer model to simulate environmental cracking.

In Chapter V, a three-dimensional cohesive layer model and corresponding mixed mode failure (debond) criterion were implemented in a test-bed finite element code to simulate the full three-dimensional peninsula blister test. Issues such as large deformation, time-dependent material behavior, and residual stresses in the thin film were considered in the simulation model. Distinctive numerical techniques were successfully employed to simulate the unique liquid loading process. FEA simulation results were also compared with analytical solution and test data. Good agreement was obtained.

In Chapter VI, cohesive layer model with strain-rate dependent traction-separation constitutive law was implemented in a test-bed FEA code to simulate a moving wedge test. Time-dependent material properties of the adhesive material were considered and quasi-static debond growth of the adhesive layer was successfully simulated by this code. Results predicted by the computational model were benchmarked through comparison with analytical solutions and mixed mode fracture tests.

In Chapter VII, cohesive layer model was used to study the dynamic response of a FRP bonded concrete beam under blast loading. Implicit Hilber-Hughes-Taylor (HHT) method was employed in the model to allow better control of numerical damping. Long term and short term responses were obtained and their effects on the failure of the adhesive layer were investigated. Dynamic responses of the structure with an initial crack and its effect on debond initiation were also studied.

In Chapter VIII, a two-dimensional implicit dynamic finite element formulation including material and geometric nonlinearity was derived and implemented into a test-bed FEA code. Model verification under very large deformation was successfully performed through comparison with ABAQUS FEA predictions. Subsequently, the NOVA-3D FEA model was applied to a circular steel plate with a polymer coating subjected to intensive blast loading, and the effect of polymer coating on the nonlinear dynamic response was numerically investigated.

In Chapter IX, conclusions are presented based on the study of the cohesive layer model and its applications on various engineering structures.

CHAPTER II

COHESIVE LAYER MODEL

This chapter gives a detailed description of the cohesive layer model for two-dimensional and three-dimensional cases. It includes the definition of cohesive layer, the constitutive laws for the cohesive layer, the concept of work-of-separation, and the mixed mode failure criteria.

2.1 Cohesive Layer Configuration

Ductile polymeric adhesive materials usually have a nonlinear normal and shear stress-strain response. In the event of crack initiation and propagation in such polymeric materials, there exists a damage zone ahead of the debond tip, in which, craze and void initiation, growth and coalescence take place. The cohesive forces in the damage region must be taken into account to capture the behavior of the failing material in this zone, especially if the zone size is not sufficiently small compared to characteristic structural dimensions. The vicinity of debond tip can be divided into three common zones: an elastic/viscoelastic zone, a damage zone, and a debonded zone, as depicted in Fig. 2-1(a). The corresponding stress-strain (or traction-separation) relation may take different nonlinear forms in each zone for different materials and different loading conditions.

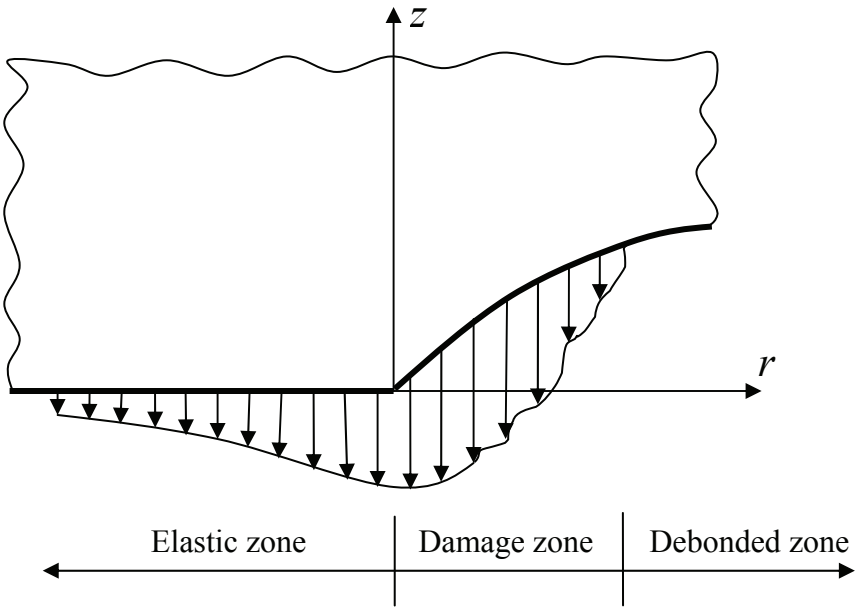

(a) Debond tip traction force

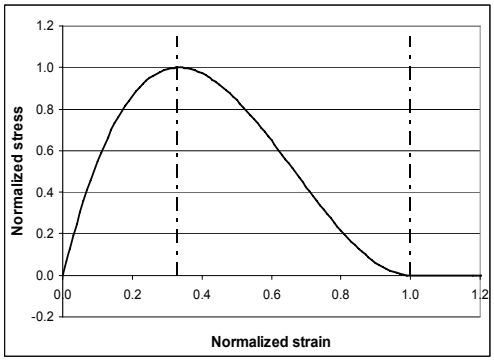

(b) Traction-separation law near debond tip

Fig. 2.1 Three characteristic zones near debond tip
and corresponding stress-strain relations

In order to model this nonlinear behavior near the debond tip, a cohesive layer, which is a thin layer of cohesive finite elements, can be placed between two adjacent layers for laminated structures and multi-layer structures, or along the bimaterial interface, or along a predicted cracking path in a single material (e.g. concrete and metal). It allows debond (or failure) to initiate and grow in these elements and different stress-

strain traction-separation laws can be selected to cope with any particular nonlinear behavior in front of the debond tip. An example of the traction-separation law for a cohesive layer is shown schematically in Fig. 2-1(b).

The thickness, h_c, of cohesive layer is an important parameter in the cohesive layer model. It is not arbitrary, but is directly related to a characteristic length parameter (δ), such as crack opening displacement (COD). In this simulation, $\delta = h_c \varepsilon_{\max}$ and $\varepsilon_{\max}$ is the maximum strain that could be reached at debond tip. Environmental degradation in cohesive material is included in the cohesive layer model through the change of the material properties $c_{\max}$ and $\varepsilon_{\max}$. When investigating the moisture induced degradation, two-dimensional and three-dimensional moisture diffusion in the cohesive layer can be directly simulated. Mixed mode failure and corresponding failure criteria can also be easily established to predict the debond process.

2.2 Cohesive Layer Constitutive Equations

2.2.1 Triangular Stress-Strain Traction-Separation Law

Triangular stress-strain traction-separation law is a simple and commonly used model for cohesive material (Fig. 2-2), especially in theoretical analysis. Considering the stress and strain of mode I debond (opening mode) in the direction perpendicular to the debond surface, three types of zone are defined as follow:

Elastic zone: when the transverse strain $\varepsilon \le \frac{\varepsilon_{\max}}{3}$, stress linearly increases with strain, stress reaches its maximum value $c = c_{\max}$ at $\varepsilon = \frac{\varepsilon_{\max}}{3}$.

Damage zone: when the transverse strain $\varepsilon > \frac{\varepsilon_{\max}}{3}$, stress decreases gradually from its maximum to zero as strain approaches $\varepsilon_{\max}$.

Debond (failure) zone: when the transverse strain $\varepsilon > \varepsilon_{\max}$, stress remains zero which implies a full debond or separate of the cohesive layer.

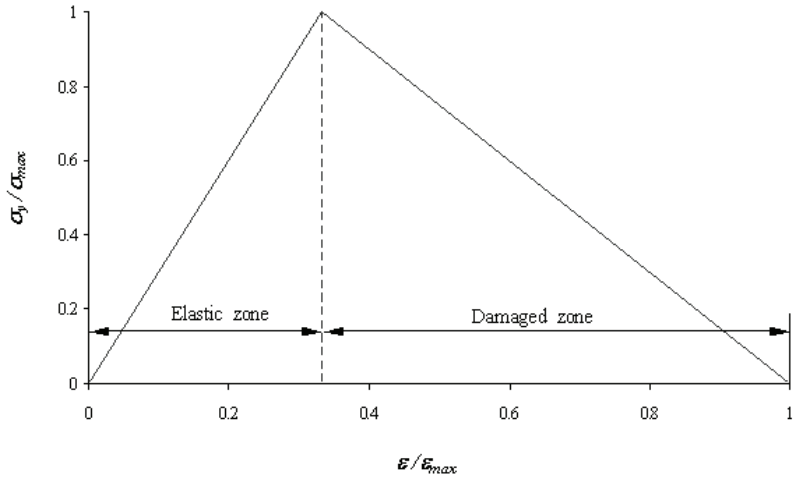

Fig. 2-2 Normalized triangular stress-strain traction-separation law for a cohesive layer

The maximum stress $\sigma_{\max}$ and maximum strain $\varepsilon_{\max}$, which are material properties, are functions of time, strain rate, temperature and moisture concentration etc., and represent the prescribed maximum stress and strain that could be reached in cohesive layer when the cohesive layer debonds along a specified direction.

2.2.2 2-D Cubic Stress-Strain Traction-Separation Law

Based on fundamental principles of continuum mechanics, for two-dimensional case, a more accurate cohesive layer constitutive relationship takes the cubic form as

employed by Needleman [7] (Fig. 2-3). In the direction perpendicular to the debond surface, the transverse normal stress is given by,

$$\sigma_{22} = \begin{cases} \frac{27}{4}\sigma_{\max}(\bar{\varepsilon}_{22} - 2\bar{\varepsilon}_{22}^{\,2} + \bar{\varepsilon}_{22}^{\,3}) & 0 \le \bar{\varepsilon}_{22} \le 1 \\ 0 & \bar{\varepsilon}_{22} > 1 \\ \frac{27}{4}\frac{\sigma_{\max}}{\varepsilon_{\max}}\varepsilon_{22} = \frac{27}{4}\sigma_{\max}\bar{\varepsilon}_{22} & \bar{\varepsilon}_{22} < 0 \end{cases} \tag{2-1}$$

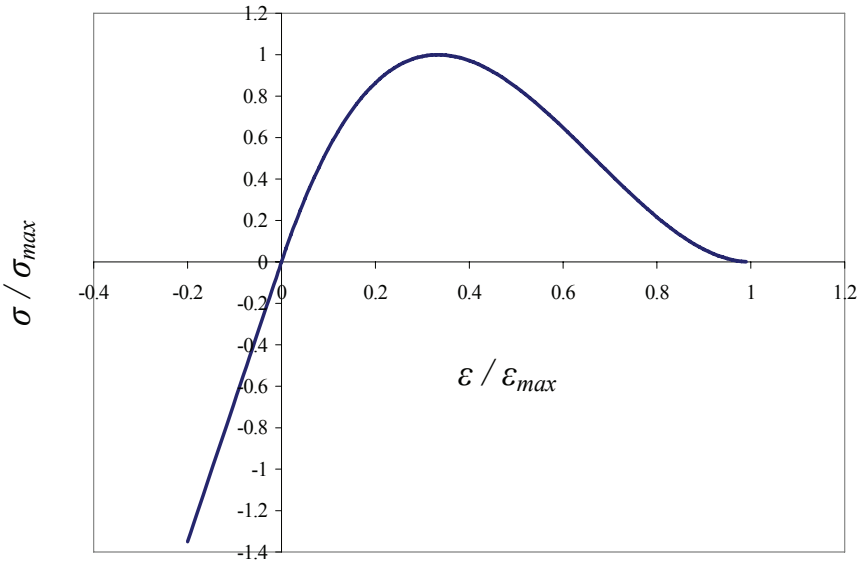

Fig. 2-3 Cubic stress-strain traction-separation law for a cohesive layer

In the direction of debond growth, linear elastic response is assumed, and the axial normal stress is given by,

$$\sigma_{11} = \frac{c_{\max}}{\varepsilon_{\max}}\varepsilon_{11} = \sigma_{\max}\bar{\varepsilon}_{11} \tag{2-2}$$

where, the normalized strain in a given direction is defined as $\bar{\varepsilon}_{ii} = \dfrac{\varepsilon_{ii}}{\varepsilon_{\max}}$ (no sum on *i*).

A similar treatment to the one developed in Eq. (2-1) is prescribed for the shear σ_{12} response, with the proviso that the shear stress is independent of the sign of shear strain.

2.2.3 3-D Cubic Stress-Strain Traction-Separation Law

Three-dimensional cohesive layer treatment is often necessary for some structures like peninsula blister specimen, which is used to measure the interfacial fracture toughness in thin film structures. A full three-dimensional cohesive layer model was constructed in this study to meet this requirement. By extending the above two-dimensional cohesive layer model just described, the constitutive law for a three-dimensional cohesive layer can be expressed in a similar manner as shown in Eqs. (2-3) and (2-4). Again, nonlinear responses are considered for transverse stress components c_{31}, c_{32}, and c_{33}, while for other stress components linear elastic response is assumed.

$$\sigma_{3i} = \begin{cases} \frac{27}{4}\sigma_{\max}(\bar{\varepsilon}_{3i} - 2\bar{\varepsilon}_{3i}^{\,2} + \bar{\varepsilon}_{3i}^{\,3}) & 0 \le \bar{\varepsilon}_{3i} \le 1 \\ 0 & \bar{\varepsilon}_{3i} > 1 \\ \frac{27}{4}\sigma_{\max}\bar{\varepsilon}_{3i} & \bar{\varepsilon}_{3i} < 0 \end{cases} \qquad (i = 1,\ 2,\ 3) \tag{2-3}$$

$$\sigma_{jk} = \frac{\sigma_{\max}}{\varepsilon_{\max}}\varepsilon_{jk} = \sigma_{\max}\bar{\varepsilon}_{jk} \qquad (j,\ k = 1,\ 2) \tag{2-4}$$

2.3 Cohesive Layer Work-of-Separation

For a given stress-strain traction-separation law, the work-of-separation (or strain energy) is the work needed to fully separate a unit area of cohesive layer, which is given by the total area under the prescribed stress-strain curve.

Under the triangular stress-strain traction-separation law as shown in Fig. 2-2, for pure mode I debond,

$$\phi_{sep}^{I} = h_c \int_0^{\sigma_{\max}} \sigma(\varepsilon) d\varepsilon = \frac{1}{2} \sigma_{\max} \varepsilon_{\max} h_c \tag{2-5}$$

and for pure mode II debond,

$$\phi_{sep}^{II} = h_c \int_0^{\gamma_{\max}} \tau(\gamma) d\gamma = \frac{1}{2} \tau_{\max} \gamma_{\max} h_c \tag{2-6}$$

Similarly, under the cubic stress-strain traction-separation law as shown in Fig. 2-3,

$$\phi_{sep}^{I} = h_c \int_0^{\sigma_{\max}} \sigma(\varepsilon) d\varepsilon = \frac{9}{16} \sigma_{\max} \varepsilon_{\max} h_c \tag{2-7}$$

$$\phi_{sep}^{II} = h_c \int_0^{\gamma_{\max}} \tau(\gamma) d\gamma = \frac{9}{16} \tau_{\max} \gamma_{\max} h_c \tag{2-8}$$

where h_c is the thickness of the cohesive layer.

2.4 Failure Criteria of Mixed Mode Debond

Mixed mode I and mode II debond is the common failure form of cohesive layer, while pure mode I or mode II debond is only a special case under certain conditions. It is

necessary to establish a failure criterion such that it contains both the contributions of mode I and mode II debond, and in some cases even includes mode III.

2.4.1 Criterion Based on Prescribed Maximum Strain

At the debond tip, when the strains satisfy the following condition, cohesive layer will debond [21],

$$\sqrt{\alpha_1\left(\frac{\varepsilon_y}{\varepsilon_{\max}}\right)^2+\alpha_2\left(\frac{\gamma_{xy}}{\gamma_{\max}}\right)^2}=\delta \tag{2-9}$$

where ε_y and γ_{xy} are the transverse normal strain and shear strain respectively, $\varepsilon_{\max}$ and $\gamma_{\max}$ are the prescribed normal and shear failure strains of the cohesive layer, respectively. α_1, α_2, and δ are constants and $\alpha_1=\alpha_2=\delta=1$ was taken in this study.

2.4.2 Criterion Based on Strain Energy Release Rate

The strain energy release rate in the cohesive layer during mixed mode debond, G, due to the traction-separation force can be partitioned into the opening (mode I) and shear (mode II) components, G_I and G_{II} respectively, in such a way that,

$$G=G_I+G_{II} \tag{2-10}$$

Each individual component can be calculated by integrating the mode I and II traction-separation curves (Fig. 2-4)

$$G_I=\int_0^{\bar{\varepsilon}_t}\bar{\sigma}(\bar{\varepsilon})d\bar{\varepsilon} \tag{2-11}$$

$$G_{II} = \int_0^{\bar{\gamma}_t} \bar{\tau}(\bar{\gamma}) d\bar{\gamma} \tag{2-12}$$

where $\bar{\sigma} = \dfrac{\sigma}{\sigma_{\max}}$, $\bar{\tau} = \dfrac{\tau}{\tau_{\max}}$, $\bar{\varepsilon} = \dfrac{\varepsilon}{\varepsilon_{\max}}$, $\bar{\gamma} = \dfrac{\gamma}{\gamma_{\max}}$ are normalized stresses and strains in the specific directions, respectively.

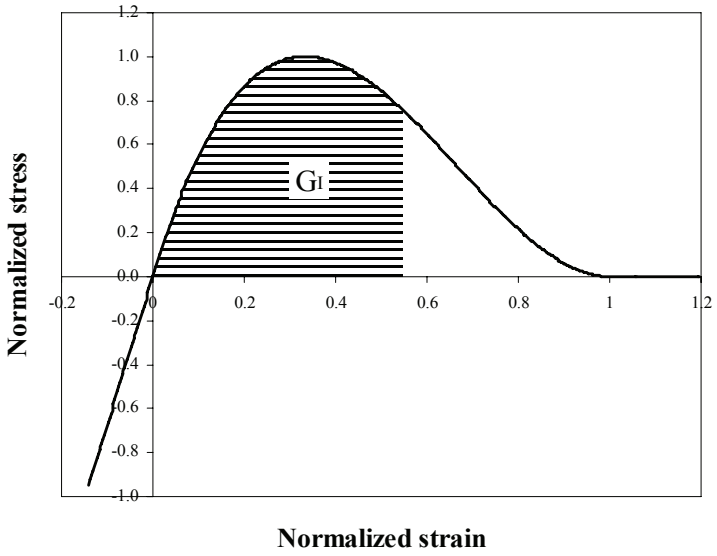

Fig. 2-4 Cubic stress-strain traction-separation law and strain energy release rate for a cohesive layer

Considering the energy required to separate the cohesive layer, the cohesive layer debond process can be better predicted by means of the following criterion

$$\left(\frac{G_I}{G_{I_C}}\right)^m + \left(\frac{G_{II}}{G_{II_C}}\right)^n = e \tag{2-13}$$

where, G_I and G_{II} are the respective values of the ambient energy release rates given by the area under the corresponding stress-strain curves under a given applied loading.

G_{I_C} and G_{II_C} are the critical strain energy release rates in pure mode I and mode II debond, respectively.

m, *n*, and *e* are material constants, Kutlu and Chang [22] found that $m = n = e = 1$ provided the best fit to their experimental data.

When neglecting energy dissipation in the bulk adhesive, critical strain energy release rate of cohesive layer is equal to the work-of-separation ϕ_{sep} (the total area under mode I or mode II traction-separation curves for $0 \leq \bar{\varepsilon} \leq 1$, Fig. 2-4), which is the energy necessary to generate unit debond length (2-D case) or area (3-D case). Thus for the cubic stress-strain traction-separation law, integrating Eq. (2-3) over the limits $[0,\ \bar{\varepsilon}]$ for the case of pure mode I debond and $[0,\ \bar{\gamma}]$ for the case of pure mode II debond,

$$G_I = h_c \int_0^{\varepsilon} \sigma(\varepsilon) d\varepsilon = \frac{27}{4} \sigma_{\max} \varepsilon_{\max} h_c \left(\frac{1}{2} \bar{\varepsilon}^2 - \frac{2}{3} \bar{\varepsilon}^3 + \frac{1}{4} \bar{\varepsilon}^4 \right) \tag{2-14}$$

$$G_{II} = h_c \int_0^{\gamma} \tau(\gamma) d\gamma = \frac{27}{4} \tau_{\max} \gamma_{\max} h_c \left(\frac{1}{2} \bar{\gamma}^2 - \frac{2}{3} \bar{\gamma}^3 + \frac{1}{4} \bar{\gamma}^4 \right) \tag{2-15}$$

And therefore, $G_I \to G_{Ic}$ as $\bar{\varepsilon} \to 1$, and $G_{II} \to G_{IIc}$ as $\bar{\gamma} \to 1$ giving

$$G_{I_C} = h_c \int_0^{\varepsilon_{\max}} \sigma(\varepsilon) d\varepsilon = \frac{9}{16} \sigma_{\max} \varepsilon_{\max} h_c \tag{2-16}$$

$$G_{II_C} = h_c \int_0^{\gamma_{\max}} \tau(\gamma) d\gamma = \frac{9}{16} \tau_{\max} \gamma_{\max} h_c \tag{2-17}$$

For triangular stress-strain traction-separation law, a similar procedure can be applied.

Where, h_c is the cohesive layer thickness. It should be noted that the cohesive layer thickness is not arbitrary in cohesive layer model, and it is related to some

characteristic length-scale of the debond process, such as COD. Determination of cohesive layer thickness from test data will be discussed in a later section.

A phase angle is defined to describe the mode-mix of the failure (debond) in a cohesive layer

$$\phi = \tan^{-1}\left[\left(\frac{G_{II}^{*}}{G_{I}^{*}}\right)^{1/2}\right] \tag{2-18}$$

where G_I^* and G_{II}^* are the strain energy release rates at which debond of cohesive layer initiates.

In the case of the presence of anti-plane shear stress (mode III), the mixed mode debond criterion can be expressed as

$$\frac{G_I}{G_{Ic}} + \frac{G_{II}}{G_{IIc}} + \frac{G_{III}}{G_{IIIc}} = 1 \tag{2-19}$$

and the phase angle between mode I and mode III is given by,

$$\varphi = \tan^{-1}\left[\left(\frac{G_{III}^{*}}{G_{I}^{*}}\right)^{1/2}\right] \tag{2-20}$$

CHAPTER III

DEVELOPMENT OF AN ANALYTICAL SOLUTION FOR COHESIVE LAYER MODEL AND MODEL VERIFICATION

The objective of this chapter is to find an analytical solution to the cohesive damage zone at the interface between a fiber reinforced polymer (FRP) plate and concrete substrate. An analytical solution was derived to predict the stress in cohesive layer when considering the deformation in a stiff substrate. A two-dimensional cohesive layer model with a prescribed stress-strain traction-separation law as described in Chapter II was employed in this study. For comparison purpose, the cohesive layer model was implemented into a test-bed finite element code (NOVA-3D). Detailed benchmark comparisons of analytical results with finite element predictions for a double cantilever beam specimen for model verification were performed and issues related to cohesive layer thickness were investigated. It was observed that the assumption of a rigid substrate in analytical modeling can lead to inaccurate analytical prediction of cohesive damage zone length and stress distribution near debond tip.

3.1 Analytical Solution from Cohesive Zone Model

Williams and Hadavinia [23] used a cohesive zone model with various simple forms of cohesive traction-separation laws to analyze the global features and local stress

distribution of a double cantilever beam specimen (DCB, shown in Fig. 3-1). The DCB specimen is modeled as a cantilever beam with elastic foundation as shown in Fig. 3-2. The deformation of the beam is given by the equation

$$\frac{d^4 v}{dx^4} = \frac{w}{EI} \tag{3-1}$$

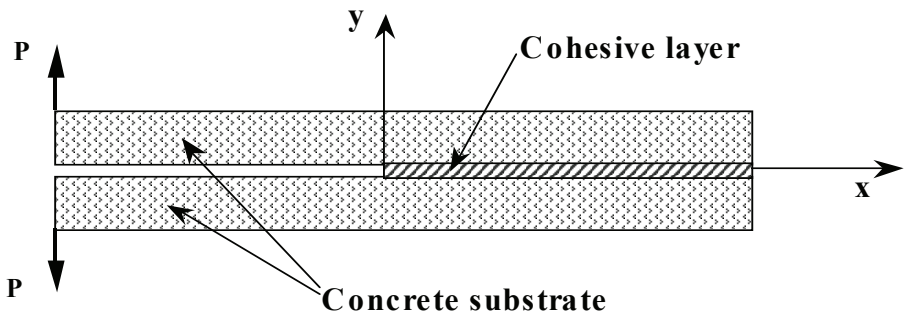

Fig. 3-1 A cohesive layer in a double cantilever beam (DCB)

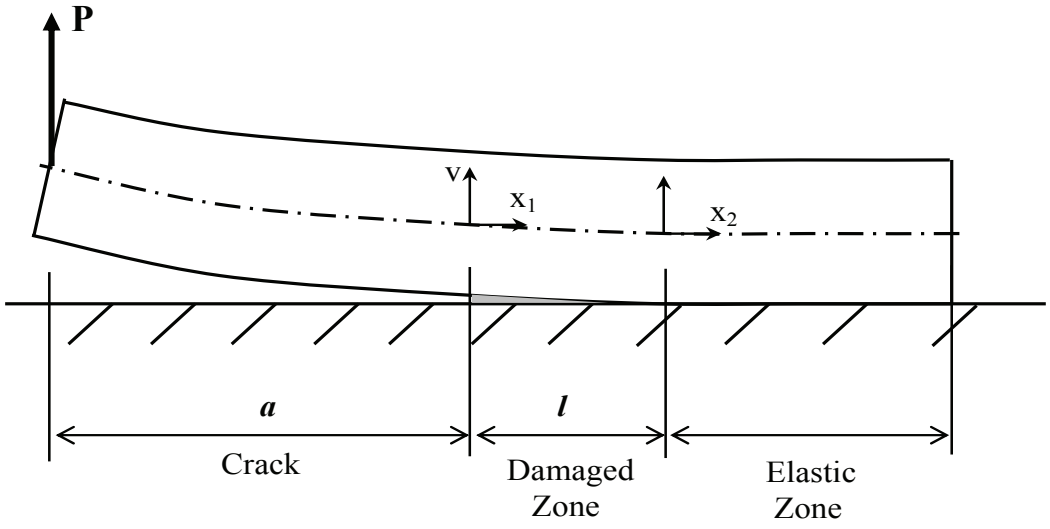

Fig. 3-2 Schematic debonding of a double cantilever beam showing cohesive layer with elastic zone and damage zone ($x_1 \in [0, l]$)

Where E is the Young's modulus of the beam, v is the deflection of beam at its mid-plane, b is the width, and w is the distributed load per unit length of the beam that can be related to the stress in the cohesive layer by $w = -b\sigma_y$.

The stress σ_y in the cohesive zone is modeled by a triangular elastic-linear-damage traction-separation law referring to the stress in the cohesive zone (as depicted in Fig. 2-2), where $v_{\max}$ is the displacement at final fracture, $\sigma_{\max}$ is the maximum stress in the cohesive zone at $v = \frac{v_{\max}}{3}$.

(a) In the damage zone:

$$w = -b\sigma_y = \frac{3b\sigma_{\max}}{2v_{\max}}(v - v_{\max}) \tag{3-2}$$

Let

$$\lambda_1^4 = \frac{3b\sigma_{\max}}{2EIv_{\max}} \tag{3-3}$$

Thus Eq. (3-1) becomes

$$\frac{d^4v}{dx^4} = \lambda_1^4(v - v_{\max}) \tag{3-4}$$

and the corresponding solution is,

$$v = v_{\max} + B_1 \sinh \lambda_1 x_1 + B_2 \cosh \lambda_1 x_1 + C_1 \sin \lambda_1 x_1 + C_2 \cos \lambda_1 x_1 \tag{3-5}$$

(b) In the elastic zone:

$$w = -b\sigma_y = -\frac{3b\sigma_{\max}}{v_{\max}}v \tag{3-6}$$

Let

$$\lambda_2^4 = \frac{3bc_{\max}}{4EIv_{\max}} \tag{3-7}$$

$$\frac{d^4v}{dx^4} = -4\lambda_2^4 v \tag{3-8}$$

and the solution is given by,

$$v = e^{-\lambda_2 x_2}(A_1 \sin \lambda_2 x_2 + A_2 \cos \lambda_2 x_2) \tag{3-9}$$

There are a total six unknown coefficients in Eqs. (3-5, 3-9). Along with the unknown damage length *l* and the critical force P_{cr}, it requires eight boundary conditions to determine the beam deformation and the corresponding stresses in the cohesive layer. Two force boundary conditions are provided by force and moment equilibrium at the crack tip $x_1 = 0$. Continuity conditions imposed at the boundary of the elastic zone and damage zone yield another four boundary conditions by matching v, $\frac{dv}{dx}$, $\frac{d^2v}{dx^2}$, $\frac{d^3v}{dx^3}$ at $x_1 = l$ and $x_2 = 0$. Finally, two displacement boundary conditions are $v = v_{\max}$ at $x_1 = 0$ and $v = \frac{v_{\max}}{3}$ at $x_1 = l$.

From $v_1(0) = v_{\max}$,

$$B_2 + C_2 = 0 \tag{3-10}$$

$\frac{d^2v_1}{dx^2}(0) = \frac{P_{cr}a}{EI}$, where *a* is the crack length

$$B_2 + C_2 = \frac{P_{cr}a}{2EI\lambda_1^2} \tag{3-11}$$

$\frac{d^3v_1}{dx^3}(0) = \frac{P_{cr}}{EI}$

$$B_1 - C_1 = \frac{P_{cr}}{2EI\lambda_1^3} \tag{3-12}$$

$$v_1(l) = \frac{v_{\max}}{3}$$

$$v_{\max} + B_1 \sinh \lambda_1 l + B_2 \cosh \lambda_1 l + C_1 \sin \lambda_1 l + C_2 \cos \lambda_1 l = \frac{v_{\max}}{3} \tag{3-13}$$

$$v_2(0) = \frac{v_{\max}}{3}$$

$$A_2 = \frac{v_{\max}}{3} \tag{3-14}$$

$$\frac{dv_1}{dx}(l) = \frac{dv_2}{dx}(0)$$

$$\lambda_1(B_1 \cosh \lambda_1 l + B_2 \sinh \lambda_1 l + C_1 \cos \lambda_1 l - C_2 \sin \lambda_1 l) = \lambda_2(A_1 - A_2) \tag{3-15}$$

$$\frac{d^2 v_1}{dx^2}(l) = \frac{d^2 v_2}{dx^2}(0)$$

$$\lambda_1^2(B_1 \sinh \lambda_1 l + B_2 \cosh \lambda_1 l - C_1 \sin \lambda_1 l - C_2 \cos \lambda_1 l) = -2\lambda_2^2 A_1 \tag{3-16}$$

$$\frac{d^3 v_1}{dx^3}(l) = \frac{d^3 v_2}{dx^3}(0)$$

$$\lambda_1^3(B_1 \cosh \lambda_1 l + B_2 \sinh \lambda_1 l - C_1 \cos \lambda_1 l + C_2 \sin \lambda_1 l) = 2\lambda_2^3(A_1 + A_2) \tag{3-17}$$

Eqs. (3-10 ~ 3-17) are nonlinear in terms of damage length *l*. Solutions are sought by an iterative numerical predictor-corrector method as follows: Damage length *l* is varied from 0.0 to 1.0 *mm* with interval of 0.001~0.01*mm* for the current specimen, and thereby Eqs. (3-10 ~ 3-16) become a set of linear equations that can be solved to obtain the constants coefficients A_1, A_2, B_1, B_2, C_1, C_2 and the crack initiation load P_{cr} for a specified damage length *l*. These constants and corresponding damage length *l* are then substituted into Eq. (3-17) and, because the equation is not exactly solved, the solution

error is numerically estimated. The correct solution for damage length l and the constants is the one that minimizes the error.

3.2 Analytical Solution from Cohesive Layer Model

In Williams' solution, deformation of the beam transverse to beam axis is neglected, therefore the displacement in y-direction (v) at the centerline of the beam is considered as the deformation of the cohesive zone. Maximum deformation $v_{\max}$ at the debond tip, which is independent of the geometry and material properties of the beam, is the characteristic length scale of the cohesive zone model. When applying cohesive zone approach to a cohesive layer model, maximum deformation can be expressed as $v_{\max} = h_c \varepsilon_{\max}$, where $\varepsilon_{\max}$ is the maximum strain in the cohesive layer at failure, which is assumed to be a material property. As a result, the cohesive layer thickness h_c is no longer arbitrary, but is uniquely determined by the relation $h_c = \frac{v_{\max}}{\varepsilon_{\max}}$. When considering the transverse deformation of the beam, h_c is an important factor in evaluating the relative stiffness of beam and the cohesive layer in the transverse direction.

The Young's modulus of the beam (concrete) is usually much higher than that of the cohesive layer. On the other hand, the thickness of the beam is also much greater than that of the cohesive layer. Consequently the transverse deformation of the beam is comparable to the deformation in the cohesive layer and thus cannot be neglected. A small lateral deformation of the beam will greatly change the stress in the cohesive layer. FEA results clearly show the difference between the deflection of the beam at the

centerline and the deformation of the cohesive layer (that is, the displacement at the beam-cohesive layer interface represents the deformation of the cohesive layer) (Fig. 3-3). As can be seen in Fig. 3-3 the displacement at the interface is generally smaller than the displacement at the centerline of the beam, the latter being the summation of the transverse deformations of the beam and the cohesive layer.

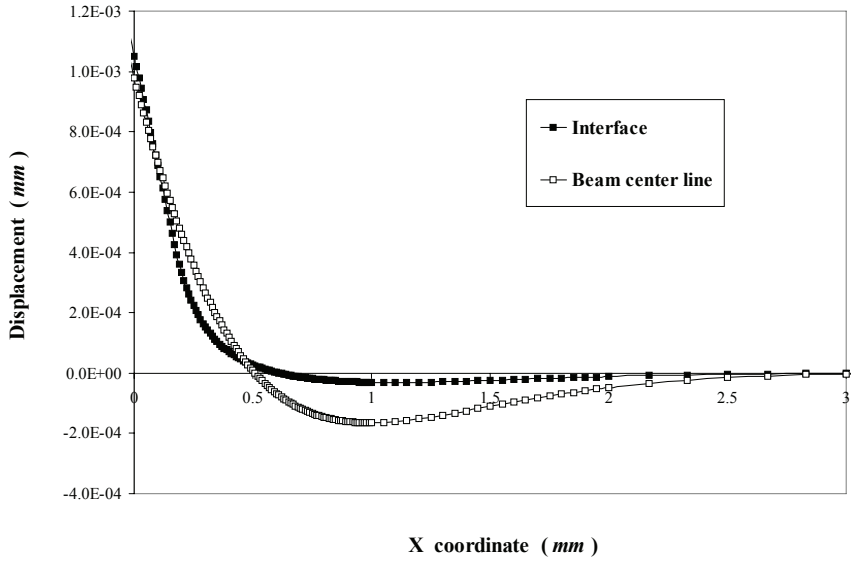

Fig. 3-3 Transverse deformation comparison between beam centerline and cohesive interface using FEA

Thus, the total displacement v in y-direction at the centerline of the beam is composed of two parts: deformation v_b of the beam and deformation v_c of the cohesive layer, such that

$$v = v_b + v_c \tag{3-18}$$

Assume that the transverse stress at the interface and in the cohesive layer is $\sigma_y = \sigma_c$, and $\sigma_y = 0$ at the free top surface of the beam. A distribution law for σ_y

through the height of the beam (h_b) must be assumed to calculate the deformation of the beam (see Fig. 3-4). The actual distribution law for transverse stress can be obtained from elastic FEA analysis. Three idealized distribution laws for σ_y were evaluated in this study:

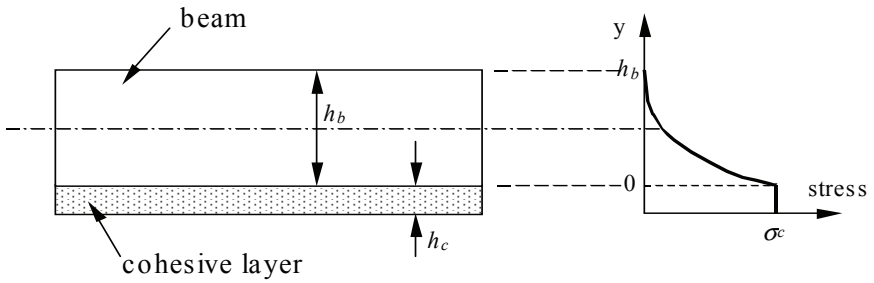

Fig. 3-4 Transverse stress distribution in the beam and cohesive layer

(a) Linear: $\sigma_y = \frac{\sigma_c}{h_b}(h_b - y)$

(b) Quadratic: $\sigma_y = \frac{\sigma_c}{h_b^2}(h_b - y)^2$ (3-19)

(c) Cubic: $\sigma_y = \frac{\sigma_c}{h_b^3}(h_b - y)^3$

The corresponding lateral deformations in the lower half of the beam are, respectively:

(a) Linear: $v_b = \int_0^{h_b/2} \varepsilon_y dy = \int_0^{h_b/2} \frac{\sigma_y}{E_b} dy = \int_0^{h_b/2} \frac{\sigma_c}{E_b h_b}(h_b - y) dy = \frac{3}{8}\frac{\sigma_c h_b}{E_b}$

(b) Quadratic: $v_b = \int_0^{h_b/2} \varepsilon_y dy = \int_0^{h_b/2} \frac{\sigma_y}{E_b} dy = \int_0^{h_b/2} \frac{\sigma_c}{E_b h_b^2}(h_b - y)^2 dy = \frac{7}{24}\frac{\sigma_c h_b}{E_b}$ (3-20)

(c) Cubic: $v_b = \int_0^{h_b/2} \varepsilon_y dy = \int_0^{h_b/2} \frac{c_y}{E_b} dy = \int_0^{h_b/2} \frac{\sigma_c}{E_b h_b^3} (h_b - y)^3 dy = \frac{15}{64} \frac{\sigma_c h_b}{E_b}$

where E_b is the Young's modulus of the beam, and h_b is the height of the beam.

The above results can be generalized as $v_b = k \frac{c_c h_b}{E_b}$, which represents the lateral deformation of the beam, where *k* is the coefficient determined by the distribution of c_y along the *y*-direction within the beam given by Eq. (3-20). From Eq. (3-20), the values of *k* are $\frac{3}{8}$, $\frac{7}{24}$, $\frac{15}{64}$ for linear, quadratic and cubic distributions, respectively.

The analytical solution to the DCB specimen bonded by a cohesive layer with small but finite thickness can now be derived as follows.

(a) In the damage zone:

From Eq. (3-2),

$$v_c = v_{\max} - \sigma_y \frac{2v_{\max}}{3\sigma_{\max}} \tag{3-21}$$

Displacement at the centerline of the beam is

$$v = v_b + v_c = v_{\max} - \sigma_y \left(\frac{2v_{\max}}{3\sigma_{\max}} - k \frac{h_b}{E_b} \right) \tag{3-22}$$

$$\frac{d^4 v}{dx^4} = -\frac{b\sigma_y}{E_b I_b} = (v - v_{\max}) \left[\frac{b}{E_b I_b \left(\frac{2v_{\max}}{3\sigma_{\max}} - k \frac{h_b}{E_b} \right)} \right] \tag{3-23}$$

By defining

$$\lambda_1^4 = \frac{b}{E_b I_b \left(\frac{2v_{\max}}{3\sigma_{\max}} - k \frac{h_b}{E_b} \right)} \tag{3-24}$$

The governing equation becomes

$$\frac{d^4 v}{dx^4} = \lambda_1^4 (v - v_{\max}) \tag{3-25}$$

(b) In the elastic zone:

$$v = v_b + v_c = \sigma_y \left(\frac{v_{\max}}{3\sigma_{\max}} + k \frac{h_b}{E_b} \right) \tag{3-26}$$

$$\frac{d^4 v}{dx^4} = -\frac{b\sigma_y}{E_b I} = -4v \left[\frac{b}{4E_b I_b \left(\frac{v_{\max}}{3\sigma_{\max}} + k \frac{h_b}{E_b} \right)} \right] \tag{3-27}$$

Defining,

$$\lambda_2^4 = \frac{b}{4E_b I_b \left(\frac{v_{\max}}{3\sigma_{\max}} + k \frac{h_b}{E_b} \right)} \tag{3-28}$$

$$\frac{d^4 v}{dx^4} = -4\lambda_2^4 v \tag{3-29}$$

Governing Eqs. (3-25, 3-29) are of a similar form with the original Williams' Eqs. (3-4, 3-8). But the coefficients λ_1 and λ_2 are different because of the presence of the extra term $k\frac{h_b}{E_b}$ which represents the transverse deformation of the beam (note that $k = 0$ gives the original Williams' solution). A solution procedure and boundary conditions similar to the ones used for solving Eqs. (3-4, 3-8) can be employed to solve Eqs. (3-25, 3-29) to determine the unknown constants.

Regarding the boundary conditions for Eqs. (3-25, 3-29), the two force boundary conditions and four displacement continuity conditions are same as the original solution

because these conditions are directly related to the beam. But the two displacement conditions, which are related to the cohesive layer, are a little different.

First, at $x_1 = l$ and $x_2 = 0$, the deformation of cohesive layer v_c (not v at the centerline of the beam) equals $\frac{v_{\max}}{3}$ and the corresponding stress is $\sigma_{\max}$.

$$v_c = v - v_b = \frac{v_{\max}}{3} \tag{3-30}$$

Therefore the corresponding Eqs. (3-13, 3-14) become

$$v_{1c}(l) = \frac{v_{\max}}{3}$$

$$(v_{\max} + B_1 \sinh \lambda_1 l + B_2 \cosh \lambda_1 l + C_1 \sin \lambda_1 l + C_2 \cos \lambda_1 l) - k\frac{\sigma_{\max} h_b}{E_b} = \frac{v_{\max}}{3} \tag{3-31}$$

$$v_{2c}(0) = \frac{v_{\max}}{3}$$

$$A_2 - k\frac{\sigma_{\max} h_b}{E_b} = \frac{v_{\max}}{3} \tag{3-32}$$

On the other hand, at $x_1 = 0$, transverse stress $\sigma_y = 0$ in the concrete beam, so that the lateral deformation of beam $v_b = 0$, therefore $v = v_b + v_c = v_c = v_{\max}$ which is same as Eq. (3-10).

3.3 Comparison between Analytical Solution and FEA Results

A double cantilever beam (DCB) consisting of two substrates bonded with a thin layer of epoxy adhesive is shown in Fig. 3-1. The entire layer of epoxy is modeled with

special cohesive layer elements which obey the prescribed stress-strain traction-separation law. A cohesive layer thickness $h_c = 0.02\ mm$ and beam height $h_b = 1\ mm$ were used in this example, and the initial debond length $a = 15\ mm$ corresponds to the unbonded portion of the beam. Unlike the usual linear elastic fracture mechanics modeling method of a sharp crack tip of zero tip radius, the localized fracture process zone in the current study has a small but finite thickness h_c. Substrate beam is modeled as linear elastic, and the material properties used in this analysis are listed in Table 3-1.

Table 3-1 Material properties for concrete and epoxy adhesive

	Concrete	Epoxy
Young's modulus (*GPa*)	27.5	3.85
Shear modulus (*GPa*)	11.0	1.54
Poisson's ratio	0.25	0.25
$c_{\max}$ (*MPa*)	--	30.0
$\varepsilon_{\max}$	--	0.0526

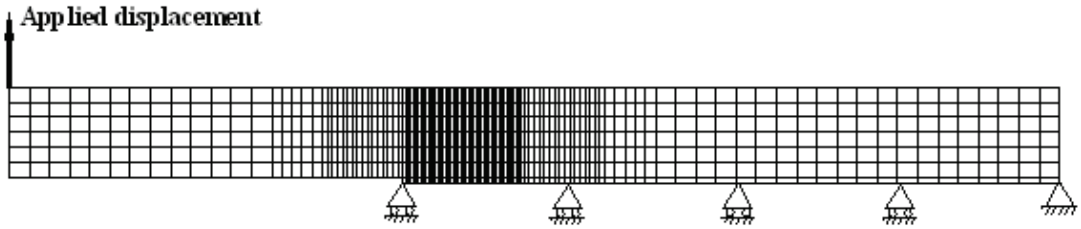

Fig. 3-5 Finite element mesh of a DCB specimen with symmetry boundary conditions

Considering the symmetry boundary conditions along the centerline of epoxy adhesive layer, only half of the DCB specimen is modeled. Fig. 3-5 shows the actual finite element mesh (8-node quadrilateral element) with applied symmetry boundary conditions. A very fine mesh is used to model the sharp stress gradients in the damage region. Plane strain conditions are assumed. Convergence study shows that converged results were obtained when the geometries of the elements in the crack tip area are smaller than $\frac{1}{10}$ of the length of the damage zone.

A constant beam tip displacement (instead of applied force) is specified in the FEA analysis to simulate a wedge test and to ensure that stable debond growth would occur. Debond growth (or cohesive layer element failure) is characterized by the transverse mechanical strain in the cohesive elements exceeding the specified maximum strain $\varepsilon_{\max}$ in the cohesive layer beyond which the transverse stress goes to zero as defined by the cohesive constitutive law depicted in Fig. 2-2. Instead of node release and element deletion schemes used in most finite element codes, a failed element remains active in the subsequent analysis while the stiffness of the element is reduced close to zero.

Analytical results with different *k* values are obtained and compared with numerical results from FEA as shown in Fig. 3-6. It can be seen that the best agreement with the FEA results is reached with the correction coefficient $k = \frac{15}{64}$, which represents a cubic distribution of transverse stress in the beam. This cubic stress distribution is also verified by FEA simulation of the stress field in the concrete beam. The length of damage zone *l* decreases as the *k* increases, which implies a greater transverse deformation in the

beam under the same stress at the interface of beam and the cohesive layer. Due to the complexity of the transverse stress distribution, especially near the crack tip, k may take different values under different combination of material properties and geometries of the concrete beam and the cohesive layer. Further, as shown in Fig. 3-7, the deviation of the FEA results from the analytical solutions within the damage zone is likely attributable to the use of eight-node quadrilateral elements with quadratic interpolation that could result in linear variation of through-thickness strain within the fracture localization zone. Fortunately, the stress distribution in the damage zone does not have a significant effect on the process of debond initiation and propagation in the cohesive layer.

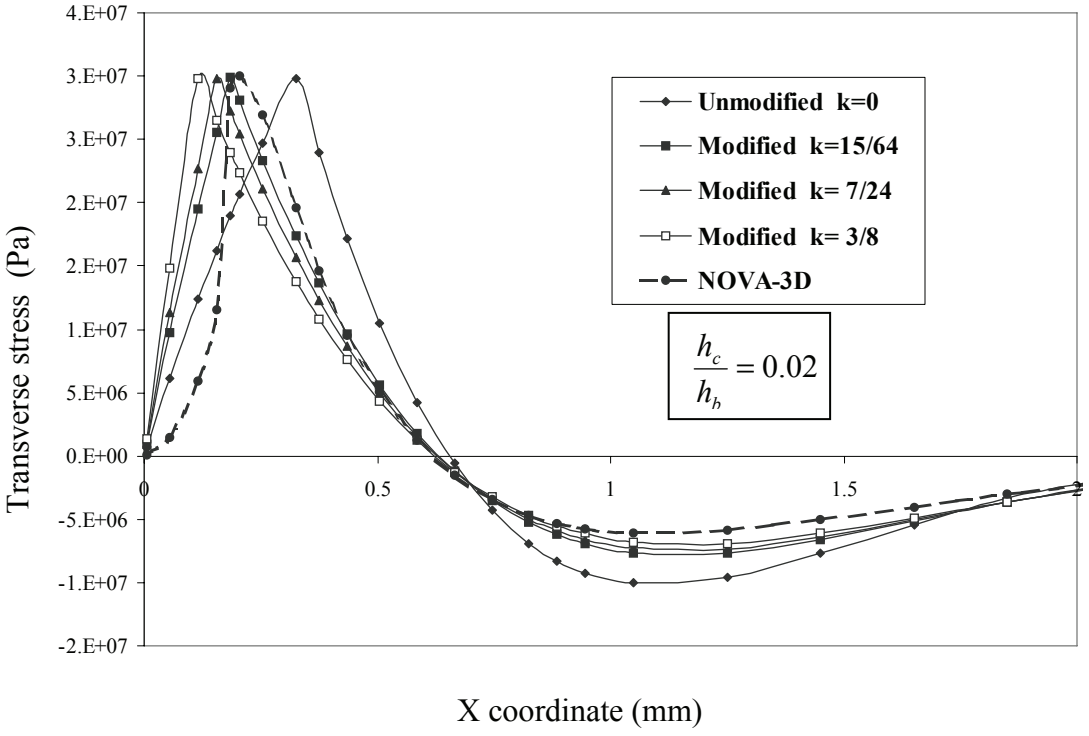

Fig. 3-6 Stress distribution with different correction coefficient k

Furthermore, different cohesive layer thickness and debond lengths were used to verify the agreement between analytical solutions and FEA simulation results, for both global and local metrics as discussed in the following paragraphs.

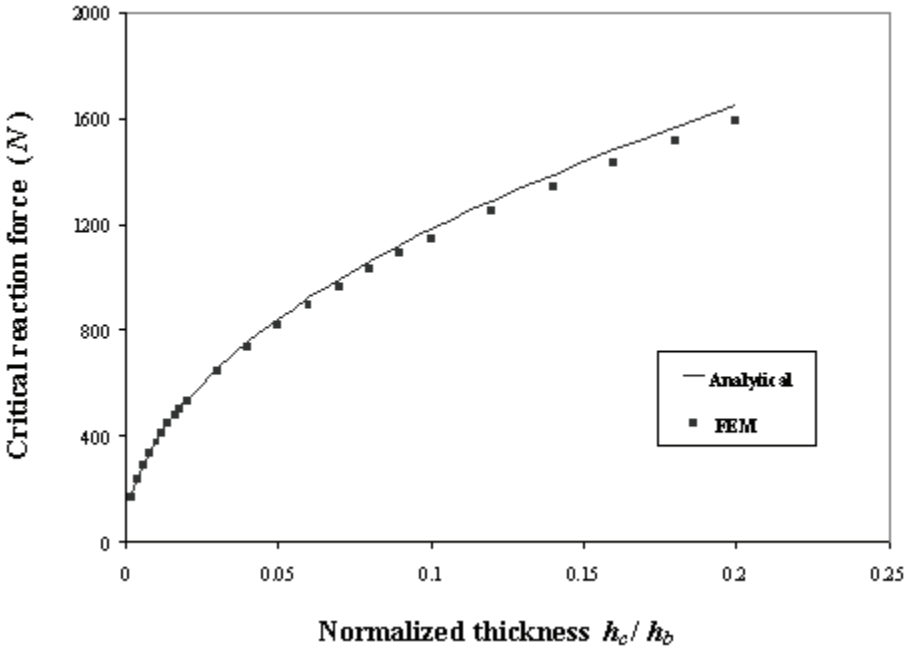

Fig. 3-7 Reaction force comparison for different normalized cohesive layer thicknesses

To study the effect of cohesive layer thickness on a global metric such as critical force (P_{cr}), the comparisons are conducted under the assumption that the cohesive layer deformation at the debond tip is equal to the maximum strain $\varepsilon_{\max}$ of the cohesive layer (critical strain). For most practical cases, the ratio of cohesive layer thickness to beam thickness ($\frac{h_c}{h_b}$) is in the range of 0.02 ~ 0.15. Critical reaction force versus normalized cohesive layer thickness ($\frac{h_c}{h_b}$) is studied and good agreement is obtained between

analytical and FEA solutions. As shown in Fig. 3-7, the critical reaction force by FEA is slightly lower than the analytical predictions. This error is probably due to the fact that at the crack tip ($x_1 = 0$) the transverse displacement at the interface is actually slightly greater than that at the beam centerline (see Fig. 3-3), thereby reducing the reaction force required.

To study the effect of debond length on reaction force, two kinds of boundary conditions are used:

(a) Deformation control: under the same critical deformation at debond tip for FEA and analytical solution

(b) Displacement control: under the same free end displacement for FEA and analytical solution.

Good agreement is observed in both cases as shown in Fig. 3-8.

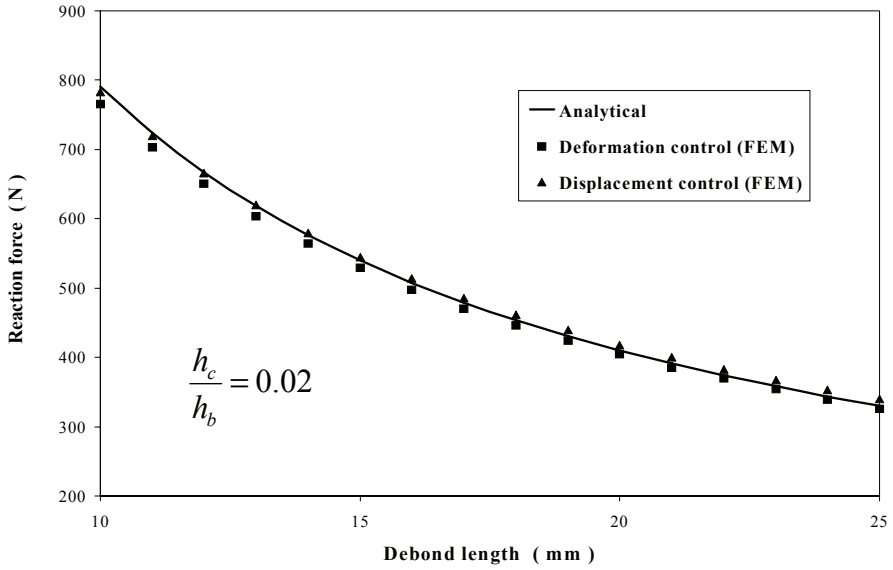

Fig. 3-8 Reaction force comparison for different debond lengths

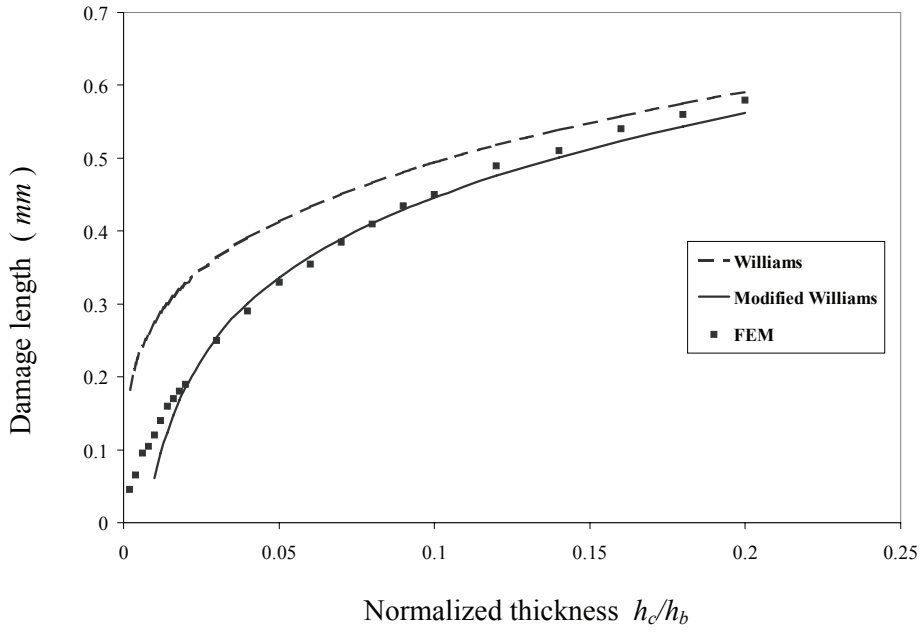

Fig. 3-9 Damage length comparison for different cohesive layer thicknesses

For local stress verifications, cohesive layer stress distribution in crack tip region is determined by evaluating damage length *l*. It can be observed from Fig. 3-9 and from Table 3-2 that the results from FEA are in good agreement with the modified Williams' analytical solution when the normalized thickness lies between 0.02 and 0.15. When $\frac{h_c}{h_b} > 0.20$, that is, when the thickness of cohesive layer is relatively large, the deformation of the beam is relatively small compared with the deformation of the cohesive layer. As a result, the influence of the correction factor is no longer significant and the FEA solution approaches the original (unmodified) Williams' solution. Fig. 3-10 shows how cohesive layer thickness h_c influences local transverse stress distribution near crack tip as characterized by the damage length *l*. Good agreement is observed between analytical prediction and FEA results.

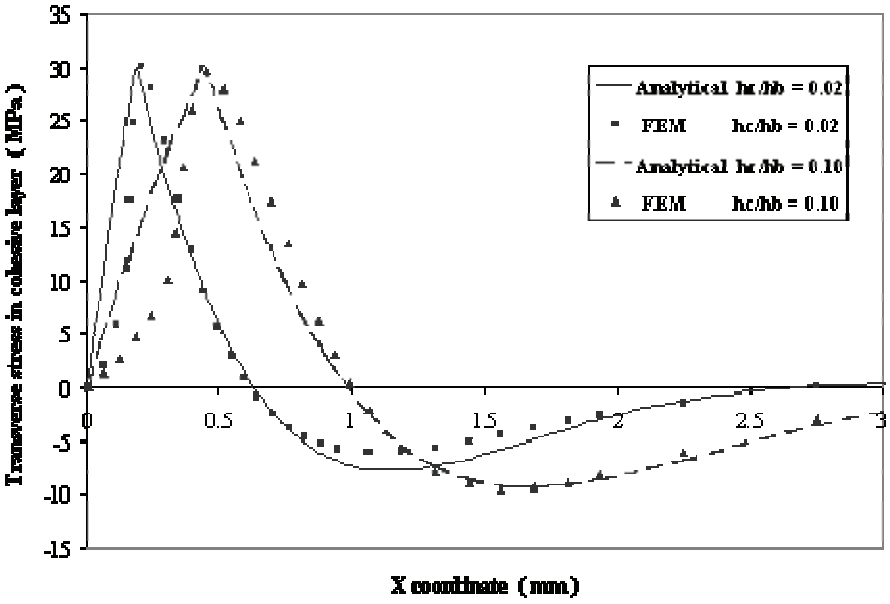

Fig. 3-10 Stress distributions for different cohesive layer thicknesses

Table 3-2 Variation of damage length with different cohesive layer thicknesses

$\frac{h_c}{h_b}$	Damage length (*mm*)		Error (%)
	Analytical	NOVA-3D	
0.02	0.186	0.190	2.15
0.05	0.336	0.332	1.19
0.10	0.446	0.437	2.02
0.15	0.513	0.534	4.09
0.20	0.562	0.587	4.45

It was observed that the modification to Williams' model has little effect on global metrics (i.e. critical force and free end displacement), while for localized damage zone length and local stress distribution the effect of different values of k is significant as

depicted in Fig. 3-6, Fig. 3-9 and Table 3-3. It can be concluded that value of k has significant effect on the damage length, and $k = \frac{15}{64}$ results in the best agreement with FEA for the cohesive layer model with normalized thickness ranging from 0.02 to 0.15. For smaller or larger cohesive layer thickness, the relative lateral deformation of cohesive layer and concrete beam will change significantly. Further analytical studies are necessary to address these specific conditions.

Table 3-3 Analytical and numerical solutions of damage length

Correction factor k	0	15/64	7/24	3/8	FEA
Damage length l (mm)	0.328	0.186	0.156	0.116	0.190

3.4 Conclusions

An analytical solution was derived by introducing a correction term into the original Williams' solution to predict the transverse stress in a cohesive layer when considering the deformation in a stiff substrate. Implementation of the cohesive layer model into a test-bed finite element code was carried out and code verification was performed. Benchmark comparisons of finite element prediction of both global critical load and local stress field with analytical results for a DCB specimen resulted in good agreement after modifications were made to the original Williams' solution. A sensitivity study was conducted to evaluate the influence of cohesive layer thickness on local parameters such as damage zone length, and global parameter such as critical force. From

the present studies it can be concluded that both local and global cohesive layer parameters are fairly sensitive to the cohesive layer thickness, whereas the correction factor (k) to Williams' original solution significantly influences the local stress distribution and damage length.

CHAPTER IV

HYGROTHERMAL EFFECT ON COHESIVE LAYER

The objective of this chapter is to model the synergistic bond degradation mechanism that may occur at the interface between a fiber reinforced polymer (FRP) and concrete. For this purpose, a two-dimensional cohesive layer involving strain-dependent, non-Fickian hygrothermal effects as well as diffusion induced degradation in the cohesive layer was constructed. The model was implemented in a test-bed finite element code (NOVA-3D). Results from demonstration cases involving synergistic bond degradation were presented.

4.1 Introduction

The influence of moisture diffusion on crack growth along an interface is not yet fully understood. Environmental cracking in a polymer typically occurs in the presence of a penetrant, such as moisture, and stress. It has been postulated that the mechanism involved in environmental crack growth in a polymer involves a small zone of craze formation and/or plasticization at the crack tip. For thermoset resins, such as epoxy, energy absorption at the crack tip is primarily by a shear yielding process and not by crazing. Consequently, for a thermoset epoxy, the zone of plasticization ahead of the crack tip must be determined using a diffusion law for non-porous media, such as Fick's

law. However, quite frequently, polymer composites exhibit deviations from the classical Fickian treatment, termed as anomalous or non-Fickian diffusion, especially at elevated temperatures and stress levels, and at high relative humidity. Some researchers have suggested that the deviation can be explained by a two-stage Fickian process [24, 25]. Others claim that the diffusion process in a polymer is really non-Fickian [26, 27]. Sophisticated hygrothermal models have been developed and verified by Roy [17-20] to account for anomalous diffusion.

The objective of this chapter is to model the synergistic bond degradation mechanisms that might occur at the interface due to interactions between stress, cohesive damage, and penetrant diffusion. For this purpose, a two-dimensional cohesive layer constitutive model with a prescribed traction-separation law is constructed from basic principles of continuum mechanics and thermodynamics, taking into account non-Fickian hygrothermal effects that are likely to occur within the cohesive layer.

4.2 Fickian Diffusion

Diffusion is the process by which matter is transported from one part of a system to another as a result of random molecular motions. In 1855, Fick first put diffusion on a quantitative basis by adopting the mathematical equation of heat conduction. The theory of diffusion in isotropic substance is therefore based on the hypothesis that the rate of transfer of diffusing substance through unit area of a section is proportional to the concentration gradient measured normal to the section, i.e.

$$f = -D\frac{\partial C}{\partial x} \tag{4-1}$$

where C is the concentration of diffusing substance, D is called diffusion coefficient or diffusivity, and is the function of coordinate x, y, and z (location) and concentration C.

Considering the mass balance of diffusing substance, we have

$$\frac{\partial C}{\partial t}+\frac{\partial f_x}{\partial x}+\frac{\partial f_y}{\partial y}+\frac{\partial f_z}{\partial z}=0 \tag{4-2}$$

$$\frac{\partial C}{\partial t}=\frac{\partial}{\partial x}\left(D\frac{\partial C}{\partial x}\right)+\frac{\partial}{\partial y}\left(D\frac{\partial C}{\partial y}\right)+\frac{\partial}{\partial z}\left(D\frac{\partial C}{\partial z}\right) \tag{4-3}$$

The fundamental differential equation of diffusion in an isotropic medium (where D is independent of the concentration C and location) can be expressed as

$$\frac{\partial C}{\partial t}=D\left(\frac{\partial^2 C}{\partial x^2}+\frac{\partial^2 C}{\partial y^2}+\frac{\partial^2 C}{\partial z^2}\right) \tag{4-4}$$

and this is the so-called Fickian diffusion.

4.3 Non-Fickian Diffusion (Strain Assisted Diffusion)

For a two-dimensional cohesive layer of finite thickness h_c, under plane-strain conditions as shown in Fig. 4-1, the Helmholtz free energy per unit volume is given by,

$$\begin{aligned}\rho\psi = {} & C_0(m,T)+C_1(m,T)\varepsilon_{11}+C_2(m,T)\varepsilon_{22}+C_3(m,T)\varepsilon_{12}+C_4(m,T)\varepsilon_{11}^2+C_5(m,T)\varepsilon_{22}^2 \\ & +C_6(m,T)\varepsilon_{12}^2+C_7(m,T)\varepsilon_{11}\varepsilon_{12}+C_8(m,T)\varepsilon_{11}\varepsilon_{22}+C_9(m,T)\varepsilon_{12}\varepsilon_{22}+C_{10}(m,T)\varepsilon_{22}^3 \\ & +C_{11}(m,T)\varepsilon_{22}^2\varepsilon_{12}+C_{12}(m,T)\varepsilon_{22}\varepsilon_{12}^2+C_{13}(m,T)\varepsilon_{12}^3+C_{14}(m,T)\varepsilon_{22}^4+C_{15}(m,T)\varepsilon_{22}^3\varepsilon_{12} \\ & +C_{16}(m,T)\varepsilon_{22}^2\varepsilon_{12}^2+C_{17}(m,T)\varepsilon_{22}\varepsilon_{12}^3+C_{18}(m,T)\varepsilon_{12}^4\end{aligned} \tag{4-5}$$

where the mechanical strain components are defined as,

$$\varepsilon_{11} = E_{11} - \alpha(T - T_{REF}) - \beta(m - m_{REF})$$

$$\varepsilon_{22} = E_{22} - \alpha(T - T_{REF}) - \beta(m - m_{REF})$$

$$\varepsilon_{12} = E_{12}$$

and,

ρ : mass density of material in the cohesive layer

ε_{11} : mechanical strain component in x direction

ε_{22} : mechanical strain component normal to crack face (in y direction)

ε_{12} : shear strain component tangential to crack face

E_{ij} : total (kinematic) strain components

m : moisture concentration in the cohesive layer at time t

m_{REF} : reference moisture concentration

T : temperature in the cohesive layer at time t

T_{REF} : reference temperature

$\alpha(T)$: linear coefficient of thermal expansion

$\beta(T)$: linear coefficient of moisture expansion

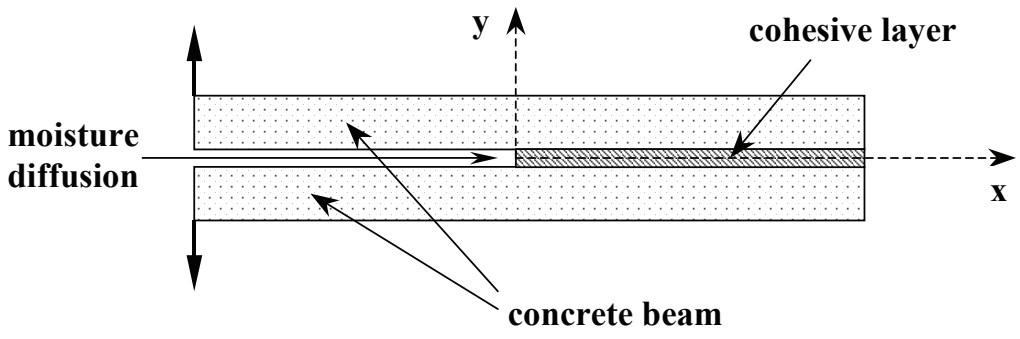

Fig. 4-1. A cohesive layer with moisture diffusion in a DCB beam

From reduced entropy inequality, the cohesive stresses are defined by,

$$\sigma_{11} = \rho \frac{\partial \psi}{\partial E_{11}} = C_1(m,T) + 2C_4(m,T)\varepsilon_{11} + C_7(m,T)\varepsilon_{12} + C_8(m,T)\varepsilon_{22} \tag{4-6}$$

$$\begin{aligned}\sigma_{22} = \rho \frac{\partial \psi}{\partial E_{22}} &= C_2(m,T) + 2C_5\varepsilon_{22} + C_8(m,T)\varepsilon_{11} + C_9(m,T)\varepsilon_{12} + 3C_{10}(m,T)\varepsilon_{22}^2 \\ &+ 2C_{11}(m,T)\varepsilon_{22}\varepsilon_{12} + C_{12}(m,T)\varepsilon_{12}^2 + 4C_{14}(m,T)\varepsilon_{22}^3 \\ &+ 3C_{15}(m,T)\varepsilon_{22}^2\varepsilon_{12} + 2C_{16}(m,T)\varepsilon_{22}\varepsilon_{12}^2 + C_{17}(m,T)\varepsilon_{12}^3\end{aligned} \tag{4-7}$$

Similarly,

$$\begin{aligned}\sigma_{12} &= \rho \frac{\partial \psi}{\partial E_{12}} \\ &= C_3(m,T) + 2C_6(m,T)\varepsilon_{12} + C_7(m,T)\varepsilon_{11} + C_9(m,T)\varepsilon_{22} + C_{11}(m,T)\varepsilon_{22}^2 \\ &+ 2C_{12}(m,T)\varepsilon_{22}\varepsilon_{12} + 3C_{13}(m,T)\varepsilon_{12}^2 + C_{15}(m,T)\varepsilon_{22}^3 + 2C_{16}(m,T)\varepsilon_2^2\varepsilon_{12} \\ &+ 3C_{17}(m,T)\varepsilon_{22}\varepsilon_{12}^2 + 4C_{18}(m,T)\varepsilon_{12}^3\end{aligned} \tag{4-8}$$

Chemical potential of the diffusing vapor is defined by Weistman [28],

$$\mu = \rho \frac{\partial \psi}{\partial \mathrm{m}}$$

or,

$$\begin{aligned}\mu = \frac{\partial C_0}{\partial m} &+ \left[\frac{\partial C_4}{\partial m}\varepsilon_{11}^2 - 2C_4(m,T)\beta(T)\varepsilon_{11}\right] + \left[\frac{\partial C_5}{\partial m}\varepsilon_{22}^2 - 2C_5(m,T)\beta(T)\varepsilon_{22}\right] \\ &+ \left[\frac{\partial C_{10}}{\partial m}\varepsilon_{22}^3 - 3C_{10}(m,T)\beta(T)\varepsilon_{22}^2\right] + \left[\frac{\partial C_{14}}{\partial m}\varepsilon_{22}^4 - 4C_{14}(m,T)\beta(T)\varepsilon_{22}^3\right]\end{aligned} \tag{4-9}$$

From conservation of mass, the governing Equation for two-dimensional moisture diffusion is,

$$\frac{\partial m}{\partial t} = -\left(\frac{\partial f_x}{\partial x} + \frac{\partial f_y}{\partial y}\right) \tag{4-10}$$

where the moisture flux, $\vec{f} = f_x \hat{n}_x + f_y \hat{n}_y$, in the absence of temperature gradients is given by,

$$f_x = -\hat{D}\frac{\partial \mu}{\partial x}$$
$$f_y = -\hat{D}\frac{\partial \mu}{\partial y} \tag{4-11}$$

Assuming isotropic material and using the chain rule,

$$f_x = -\hat{D}\left(\frac{\partial \mu}{\partial m}\right)\frac{\partial m}{\partial x} - \hat{D}\left(\frac{\partial \mu}{\partial T}\right)\frac{\partial T}{\partial x} - \hat{D}\left(\frac{\partial \mu}{\partial \varepsilon_{22}}\right)\frac{\partial \varepsilon_{22}}{\partial x} \tag{4-12}$$

$$f_y = -\hat{D}\left(\frac{\partial \mu}{\partial m}\right)\frac{\partial m}{\partial y} - \hat{D}\left(\frac{\partial \mu}{\partial T}\right)\frac{\partial T}{\partial y} - \hat{D}\left(\frac{\partial \mu}{\partial \varepsilon_{22}}\right)\frac{\partial \varepsilon_{22}}{\partial y} \tag{4-13}$$

Assuming isothermal condition and substituting Eqs. (4-9, 4-12, 4-13) into Eq. (4-10), gives

$$\frac{\partial m}{\partial t} = \frac{\partial}{\partial x}\left(D_m \frac{\partial m}{\partial x} + D_\varepsilon \frac{\partial \varepsilon_{22}}{\partial x}\right) + \frac{\partial}{\partial y}\left(D_m \frac{\partial m}{\partial y} + D_\varepsilon \frac{\partial \varepsilon_{22}}{\partial y}\right)$$

where $D_m = \hat{D}\left(\frac{\partial \mu}{\partial m}\right)$, *and* $D_\varepsilon = \hat{D}\left(\frac{\partial \mu}{\partial \varepsilon_{22}}\right)$

$$\begin{aligned} D_m = \hat{D}\Bigg[& \frac{\partial^2 C_0}{\partial m^2} + \frac{\partial^2 C_4}{\partial m^2}\varepsilon_{11}^2 - 4\frac{\partial C_4}{\partial m}\beta(T)\varepsilon_{11} + 2C_4\beta(T)^2 + \frac{\partial^2 C_5}{\partial m^2}\varepsilon_{22}^2 - 4\frac{\partial C_5}{\partial m}\beta(T)\varepsilon_{22} \\ & + 2C_5\beta(T)^2 + \frac{\partial^2 C_{10}}{\partial m^2}\varepsilon_{22}^3 - 6\frac{\partial C_{10}}{\partial m}\beta(T)\varepsilon_{22}^2 + 6C_{10}(T)\beta(T)^2\varepsilon_{22} + \frac{\partial^2 C_{14}}{\partial m^2}\varepsilon_{22}^4 \\ & - 8\frac{\partial C_{14}}{\partial m}\beta(T)\varepsilon_{22}^3 + 6C_{14}(T)\beta(T)^2\varepsilon_{22}^2 \Bigg] \end{aligned} \tag{4-14a}$$

$$D_{\varepsilon} = \hat{D}\Big[2\frac{\partial C_5}{\partial m}\varepsilon_{22} - 2\beta(T)C_5(T) + 3\frac{\partial C_{10}}{\partial m}\varepsilon_{22}^2 - 6\beta(T)C_{10}(T)\varepsilon_{22} + 4\frac{\partial C_{14}}{\partial m}\varepsilon_{22}^3 - 12\beta(T)C_{14}(T)\varepsilon_{22}^2 \Big] \tag{4-14b}$$

If the unknown material coefficients are expanded in a Taylor Series about a reference moisture concentration value m_{REF}, and retaining terms up to second order in change in moisture concentration,

$$\begin{aligned} C_k(m,T) &= C_k(m_{REF},T) + \left(\frac{\partial C_k}{\partial m}\right)_{m_{REF}}(m - m_{REF}) + \left(\frac{\partial^2 C_k}{\partial m^2}\right)_{m_{REF}}(m - m_{REF})^2 \\ &= \hat{C}_k(m_{REF},T)\left[1 + \overline{C}_k(m_{REF},T)\Delta m + \tilde{C}_k(m_{REF},T)\Delta m^2\right] \qquad (k = 0, 1, ..., 18) \end{aligned} \tag{4-15}$$

In order to benchmark the present model against an established cohesive zone model, some of the unknown material coefficients were determined by assuming a cubic traction-separation law similar to the one proposed by Needleman [7] and modified by El-Sayed and Sridharan [14] for a finite-thickness cohesive layer, giving,

$$\mathrm{C}_0(m,T) = \hat{C}_0(m_{REF},T)\left[1 + \overline{C}_0(m_{REF},T)\Delta m + \tilde{C}_0(m_{REF},T)\Delta m^2\right]$$

$$C_1(m,T) = 0$$

$$C_2(m,T) = 0$$

$$C_3(m,T) = 0$$

$$C_4(m,T) = \frac{\sigma_{MAX}(T)}{\varepsilon_{MAX}}\left[1 + \overline{C}_4(m_{REF},T)\Delta m + \tilde{C}_4(m_{REF},T)\Delta m^2\right]$$

$$C_5(m,T) = \frac{27}{8}\frac{\sigma_{MAX}(T)}{\varepsilon_{MAX}}\left[1 + \overline{C}_5(m_{REF},T)\Delta m + \tilde{C}_5(m_{REF},T)\Delta m^2\right]$$

$$C_6(m,T) = \frac{27}{8}\frac{\tau_{MAX}(T)}{\gamma_{MAX}}\left[1 + \overline{C}_6(m_{REF},T)\Delta m + \widetilde{C}_6(m_{REF},T)\Delta m^2\right]$$

$$\left.\begin{aligned} C_7(m,T) &= 0 \\ C_8(m,T) &= 0 \\ C_9(m,T) &= 0 \end{aligned}\right\} \qquad \text{assume} \quad \nu = 0$$

$$C_{10}(m,T) = -\frac{9}{2}\frac{\sigma_{MAX}(T)}{\varepsilon_{MAX}^2}\left[1 + \overline{C}_{10}(m_{REF},T)\Delta m + \widetilde{C}_{10}(m_{REF},T)\Delta m^2\right]$$

$$C_{11}(m,T) = 0$$

$$C_{12}(m,T) = 0$$

$$C_{13}(m,T) = -\frac{9}{2}\frac{\tau_{MAX}(T)}{\gamma_{MAX}^2}\left[1 + \overline{C}_{13}(m_{REF},T)\Delta m + \widetilde{C}_{13}(m_{REF},T)\Delta m^2\right]$$

$$C_{14}(m,T) = \frac{27}{16}\frac{\sigma_{MAX}(T)}{\varepsilon_{MAX}^3}\left[1 + \overline{C}_{14}(m_{REF},T)\Delta m + \widetilde{C}_{14}(m_{REF},T)\Delta m^2\right]$$

$$C_{15}(m,T) = 0$$

$$C_{16}(m,T) = 0$$

$$C_{17}(m,T) = 0$$

$$C_{18}(m,T) = \frac{27}{16}\frac{\tau_{MAX}(T)}{\gamma_{MAX}^3}\left[1 + \overline{C}_{18}(m_{REF},T)\Delta m + \widetilde{C}_{18}(m_{REF},T)\Delta m^2\right]$$

Substituting these definitions in expressions for c_{11}, c_{22}, c_{12}, (Eqs. 4-6, 4-7, and 4-8) results in,

$$2\hat{C}_4(T) = \overline{E}(T) = \frac{\sigma_{MAX}(T)}{\varepsilon_{MAX}}$$

gives

$$\sigma_{11} = \sigma_{MAX}(T)\left[1 + \overline{C}_4(m_{REF},T)\Delta m + \widetilde{C}_4(m_{REF},T)\Delta m^2\right]\overline{\varepsilon}_{11} \qquad (4\text{-}16)$$

Similarly,

$$\begin{aligned}\sigma_{22} &= 2\hat{C}_5(T)\left[1+\overline{C}_5(m_{REF},T)\Delta m+\widetilde{C}_5(m_{REF},T)\Delta m^2\right]\varepsilon_{22}\\ &+3\hat{C}_{10}(T)\left[1+\overline{C}_{10}(m_{REF},T)\Delta m+\widetilde{C}_{10}(m_{REF},T)\Delta m^2\right]\varepsilon_{22}^2\\ &+4\hat{C}_{14}(T)\left[1+\overline{C}_{14}(m_{REF},T)\Delta m+\widetilde{C}_{14}(m_{REF},T)\Delta m^2\right]\varepsilon_{22}^3\end{aligned}$$

or

$$\begin{aligned}\sigma_{22} = \frac{27}{4}\sigma_{MAX}(T)\Big\{&\left[1+\overline{C}_5(m_{REF},T)\Delta m+\widetilde{C}_5(m_{REF},T)\Delta m^2\right]\bar{\varepsilon}_{22}\\ &-2\left[1+\overline{C}_{10}(m_{REF},T)\Delta m+\widetilde{C}_{10}(m_{REF},T)\Delta m^2\right]\bar{\varepsilon}_{22}^2\\ &+\left[1+\overline{C}_{14}(m_{REF},T)\Delta m+\widetilde{C}_{14}(m_{REF},T)\Delta m^2\right]\bar{\varepsilon}_{22}^3\Big\}\end{aligned} \tag{4-17}$$

where the maximum tensile stress in the cohesive layer is c_{MAX} and characteristic interface length δ is related to the layer thickness h_c by, $h_c = \dfrac{\delta}{\varepsilon_{MAX}}$.

And finally the shear stress can be expressed as,

$$\begin{aligned}\sigma_{12} = \frac{27}{4}\tau_{MAX}(T)\Big\{&\left[1+\overline{C}_6(m_{REF},T)\Delta m+\widetilde{C}_6(m_{REF},T)\Delta m^2\right]\bar{\varepsilon}_{12}\\ &-2\left[1+\overline{C}_{13}(m_{REF},T)\Delta m+\widetilde{C}_{13}(m_{REF},T)\Delta m^2\right]\bar{\varepsilon}_{12}^2\\ &+\left[1+\overline{C}_{18}(m_{REF},T)\Delta m+\widetilde{C}_{18}(m_{REF},T)\Delta m^2\right]\bar{\varepsilon}_{12}^3\Big\}\end{aligned} \tag{4-18}$$

where $\bar{\varepsilon}_{11} = \dfrac{\varepsilon_{11}}{\varepsilon_{MAX}}$, $\bar{\varepsilon}_{22} = \dfrac{\varepsilon_{22}}{\varepsilon_{MAX}}$, $\bar{\varepsilon}_{12} = \dfrac{\varepsilon_{12}}{\gamma_{MAX}}$, the maximum shear stress in the cohesive layer is τ_{MAX}.

The consistent diffusivities D_m and D_ε for the cohesive layer are obtained by substituting the definitions of the material coefficients into Eqs. (4-14a, 4-14b),

$$
\begin{aligned}
D_m = \hat{D}\Big\{ & 2\hat{C}_0(T)\widetilde{C}_0(T) \\
& + \frac{\sigma_{MAX}(T)}{\varepsilon_{MAX}}\left[2\widetilde{C}_4\varepsilon_{11}^2 - 4\beta(\overline{C}_4 + 2\widetilde{C}_4\Delta m)\varepsilon_{11} + 2\beta^2(1+\overline{C}_4\Delta m + \widetilde{C}_4\Delta m^2)\right] \\
& + \frac{27}{8}\frac{\sigma_{MAX}(T)}{\varepsilon_{MAX}}\left[2\widetilde{C}_5\varepsilon_{22}^2 - 4\beta(\overline{C}_5 + 2\widetilde{C}_5\Delta m)\varepsilon_{22} + 2\beta^2(1+\overline{C}_5\Delta m + \widetilde{C}_5\Delta m^2)\right] \\
& - \frac{9}{2}\frac{\sigma_{MAX}(T)}{\varepsilon_{MAX}^2}\left[2\widetilde{C}_{10}\varepsilon_{22}^3 - 4\beta(\overline{C}_{10} + 2\widetilde{C}_{10}\Delta m)\varepsilon_{22}^2 + 2\beta^2(1+\overline{C}_{10}\Delta m + \widetilde{C}_{10}\Delta m^2)\varepsilon_{22}\right] \\
& + \frac{27}{16}\frac{\sigma_{MAX}(T)}{\varepsilon_{MAX}^3}\left[2\widetilde{C}_{14}\varepsilon_{22}^4 - 4\beta(\overline{C}_{14} + 2\widetilde{C}_{14}\Delta m)\varepsilon_{22}^3 + 2\beta^2(1+\overline{C}_{14}\Delta m + \widetilde{C}_{14}\Delta m^2)\varepsilon_{22}^2\right]\Big\}
\end{aligned}
\tag{4-19}
$$

$$
\begin{aligned}
D_\varepsilon = \hat{D}\Big\{ & \frac{27}{4}\frac{\sigma_{MAX}(T)}{\varepsilon_{MAX}}\left[(\overline{C}_5 + 2\widetilde{C}_5\Delta m)\varepsilon_{22} - \beta(1+\overline{C}_5\Delta m + \widetilde{C}_5\Delta m^2)\right] \\
& - \frac{27}{2}\frac{\sigma_{MAX}(T)}{\varepsilon_{MAX}^2}\left[(\overline{C}_{10} + 2\widetilde{C}_{10}\Delta m)\varepsilon_{22}^2 - 2\beta(1+\overline{C}_{10}\Delta m + \widetilde{C}_{10}\Delta m^2)\varepsilon_{22}\right] \\
& + \frac{27}{4}\frac{\sigma_{MAX}(T)}{\varepsilon_{MAX}^3}\left[(\overline{C}_{14} + 2\widetilde{C}_{14}\Delta m)\varepsilon_{22}^3 - 3\beta(1+\overline{C}_{14}\Delta m + \widetilde{C}_{14}\Delta m^2)\varepsilon_{22}^2\right]\Big\}
\end{aligned}
\tag{4-20}
$$

4.4 Cohesive Layer Diffusion Boundary Conditions

Assuming that the chemical potential of the ambient vapor on the exposed boundary of the cohesive zone remains constant with respect to time [28], the resulting concentration at the boundary of the cohesive zone (crack tip) can be derived as,

$$
\mu(T, m, \varepsilon_{ij})\big|_{BOUNDARY} = \mu_b \tag{4-21}
$$

$$\mu_b = \Big\{ \hat{C}_0(\overline{C}_0 + 2\widetilde{C}_0\Delta m) + \frac{27}{8}\frac{\sigma_{MAX}(T)}{\varepsilon_{MAX}}\Big[(\overline{C}_5 + 2\widetilde{C}_5\Delta m)\varepsilon_{22}^2 - 2\beta(1+\overline{C}_5\Delta m + \widetilde{C}_5\Delta m^2)\varepsilon_{22}\Big] - \frac{9}{2}\frac{\sigma_{MAX}(T)}{\varepsilon_{MAX}^2}\Big[(\overline{C}_{10} + 2\widetilde{C}_{10}\Delta m)\varepsilon_{22}^3 - 3\beta(1+\overline{C}_{10}\Delta m + \widetilde{C}_{10}\Delta m^2)\varepsilon_{22}^2\Big] + \frac{27}{16}\frac{\sigma_{MAX}(T)}{\varepsilon_{MAX}^3}\Big[(\overline{C}_{14} + 2\widetilde{C}_{14}\Delta m)\varepsilon_{22}^4 - 4\beta(1+\overline{C}_{14}\Delta m + \widetilde{C}_{14}\Delta m^2)\varepsilon_{22}^3\Big]\Big\}_{BOUNDARY}$$

An equation about the unknown moisture concentration Δm at the boundary can be derived in the form of $a\Delta m^2 + b\Delta m + c = 0$.

Therefore the boundary concentration can be solved

$$m_b = m_{REF} + \frac{-b \pm \sqrt{b^2 - 4ac}}{2a} \tag{4-22}$$

4.5 Cohesive Layer Work-of-Separation

For pure Mode I or Mode II fracture, the work-of-separation at the cohesive interface (of finite thickness h_c) per unit volume in the presence of moisture concentration (Δm) is given by

$$\begin{aligned}\phi_{sep}^I &= \int_V \left[\int_0^{\varepsilon_{\max}} \sigma_{22} d\varepsilon_{22}\right] dV = h_c \int_0^1 \sigma_{22}\varepsilon_{MAX} d\bar{\varepsilon}_{22} \\ &= h_c \int_0^1 \Big\{ \frac{27}{4}\sigma_{MAX}(T)\varepsilon_{MAX}\Big\{\Big[1+\overline{C}_5\Delta m + \widetilde{C}_5\Delta m^2\Big]\bar{\varepsilon}_{22} \\ &\quad - 2\Big[1+\overline{C}_{10}\Delta m + \widetilde{C}_{10}\Delta m\Big]\bar{\varepsilon}_{22}^2 + \Big[1+\overline{C}_{14}\Delta m + \widetilde{C}_{14}\Delta m^2\Big]\bar{\varepsilon}_{22}^3\Big\}\Big\} d\bar{\varepsilon}_{22} \\ &= \frac{27}{4}\sigma_{MAX}(T)\varepsilon_{MAX}h_c\Big\{\frac{1}{2}\Big[1+\overline{C}_5\Delta m + \widetilde{C}_5\Delta m^2\Big] \\ &\quad - \frac{2}{3}\Big[1+\overline{C}_{10}\Delta m + \widetilde{C}_{10}\Delta m\Big] + \frac{1}{4}\Big[1+\overline{C}_{14}\Delta m + \widetilde{C}_{14}\Delta m^2\Big]\Big\}\end{aligned} \tag{4-23}$$

$$\phi_{sep}^{II} = \int_V \left[\int_0^{\gamma_{\max}} \sigma_{12} d\varepsilon_{12}) \right] dV = h_c \int_0^1 \sigma_{12} \gamma_{MAX} d\bar{\varepsilon}_{12}$$

$$= h_c \int_0^1 \left\{ \frac{27}{4} \tau_{MAX}(T) \gamma_{MAX} \left\{ \left[1 + \bar{C}_6 \Delta m + \tilde{C}_6 \Delta m^2 \right] \bar{\varepsilon}_{12} \right.\right.$$

$$\left.\left. - 2\left[1 + \bar{C}_{13} \Delta m + \tilde{C}_{13} \Delta m^2 \right] \bar{\varepsilon}_{12}^2 + \left[1 + \bar{C}_{18} \Delta m + \tilde{C}_{18} \Delta m^2 \right] \bar{\varepsilon}_{12}^3 \right\} \right\} d\bar{\varepsilon}_{12} \quad (4\text{-}24)$$

$$= \frac{27}{4} \tau_{MAX}(T) \gamma_{MAX} h_c \left\{ \frac{1}{2} \left[1 + \bar{C}_6 \Delta m + \tilde{C}_6 \Delta m^2 \right] \right.$$

$$\left. - \frac{2}{3} \left[1 + \bar{C}_{13} \Delta m + \tilde{C}_{13} \Delta m \right] + \frac{1}{4} \left[1 + \bar{C}_{18} \Delta m + \tilde{C}_{18} \Delta m^2 \right] \right\}$$

or write in the short form

$$\phi_{sep}^{I} = \frac{9}{16} \sigma_{MAX}(T) \varepsilon_{MAX} h_c \left[1 + A_1(T) \Delta m + A_2(T) \Delta m^2 \right] \quad (4\text{-}25)$$

$$\phi_{sep}^{II} = \frac{9}{16} \tau_{MAX}(T) \gamma_{MAX} h_c \left[1 + A_3(T) \Delta m + A_4(T) \Delta m^2 \right] \quad (4\text{-}26)$$

The thickness of the cohesive layer, h_c, is a measure of the fracture localization zone and it is directly related to the characteristic length scale of the fracture process zone controlled by specific fracture mechanism [29]. The area under the normalized stress-strain curve ($0 \le \frac{\varepsilon}{\varepsilon_{\max}} \le 1$) shown in Fig. 4-2 represents the work-of-separation of the cohesive layer. From Eqs. (4-25, 4-26) and experimental results, it can be observed that the work-of-separation decreases at elevated temperature and higher moisture concentration due to the physical or chemical degradation at the interface through a decrease in the maximum peel stress and a corresponding reduction in the area under the curve. When considering the time-dependent behavior of the polymeric adhesive, work-of-separation is also a function of time. Lower work-of-separation would imply lower critical strain energy release rate, and therefore, lower resistance to crack growth.

4.6 Cohesive Layer Degradation and FEA Simulation

The proposed cohesive layer model was implemented in an in-house finite element code, NOVA-3D. In the previous section, the parameters $\overline{C}_i$ and $\widetilde{C}_i$ are material constants to be determined experimentally. Moisture diffusion tests and fracture experiments are necessary to characterize these coefficients.

4.6.1 Cohesive Layer Degradation due to Moisture Concentration

When moisture diffuses into the cohesive layer, two effects occur concurrently. First, the cohesive layer begins to swell thereby causing the local stress state to change due to the constraining effect of the surrounding adherends. Secondly, it is likely that moisture will penetrate the bulk cohesive layer to reach the cohesive interface (or interphase), and then rapidly diffuse along the interface. At the interface, water molecules typically react with the chemical bonds across the interface especially in the presence of tensile stress, because stress provides additional driving force for the bond rupturing process. Such chemical reactions transform strong covalent bonds to weak Van der Waals bonds, thereby significantly weakening the interface strength and fracture toughness. The bond-strength degradation could be important even when the change in moisture concentration is relatively small (~10%) [16].

Due to a lack of available bond degradation data from ongoing experiments to allow characterization of material coefficients in Eq. (4-15) at present time, a simple

bond strength degradation scheme (as illustrated in Fig. 4-2) was employed for the present analysis while preserving the basic framework presented in Eq. (4-15).

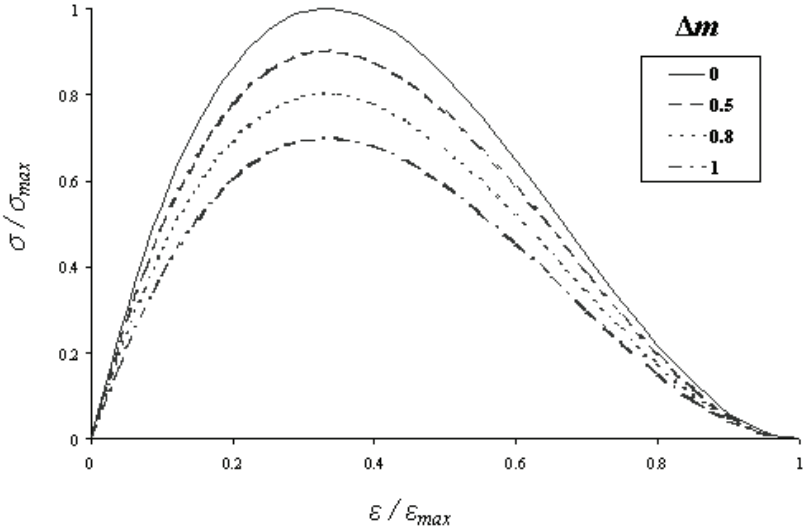

Fig. 4-2. Depiction of the influence of moisture in cohesive layer on work-of-separation

4.6.2 FEA Simulation Results

Fully coupled stress and diffusion analyses were invoked in this investigation, analogous to simulating a wedge-test under wet conditions. For the DCB specimen, moisture diffusion analysis is activated only in the cohesive layer, with moisture boundary conditions applied at the exposed surface at $x = 0$ as depicted in Fig. 4-1. A cohesive layer thickness $h_c = 0.02\ \ mm$ and beam height $h_b = 1\ \ mm$ were used, Material properties used in this analysis are listed in Tables 3-1, and the diffusivity of the cohesive layer is $5.22 \times 10^{-8} mm^2 / s$.

With time, moisture gradually diffuses from the exposed debond tip ($x = 0$) into the originally dry elements in the cohesive layer. Due to the lack of the material

coefficients defining non-Fickian diffusivities given by Eq. (4-15), linear Fickian diffusion with constant boundary concentration ($m_b = 1\times10^{-8}\, g/mm^3$) was modeled in the cohesive layer for this demonstration case. Fig. 4-3 depicts the moisture concentration profiles plotted along the bond length with the origin at the original location of the debond tip at four different time steps. The corresponding analytical solutions for one-dimensional Fick's law are also plotted in Fig. 4-3 for diffusion model verification. It is evident that the concentration profiles predicted by the finite element diffusion analysis are in excellent agreement with the analytical solution for the linear case. Incidentally, the horizontal dashed line in Fig. 4-3 corresponds to 10% of saturation concentration and its purpose will be discussed in the following paragraphs.

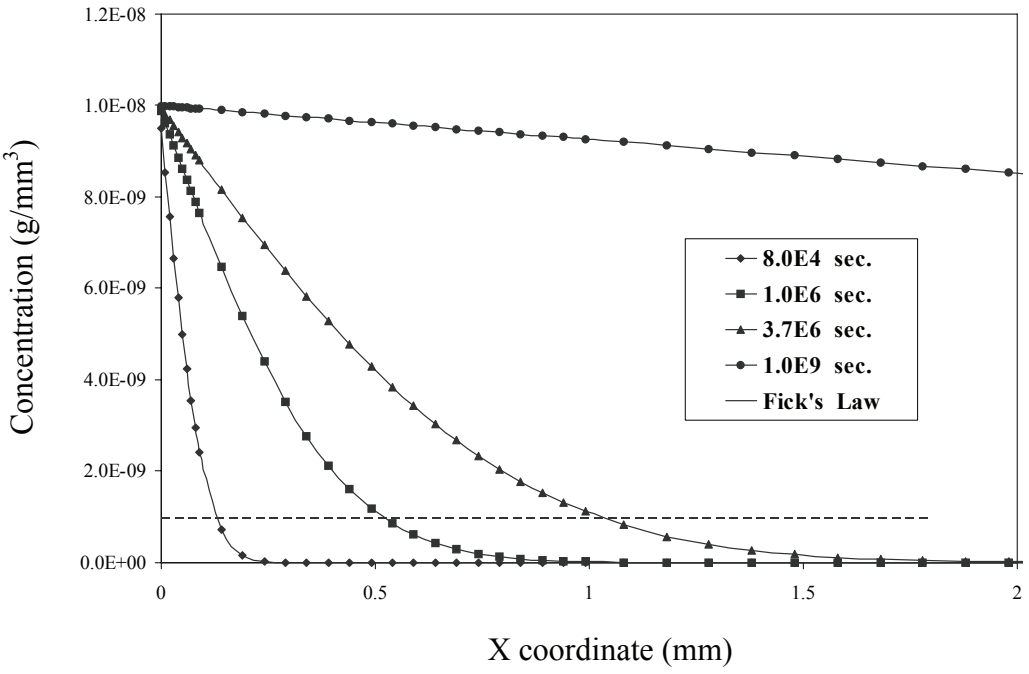

Fig. 4-3 Comparison of predicted moisture concentration profiles

A phenomenological step-function degradation law is assumed in the analysis such that when the local moisture concentration is greater than or equal to 10% of the

saturation concentration corresponding to the dashed horizontal line in Fig. 4-3, the corresponding maximum stress ($c_{\max}$) in the cohesive traction-separation law is reduced by 10% . For numerical stability, a linear degradation is assumed when the concentration is between 0 and 10% . The length of the moisture-induced cohesive strength degradation zone at various time steps is indicated by the intersection of the concentration profile and the horizontal dashed line in Fig. 4-3.

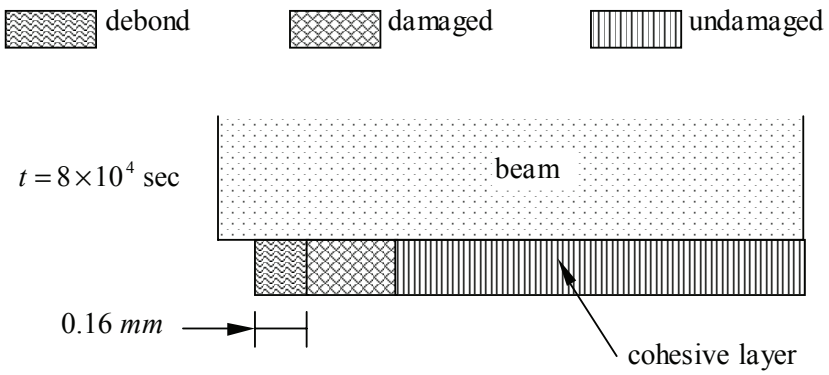

(a) Under dry condition

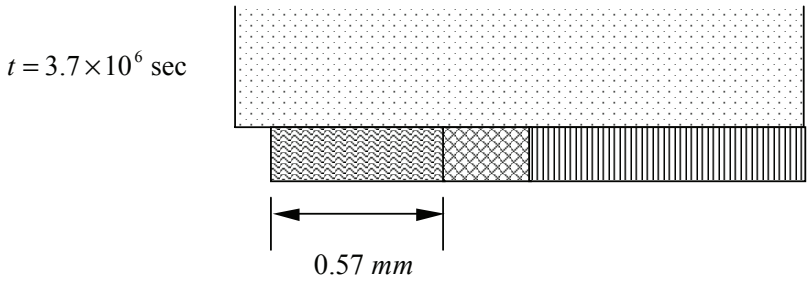

(b) Degradation due to moisture concentration

Fig. 4-4 Debond growth in a cohesive layer due to moisture degradation

In this demonstration case, a constant beam tip displacement is applied at all times for the DCB, simulating a wedge test. The debond growth predicted at the crack tip by

the finite element analysis is 0.16 *mm* at initial time ($t = 0$) under dry conditions as shown in Fig. 4-4(a). Over time, as moisture diffusion and subsequent bond degradation takes place, debond propagation occurs and the failure length increases to 0.57 *mm* over a period of 3.7×10^{6} seconds, as depicted in Fig. 4-4(b). Failure (or debond) length is determined by observing if the transverse mechanical strain, ε_{22}, has exceeded the prescribed maximum transverse strain, $\varepsilon_{\max}$, along the bond length. Fig. 4-5 shows that the transverse mechanical strain monotonically increases with time due to the formation of cohesive damage, material failure, and resultant debond propagation. The location of the crack tip of the failure zone at various time steps is indicated by the intersection of the mechanical strain and the horizontal dashed line in Fig. 4-5 indicating failure strain, $\varepsilon_{\max}$ (debond length increases from 0.16 *mm* to 0.57 *mm* due to strength degradation caused by moisture diffusion).

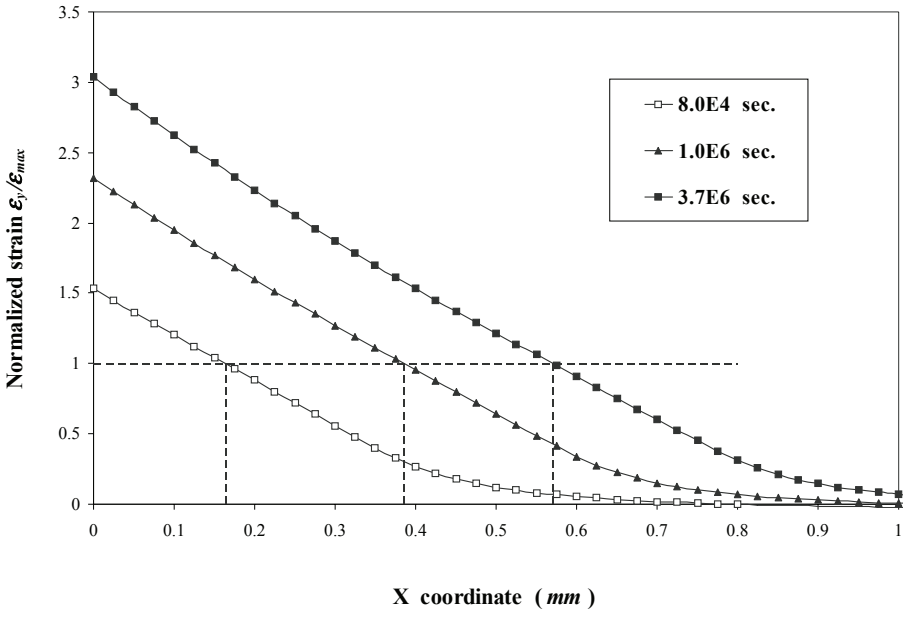

Fig. 4-5 Transverse mechanical strains and corresponding failure zones at different moments

The reduction in corresponding transverse stress distribution at different time steps is plotted along bond length in Fig. 4-6. The progressive reduction in the peak stress magnitude is due to degradation of bond strength caused by moisture ingress. Evolution of debond length with time is plotted in Fig. 4-7, and the decrease in reaction force due to the degradation of cohesive layer stiffness with time is shown in Fig.4-8. It is evident that for the present case, debond growth is driven by a synergistic interaction of moisture diffusion and transverse stress near the debond tip as discussed in the following paragraph.

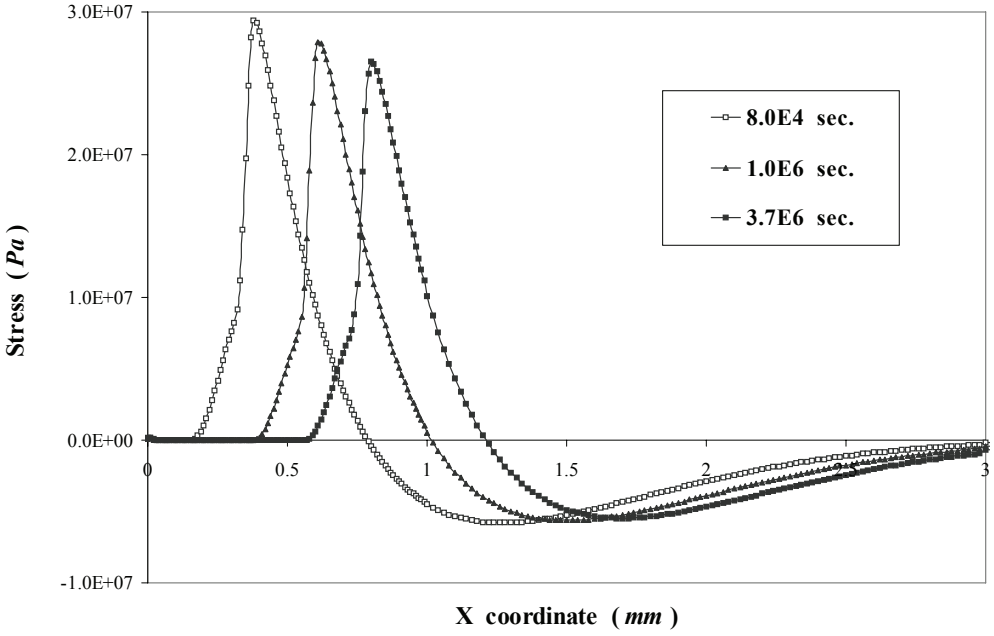

Fig. 4-6. Transverse stresses along bond length at different moments

There are two important milestones during the diffusion-assisted debond growth process, $t_1 = 8\times10^4$ second and $t_2 = 3.7\times10^6$ second (see Fig. 4-7). For $0 \le t < t_1$, the moisture concentration ahead of the crack tip is not high enough to result in significant

degradation to the cohesive layer. Therefore, no debond growth occurs during this period. At roughly $t = t_1$, the 10% concentration front impinges on the debond tip and triggers debond growth as shown in Fig. 4-6. For $t_1 \leq t \leq t_2$, the moisture concentration ahead of the debond tip becomes high enough (>10%) such that the onset of bond degradation occurs, resulting in steady debond growth as shown in Fig. 4-7. In this regime, the debond growth is driven by the rate of propagation of the 10% concentration front, and therefore can be said to be diffusion-controlled. Finally, for $t > t_2$, the debond driving force (shown in Fig. 4-8) falls below a threshold value such that no further synergistic debond growth is possible. In this case, the peak transverse stress in the cohesive layer has decreased to $0.9\sigma_{max}$ as shown in Fig. 4-6 due to the assumed moisture degradation characteristics. At the same time the transverse deformation (Fig. 4-4) and debond length (Fig. 4-7) have reached steady state values, respectively.

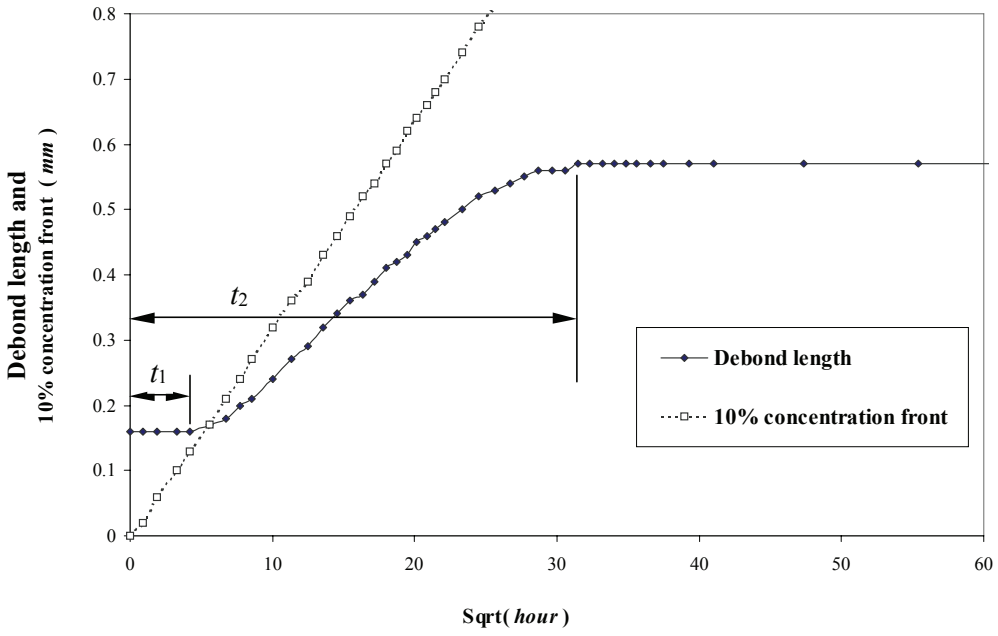

Fig. 4-7 Predicted evolution of debond length with time

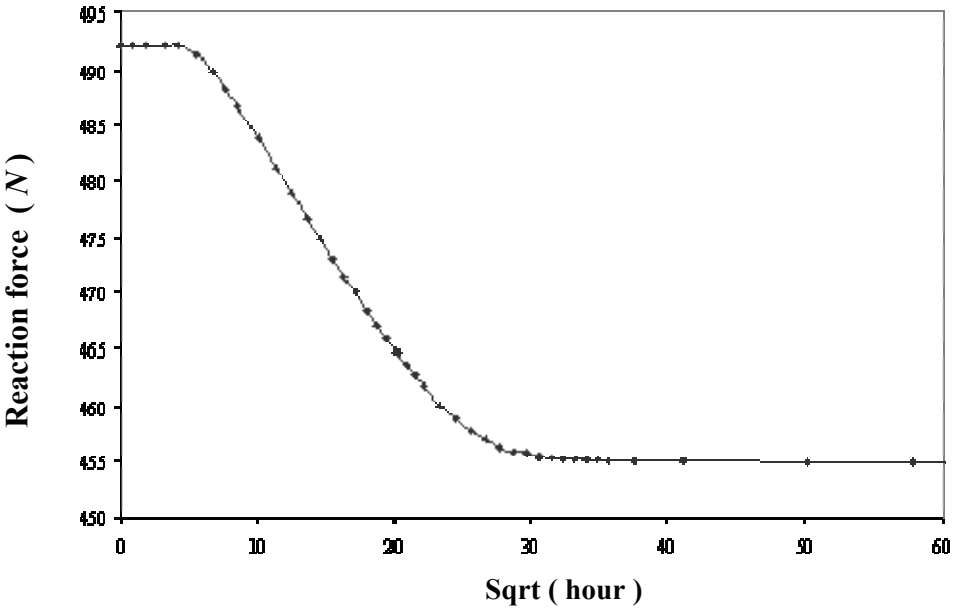

Fig. 4-8 Reaction force decreases with time

4.7 Conclusions

A two-dimensional cohesive layer constitutive model with a prescribed traction-separation law was constructed from basic principles of continuum mechanics and thermodynamics, taking into account concentration-dependent and strain-dependent non-Fickian hygrothermal effects that are likely to occur within a cohesive layer. Implementation of the model in a test-bed finite element code was carried out and code verification was performed. Numerical simulation of a wedge-test involving debond growth caused by synergistic interactions between local stress and diffusing moisture was also presented to demonstrate the ability of the cohesive layer model to simulate environmental cracking.

CHAPTER V

NUMERICAL SIMUILATION OF PENINSULA BLISTER TEST

The objective of this paper is to examine three-dimensional and viscoelastic effects in the peninsula blister test for thin film adhesion, which is considered an effective way to measure the interfacial fracture toughness of bonded thin film structures. As will be demonstrated in this Chapter, analytical solutions are sometimes inadequate for accurately simulating peninsula blister experiments because linear elastic behavior is assumed in the thin film as well as in the debonding process zone at the interface. For this purpose, a three-dimensional cohesive layer model and corresponding liquid loading simulation algorithm were developed and implemented into an in-house test-bed finite element analysis (FEA) code (NOVA-3D). Features such as three-dimensional mixed-mode debonding, large displacements and rotations, residual stresses in the thin film, and time-dependent (viscoelastic) effects in the thin film were considered. Numerical convergence and a stable debond growth were obtained over a fairly large debond length when suitably refined FEA mesh and liquid volume increment were employed. Detailed benchmark comparisons of the finite element predictions with analytical solutions and experimental results were performed, and good agreement was obtained.

5.1 Introduction

Laminated thin film structures appear in a wide variety of applications such as multilayer structures, microelectronic devices, and packages. The increasing application of thin films in industry has made it necessary to better understand the nature and the reliability of the bonding between layers or bi-material interface. Since poor bonding results in a crack or delamination, fracture mechanics is a natural approach for characterizing the resistance to failure and making durability or reliability prediction. For this purpose, several experimental methods, including peel tests, blister tests, indentation tests, scratch tests etc., have been used to determine the interfacial bond strength or toughness.

The peel test is a simple and perhaps the most commonly used method for examining the strength of adhesively bonded layers. In a peel test, a thin flexible strip that is bonded to a substrate is pulled off at a certain angle to the underlying substrate. In the absence of any plastic deformation and residual stresses, adhesive fracture energy Γ can be derived directly [30] from the peel force through

$$\Gamma = (1 - \cos\varphi)P \tag{5-1}$$

where P is the peel force per unit width of the film and φ is the peel angle.

In reality, plastic deformation in the peeling arm and crack tip singularity are present in all the peel test specimens, and were investigated by Kim et al. [31], Kinloch et al. [32], and Wei and Hutchinson [33]. It implies that a significant portion of the mechanical energy applied in peeling is dissipated and, if not properly accounted for, will lead to significant overestimates of the adhesive fracture energy. This is particularly true

when the yield strength of the peeling film is relatively low and the degree of adhesion is high.

The pressurized circular blister test was developed by Williams [34] as an alternative approach to minimize dissipation effects and overcome some of the other drawbacks of the peel test. In many blister tests, a pressurized fluid (usually water is used and considered as incompressible) is injected between the faces of the crack between the film and substrate via a hole through the substrate. A uniform fluid pressure is applied to the thin film and hence the problems associated with mechanical contact and gripping are avoided. Furthermore, the axisymmetry of the circular blister configuration greatly minimize edge effects and effects due to specimen nonuniformity.

The standard blister configuration (circular blister) was first introduced by Dannenberg [35] in 1961 to measure the adhesion of thick organic coating to metal. As tougher interface were examined, problems were encountered with tensile failure in blister film prior to debond at the interface. Another disadvantage of circular blister is that the strain energy release rate increases as the fourth power of the debond radius, thus making accurate evaluation of the debond radius essential, and resulting in a very unstable fracture specimen. Several alternative configurations with higher strain energy release rates were developed. These configurations include island blister proposed by Allen and Senturia [36], constrained blister proposed by Napolitano et al. [37] and Chang et al. [38], and peninsula blister proposed by Dillard and Bao [39].

In a constrained blister specimen, even though the strain energy release rate is independent of debond radius, the effect of friction between the delaminating film and the constraint could be significant, raising concern about the difficulty of analyzing contact

problems with large deformation. In the island blister specimen, debond growth occurs radially inwards on the island. A moderate increase in compliance is produced by a relative small increase in debond area, thereby giving rise to high strain energy release rates. As the island radius decreases with debonding, the calculated strain energy release rates increase in an unbounded manner.

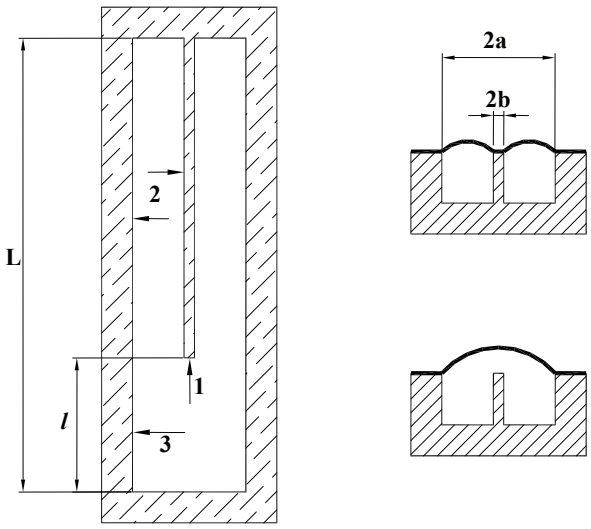

Fig. 5-1 Peninsula blister specimen and possible debond sites

The peninsula blister is an extension of the island blister concept. Its name is derived from the fact that debonding will occur along a narrow "peninsula" which extends into the blister region, as shown in Fig. 5-1. The peninsula blister configuration not only maintains the high energy release rate of the island blister but also provides a constant energy release rate as the adhesive debond progresses. Added features include the larger debond area and additional data points that can be obtained from a single specimen. A consistent set of analyses by Liechti and Shirani [40] showed that the only configuration among circular, island, and peninsula blister specimen with a homogeneous

delaminating layer that did not suffer any yielding was a relatively thick peninsula blister configuration. A subsequent cohesive zone fracture analysis by Shirani and Liechti [41] found that only 6% of the work input was dissipated as global plastic dissipation in a polyimide thin film on aluminum, a relatively tough interface. Disadvantages of the peninsula blister test include the lack of symmetry and difficulties in the fabrication of the specimen for certain material systems.

Despite its promising advantages, the peninsula blister configuration has not gained wide acceptance in the adhesion testing community. One problem is the relatively complex nature of the specimen fabrication although this can be alleviated by suitable masks. Another is the relatively complex nature of the analysis particularly when large deformations and rotations and residual stresses are encountered. Both issues have recently been addressed [42]. One issue that is yet to be resolved on the analytical front is an accounting of the viscoelastic nature of many adhesives, particularly under long term loadings [43]. On the other hand, problems were also encountered in numerical simulation of peninsula blister test, such as the loss of axisymmetric geometry, mixed mode I and mode II nonlinear fracture (and even mode III), large deflections and rotations in the film and adhesive layer, and large debond length. Another problem is the special loading methodology of the blister test. It employs a liquid-volume-control loading approach which is obviously different from any general applied force or displacement loading methods.

The purpose of the work presented here was to consider optimum geometries for peninsula blister specimens while accounting for geometric nonlinearities, viscoelastic effects and mixed-mode debonding. A three-dimensional cohesive layer model and

corresponding liquid loading simulation algorithm were developed and implemented into an in-house test-bed FEA code (NOVA-3D). Numerical convergence was achieved with suitable increment of liquid volume and with reasonable FEA mesh refinement. Steady-state debond growth was obtained over a fairly large portion of the specimen. The finite element results were benchmarked against analytical solutions and experimental data.

5.2 Constitutive Law and Failure Criterion of Cohesive Layer

Peninsula blister specimen is a full three-dimensional configuration. Three-dimensional stress-strain traction-separation law is adopted to simulate the cohesive layer as shown in Eqs. (2-3, 2-4).

In peninsula blister specimen, shear force perpendicular to the peninsula direction (corresponding to mode III fracture) was observed in peninsula blister test and simulation. A more complex failure criterion that contains the contribution of mode III debond was used in this case.

$$\frac{G_I}{G_{Ic}} + \frac{G_{II}}{G_{IIc}} + \frac{G_{III}}{G_{IIIc}} = 1 \tag{5-2}$$

Detailed description of the 3-D cohesive layer model and its failure criterion is given in Chapter II.

5.3 Specimen Geometry and Energy Release Rates

Proper choices of the geometry and, in particular, the aspect ratios of the peninsula blister specimen and regions within it are essential in order to ensure that

debond initiation and propagation occurs in the 1-direction along the narrow peninsula area as shown in Fig. 5-1. Debonding at sites 2 and 3 is also possible but is undesirable. From the standpoint of linear elastic fracture mechanics, the energy release rate can be used to predict crack initiation and propagation; it can be viewed as the driving force for crack propagation or debond growth. When the deflection of the film is on the order of the film thickness, the theory of linear elastic thin plates can be applied in this case. Dillard and Bao [39] determined the analytical solution of the strain energy release rates for debonding at the three sites under a given liquid pressure p

$$G_1 = \frac{p^2}{1440Db}\left[16a^5 - (a-b)^5\right] \tag{5-3}$$

$$G_2 = \frac{p^2(a-b)^4}{288D} \tag{5-4}$$

$$G_3 = \frac{p^2 a^4}{288D} \tag{5-5}$$

where D is the bending stiffness of the film given by

$$D = \frac{Eh^3}{12(1-\upsilon^2)} \tag{5-6}$$

E , υ , and h are its Young's modulus, Poisson's ratio, and thickness, respectively.

Numerical results from FEA analysis (NOVA-3D) are in very good agreement with Dillard's analytical solutions as shown in Fig. 5-2 and 5-3. It can be seen from Fig. 5-3 that higher energy release rate G can be achieved at site 1 for a small peninsula width. Therefore, when the peninsula width is relatively small (e.g. $\frac{b}{a} < 0.2$), debond will

occur preferentially at site 1 rather than site 3 (because $G_1 > G_3$). It should also be noted that G_1 is greater than G_2 for all $\frac{b}{a}$ ratios, implying debond of the peninsula would always propagate along the peninsula length rather than across the width. As evident from Fig 5-2, in order to obtain large energy release rates with the peninsula specimen, the most effective way is to select small values of $\frac{b}{a}$. It is suggested that $\frac{b}{a} = 0.1$ is likely to be the most practical choice, as overly small $\frac{b}{a}$ will increase difficulties in fabricating specimen.

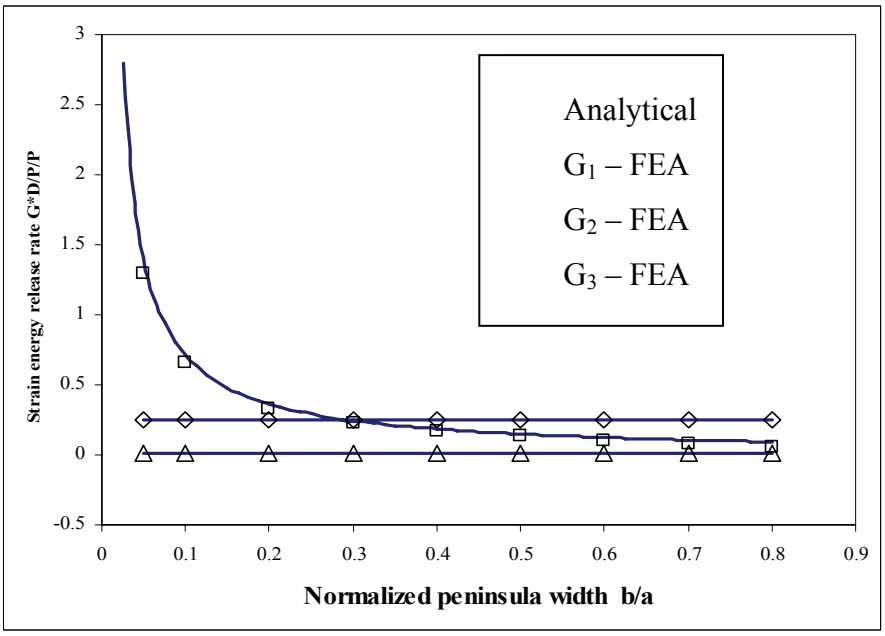

Fig. 5-2 Effect of relative peninsula width on the energy release rate

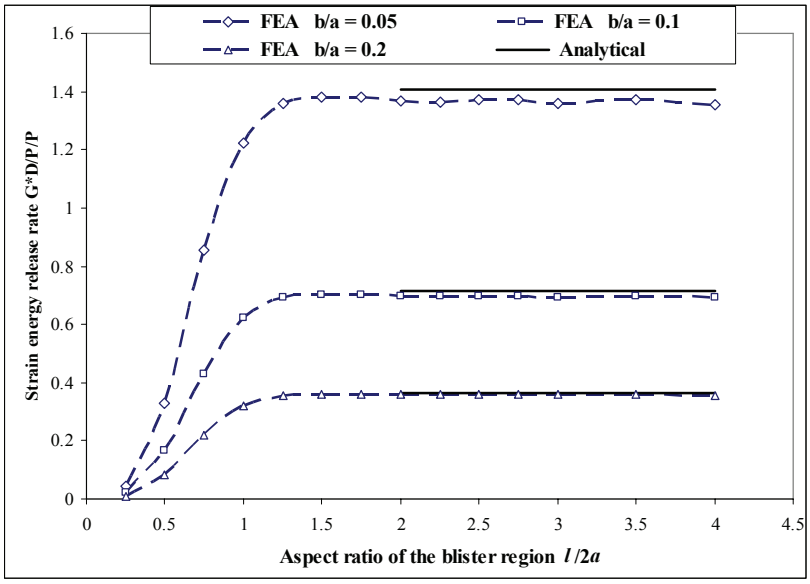

Fig. 5-3 Effect of blister region aspect ratio on the energy release rate (Analytical solution is derived from $l/2a > 2$)

Aspect ratio of the blister region ($\frac{l}{2a}$) also deserves examination. The derivation of strain energy release rates discussed earlier (Eqs. 5-3 ~ 5-5) was based on a plate with infinite length and clamped along the two remaining boundaries. According to Timoshenko and Woinowsky-Krieger [44], for an aspect ratio of 2, the deviation in the mid-plane deflection of a fully clamped plate (all four sides clamped) from the infinite plate solution is only 2%. It can be concluded that when the aspect ratio $\frac{l}{2a} > 2$ in the wider inflated region, and $\frac{L-l}{a-b} > 2$ at the end of the peninsula (i.e. the narrow inflated regions at the two sides of the peninsula), errors in the above derivation from infinite plate solution are negligible. Furthermore, a constant energy release rate G_1 is obtained when debond occurs within the limits of $4a < l < L - 2(a-b)$. FEA simulations point to

similar conclusion as shown in Fig. 5-3. When aspect ratio $\frac{l}{2a} < 1.5$, value of energy release rate G_1 increases as the debond grows. For larger blister lengths, energy release rate remains constant and converges to the solution of the infinitely long plate.

Additional verifications using numerical techniques will be presented in section 5.

5.4 Time-Dependent Behavior of Polymeric Thin Film

Polymeric thin films typically display some time-dependent behavior, such as, creep and/or relaxation due to molecular motion. A linear viscoelastic model was employed in the current study to simulate the time-dependent behavior of the polymeric film.

The three-dimensional constitutive equations of linear viscoelastic material are,

$$\sigma_{kk}(t) = \int_0^t 3K(t-\tau)\frac{\partial \theta}{\partial \tau} d\tau \tag{5-7}$$

$$S_{ij}(t) = \int_0^t 2\mu(t-\tau)\frac{\partial e_{ij}}{\partial \tau} d\tau \tag{5-8}$$

where s_{ij} and e_{ij} are the stress and mechanical strain deviators, respectively, $\theta = \varepsilon_{kk}$ is the volumetric strain. The bulk relaxation modulus $K(t)$ and shear relaxation modulus $\mu(t)$ can be expressed using Prony Series as,

$$K(t) = K_\infty + \sum_{i=1}^{n} K_i e^{-t/\tau_i} \tag{5-9}$$

$$\mu(t) = \mu_\infty + \sum_{i=1}^{n} \mu_i e^{-t/\tau_i} \tag{5-10}$$

The linear viscoelastic model for the thin film was implemented into the FEA simulation code NOVA-3D. FEA simulations of debond in a peninsular blister specimen using elastic and viscoelastic thin film were conducted and compared with test data.

5.5 Simulations of Debonding in the Peninsula Blister Experiment

5.5.1 Simulation under Small Deformation

A three-dimensional cohesive layer model with 20-node quadratic brick element was implemented into a test-bed FEA code NOVA-3D. Convergence studies showed that stable debonding was obtained within a fairly large debond region if the aspect ratio of the element in the debond tip area and the increment of liquid volume (loading increment) are sufficiently small. As the liquid is injected into the blister at a constant rate, the pressure also increases linearly with time (or liquid volume) before debond occurs. When the failure criterion given by Eq. (5-2) is satisfied, the cohesive layer elements at the debond tip fail and debonding initiates. Instead of the node release and element deletion schemes used in most finite element codes, a failed element remains active in the subsequent analysis while the stiffness of the element is reduced to approximately zero. As the cohesive layer elements fail, new surfaces are generated and the pressurized liquid occupies the newly debonded volume.

In the present work, the original aspect ratio at the beginning of simulation is set as $\frac{l}{2a} = 0.75$. During the simulation, as the debond initiates and propagates, the film deflection and aspect ratio increase while liquid pressure decreases, as shown in Fig. 5-4.

When the aspect ratio is greater than 1.5, liquid pressure stabilizes and remains constant, and a constant strain energy release rate is obtained. However, the maximum deflection in the thin film increases continuously until the aspect ratio is greater than 2. As alluded to earlier, this result agrees with Timoshenko's solution for infinite plate [44]. Debond process near the end of the peninsula was also studied in this paper. When the aspect ratio in the inflated region $\frac{L-l}{a-b}<1.5$, pressure will start to increase due to the boundary effects (These simulation results will be discussed in Section 6.3). From both analytical and FEA simulations, it can be concluded that the effective test domain for peninsula blister test is: $\frac{l}{2a}>1.5$ and $\frac{L-l}{a-b}>1.5$. When debond occurs within this domain, constant strain energy release rates will be obtained.

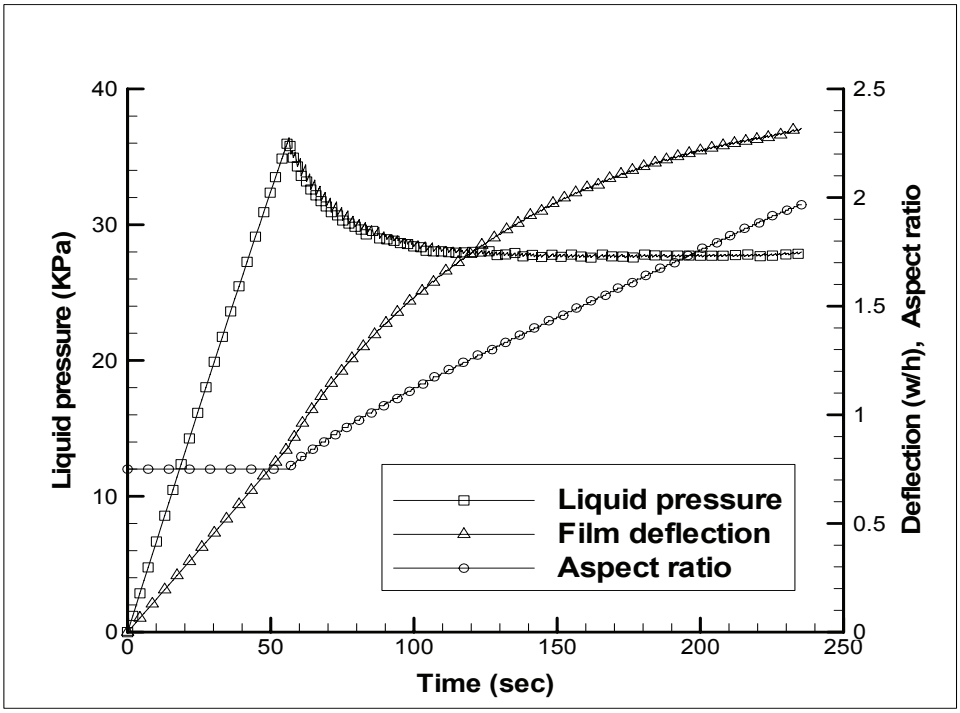

Fig. 5-4 Peninsula blister responses over large debond lengths

5.5.2 Peninsula Blister Specimen and Test Results

The data used here was obtained from a peninsula blister specimen with dimensions $L = 35.56mm$, $l = 15.24mm$, $2a = 10.16mm$, $2b = 1.27mm$ ($\frac{2b}{2a} = 0.125$) with an initial aspect ratio $\frac{l}{2a} = 1.5$ (as illustrated in Fig. 5-1). The epoxy thin film in the current simulation was assumed as linear elastic and its Young's modulus was $E = 1.78GPa$, Poisson's ratio was $\upsilon = 0.3$, and film thickness was $h_f = 0.127mm$. Residual stresses $\sigma_x^R = \sigma_y^R = 5.7MPa$ were obtained from bulge tests and, for analysis, were applied to the thin film before loading. The aluminum substrate was considered to be rigid both. The critical energy release rates (or fracture energy) extracted from the blister test was $G_c = 100 \sim 110 J/m^2$ (including residual stresses) and $G_c = 130 \sim 140 J/m^2$ (without residual stress). In addition, a critical pressure of 80.9kPa was observed at debond initiation, along with a constant pressure of 86.5kPa during stable debonding.

The adhesive material which was used to bond the epoxy thin film to the substrate is Hysol EA9696, with an adhesive strength of $\sigma_{\max} = 42.7MPa$. The maximum strain in the adhesive layer is assumed to be $\varepsilon_{\max} = 0.1$. When applying cohesive layer model to this specimen, a cohesive layer thickness $h_c = 0.0416mm$ was determined from Eq. (2-16) (including residual stresses in the thin film and a fracture energy $G_c = 100 J/m^2$).

It should be clarified here that in the present case, the thickness of adhesive layer is different from the cohesive layer thickness. The latter is determined by adhesive

material properties and corresponding fracture energy or debond energy as presented in Eq. (2-16). Consequently, only a portion of the adhesive layer is modeled by the special three-dimensional cohesive layer elements and the remainder of the adhesive layer was modeled by regular elements. Exact measurements of the adhesive layer thickness in peninsula blister specimen are difficult and the debond process is not sensitive to the adhesive layer thickness. Therefore we can reasonably assume that the adhesive layer thickness is equal to the cohesive layer thickness. In other words, only one layer of cohesive layer elements was employed to represent the entire adhesive layer.

5.5.3 Simulation with Large Deformation and Residual Stresses

For peninsula blister specimen, both the thin film and adhesive layer experience large deflections and rotations near the debond tip during debond growth. An updated Lagrangian (UL) formulation [45] was employed to cope with the geometrical nonlinear characteristics in the thin film (nonlinear strain-displacement relations, while the stress-strain relation in the thin film is still linear). The UL formulation was combined with Cauchy stress and Almansi strain tensor as energy conjugates.

A typical finite element mesh for the three-dimensional peninsula specimen is shown in Fig. 5-5. Only one layer of three-dimensional 20-node brick element was used to model both the thin film and a portion of the adhesive layer. In the plane of the film, element dimension along the debond (peninsula) direction is greatly dependent on the film thickness as smaller film thickness will experience larger bending deformation near the debond tip; a fine mesh was used to account for the sharp stress gradients and large curvature near the debond tip. Convergence studies showed that the critical pressure is

rather sensitive to the element dimension in the peninsula direction (Table 5-1). However, when the ratio of element size in the x-direction to film thickness was $\Delta x/h_f = 0.4$, convergence was achieved.

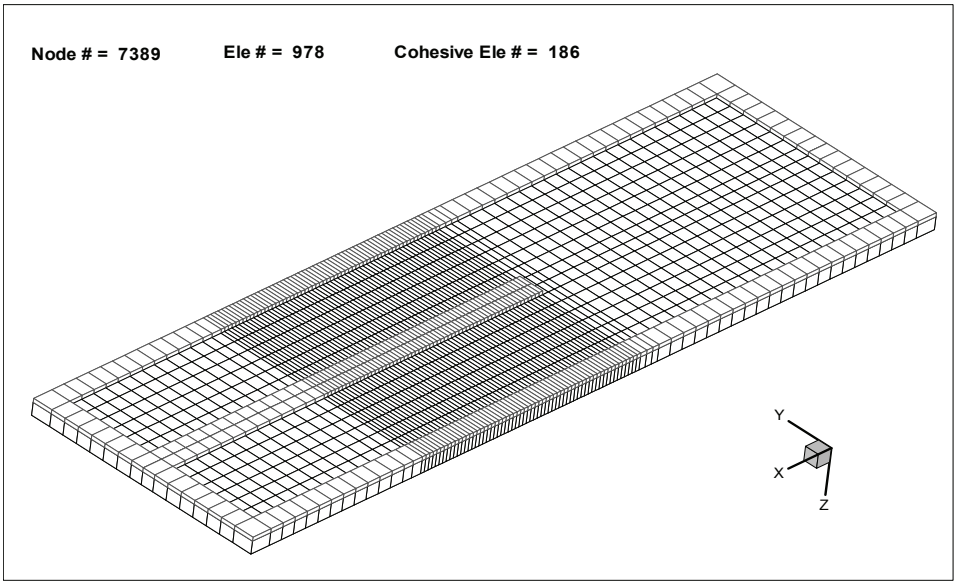

Fig. 5-5 3-D FEA mesh with 20-node brick element

(Viewed from the bottom, elements on the top are the cohesive layer element)

Table 5-1 Different element size in peninsula direction

Element size ($\Delta x/h_f$ *)	1.6	0.8	0.4	0.2
Critical pressure (kPa)	110.5	100.0	95.5	94.0
Deflection (w/h_f)	3.87	3.70	3.62	3.59
Liquid volume (mm^3)	46.6	44.2	43.0	42.6

*: Δx is the element dimension in peninsula direction, h_f is the film thickness, w is the maximum deflection in the thin film

Residual stresses, due to mismatch of thermal coefficients of expansion are usually present in the thin film following cure. Assuming a thermal expansion coefficient $\alpha = 0.0001/^{o}C$ and a temperature change $\Delta T = -23^{o}C$, resulted in uniform residual stresses $\sigma_x^R = \sigma_y^R = 5.7MPa$ throughout the thin film.

The effect of residual stresses on critical pressure and maximum deflection were considered (Table 5-2) for equibiaxial residual stresses ranging from 0 to 15 *MPa*. The impact on critical pressure and maximum deflection were noticeable. The mode I/II phase angle ϕ ranged from $38^{\circ} \sim 53^{\circ}$ while the mode I/III phase angle φ varied from $9^{\circ} \sim 13^{\circ}$ over the residual stress levels that were considered. They remained nearly constant during debond growth. This indicates that mixed-mode I/II debond failure is dominant and the mode III contribution is relatively small, and may be neglected in peninsula blister specimen.

Table 5-2 Effect of residual stresses on debond process as predicted by FEA simulations

Residual stress $\sigma_x^R = \sigma_y^R$ (*MPa*)	0	3.0	5.7	10.0	15.0
Critical pressure (*KPa*)	79.7	88.6	95.5	106.0	116.6
Maximum deflection (w/h_f)	4.01	3.81	3.62	3.35	3.08
Liquid volume (mm^3)	48.0	45.2	43.0	40.2	36.8
Phase angle (I and II) (^{o})	53.5	49.5	46.1	41.8	37.8
Phase angle (I and III) (^{o})	12.6	11.9	11.3	10.4	9.7

Note: Phase angle is the average value for the elements along the perpendicular direction of the peninsula.

Measured and predicted pressure and maximum deflection history are given in Fig. 5-6. Stable debond pressure predicted by the elastic FEA simulation is $P = 96.0KPa$, which is approximately 11% higher than the test value of $P = 86.5KPa$. The error is probably due to the fact that the viscoelastic effects in the thin film were ignored. Another possible source of error is that the simple failure criterion given by Eq. (5-2) may not exactly reflect the real debond conditions. The initial aspect ratio ($\frac{l}{2a}$) of current peninsula blister specimen is 1.5, and therefore the pressure would remain constant during debond growth process while maximum deflection increases continuously as the debond propagates until the aspect ratio reaches 2.5. This is in agreement with that derived from the theory of thin plates. Three-dimensional film displacement profiles from FEA simulations at different stages of debonding are shown in Fig. 5-7.

The debonding process near the end of the peninsula region was also studied. According to the analytical solution derived from the theory of elastic plates, pressure will start to increase when the aspect ratio in the narrow region $\frac{L-l}{a-b} < 1.5$. FEA simulation results showed (Fig. 5-8) that when the debond tip approached the end of the peninsula (an aspect ratio $\frac{L-l}{a-b} < 1.0$), the pressure and film deflection started to increase with debond growth.

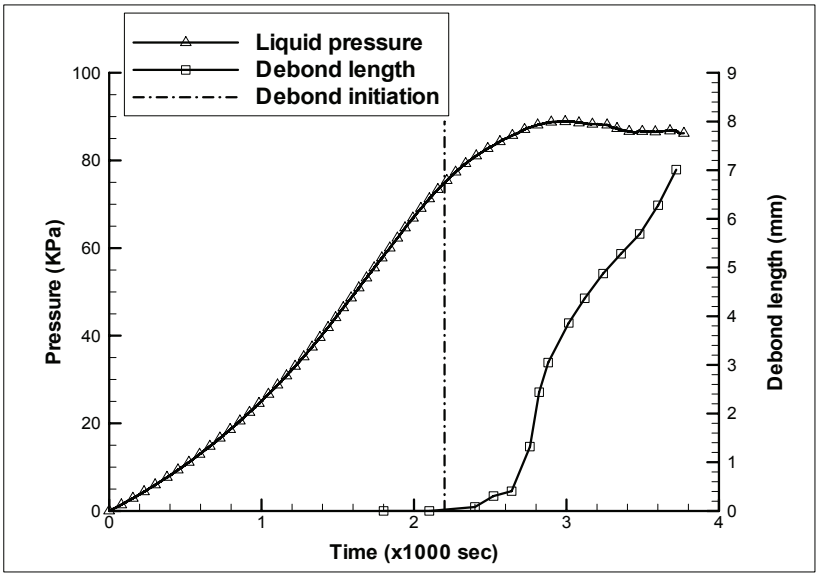

(a) Test data

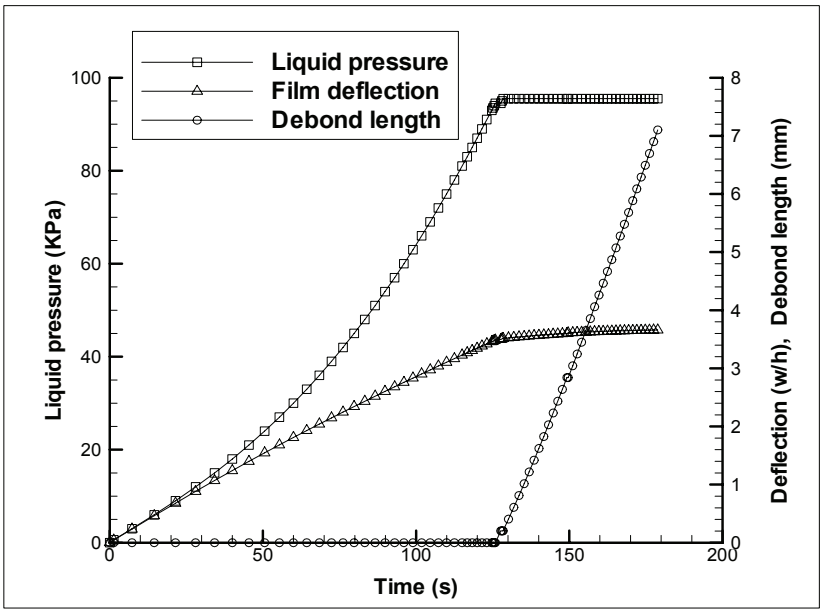

(b) Simulation results

Fig. 5-6 FEA simulation of peninsula blister responses
(with large deformation and residual stresses)

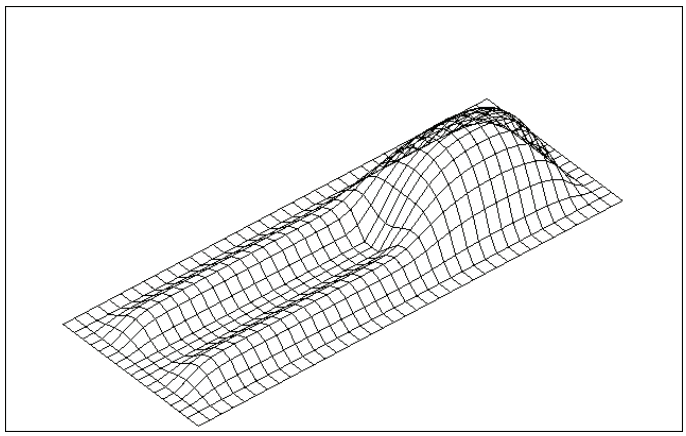

(a) Aspect ratio = 1

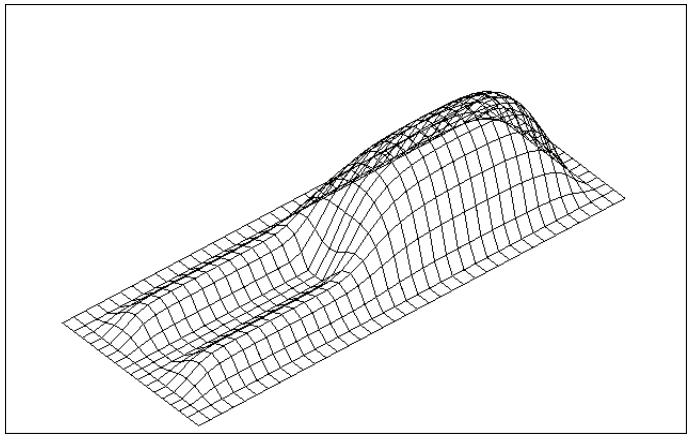

(b) Aspect ratio = 2

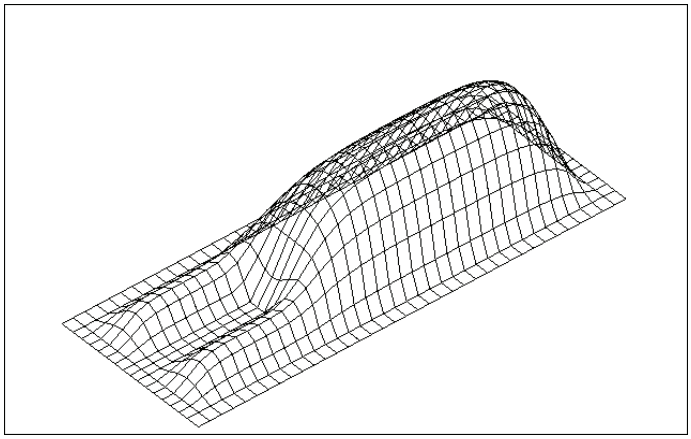

(c) Aspect ratio = 2.5

Fig.5-7 Simulated 3-D film displacement profiles at different stages of debonding

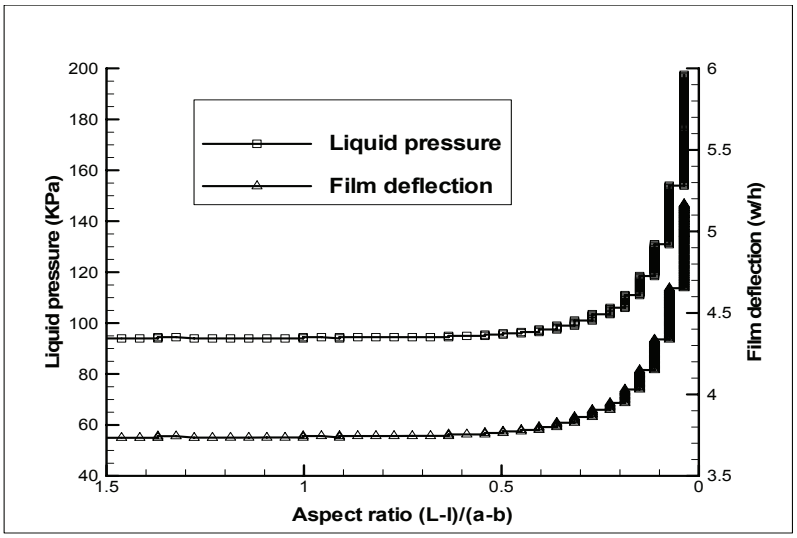

Fig. 5-8 Predicted liquid pressure and film deflection increase when debond approaches the end of the peninsula

5.5.4 Simulation Including Time-Dependent Effect

In the simulation of geometrically nonlinear, elastic debonding in thin film peninsula blister specimens with an initial aspect ratio of 1.5, critical pressure remains constant once the debond has initiated. However, in the actual peninsula blister test, a moderate increase in pressure was observed in the early stages of debond growth (Fig. 5-6). This suggested that there might be some time-dependent effects in the epoxy thin film. Due to unavailability of the time-dependent material properties of the epoxy thin film in the current blister test, a demonstration simulation considering linear viscoelastic effects in the thin film was performed to examine the influence of time-dependent material properties on the critical pressure and the debond process.

For the purpose of highlighting the effect of linear viscoelasticity of the thin film, the material properties for a linear viscoelastic epoxy thin film corresponding to the elastic film were defined and scaled from the tested values as follows: the tensile modulus $E_0 = 1.78GPa$ and Poisson's ratio $\upsilon_0 = 0.3$ of the elastic thin film correspond to the values of the viscoelastic tensile relaxation modulus, $E(t)$, and Poisson's ratio, $\upsilon(t)$, at the time $t = 0$, i.e.,

$$E_0 = E(t)\big|_{t=0} = 1.78GPa$$

$$\upsilon_0 = \upsilon(t)\big|_{t=0} = 0.3$$

For a typical linear viscoelastic epoxy thin film, material properties such as bulk relaxation modulus $K(t)$, shear relaxation modulus $\mu(t)$, tensile modulus $E(t)$, and Poisson's ratio $\upsilon(t)$ at room temperature can be expressed in the form of a Prony Series. The Prony Series coefficients for the epoxy thin film are listed in Table 5-3 using data obtained for an epoxy [46].

For a liquid injection rate $R = 80mm^3 / hour$, the simulation accounting for large deformations and residual stresses showed that the liquid pressure remained constant after debond initiation for a linearly elastic thin film. However, for a viscoelastic thin film (Fig. 5-9a), the liquid pressure did increase at the early stages of debond growth before reaching a steady state value. Stable debond processes with constant liquid pressures were obtained in both cases with constant but slightly different energy release rates.

Table 5-3 Material properties of a viscoelastic epoxy

	$Log(\tau_i)$	K_i (MPa)	$\mu_i(MPa)$	$E_i(MPa)$	υ_i
1	-4.3	24.64	0.22	0.21	-3.11 x 10-4
2	-3.3	25.54	0.45	0.11	-4.95 x 10-4
3	-2.3	104.24	20.88	68.48	-8.31 x 10-4
4	-1.3	29.14	20.32	29.72	-1.13 x 10-3
5	-0.3	150.32	22.11	93.33	-3.19 x 10-3
6	0.7	155.61	160.32	387.51	-2.40 x 10-3
7	1.7	440.03	161.77	491.45	-5.44 x 10-3
8	2.7	330.48	310.46	758.45	-6.53 x 10-3
9	3.7	438.32	159.01	552.47	-1.19 x 10-2
10	4.7	226.82	187.85	377.34	-1.66 x 10-2
11	5.7	206.62	71.09	256.68	-1.74 x 10-2
12	6.7	245.83	63.80	137.01	-2.59 x 10-2
13	7.7	49.88	21.35	95.43	-6.03 x 10-2
14	8.7	169.51	20.31	47.03	-1.18 x 10-2
15	9.7	34.86	11.30	53.36	3.00 x 10-3
16	10.7	82.59	6.45	15.69	-3.04 x 10-3
17	11.7	11.97	3.08	17.01	2.20 x 10-3
18	12.7	40.06	0.25	4.14	-9.92 x 10-4
19	13.7	8.54	1.29	7.19	1.57 x 10-4
	∞	2337.41	12.34	36.91	0.4974

*: At room temperature 23.5°C and relative humidity 35%

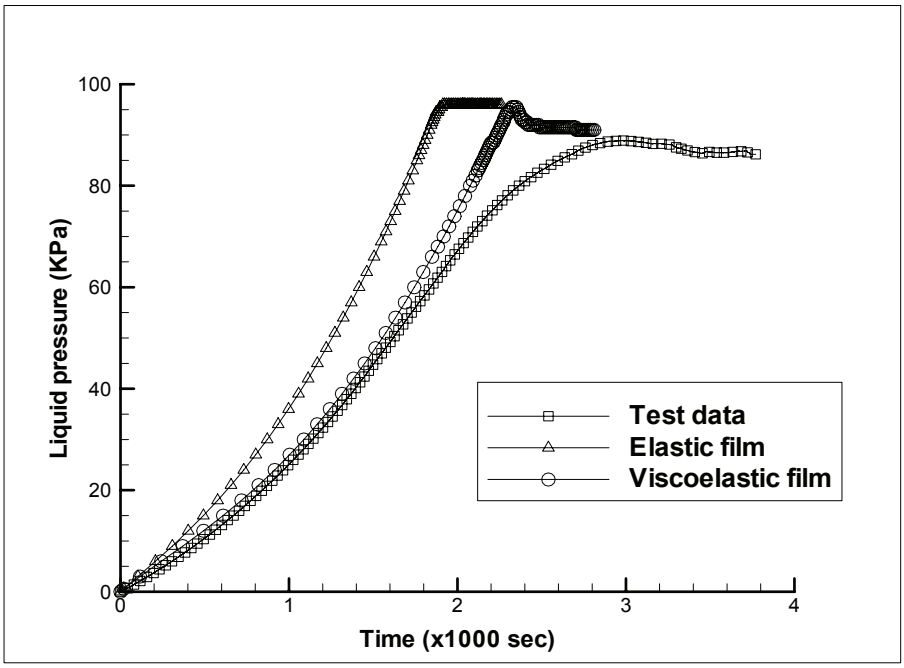

(a) Liquid pressure history

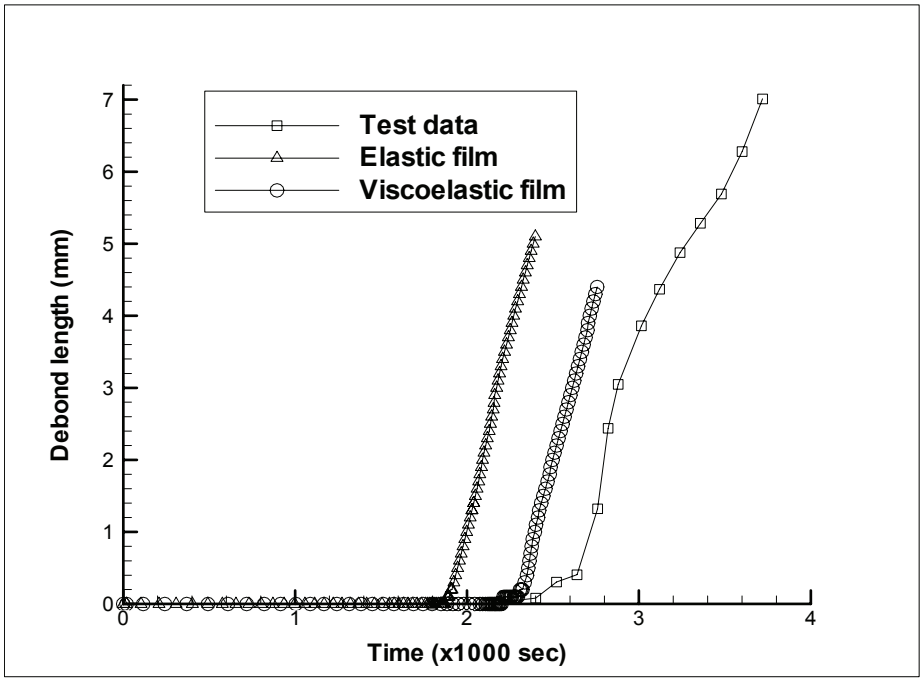

(b) Debond length history

Fig. 5-9 Peninsula blister test data and FEA simulation results (with large deformation and residual stresses)

Measurements and simulation results for both elastic and viscoelastic thin films are shown in Fig. 5-9 and tabulated in Table 5-4 for comparison. Fig. 5-9(a) compares the pressure history as a function of time, while Fig. 5-9(b) depicts comparison of the debond growth history. From Fig. 5-9 and Table 5-4 it is evident that including viscoelastic time-dependence in the thin film response results in a significant reduction in the error between simulations and test data. It should be noted that the slight discrepancy in the time scales of the simulation and test data is due to some leakage of liquid that was observed during the peninsula blister test especially at elevated pressure levels.

When a lower liquid injection rate $R = 10mm^3/hour$ was employed for the viscoelastic thin film simulation, the debond initiation pressure decreased from $88.5KPa$ (corresponding to $R = 80mm^3/hour$) to $84.0KPa$ while the peak pressure and stable debond pressure remained unchanged. Thus it is likely that the debond initiation pressure will be closer to the test value of $80.9kPa$ as the injection rate is decreased.

Table 5-4 Peninsula blister test data and FEA predictions with elastic and viscoelastic thin film

Event	Test data		Linear elastic thin film			Viscoelastic thin film		
	Time	Pressure	Time	Pressure	Error	Time	Pressure	Error
Debond initiation	2250	80.9	1880	94.5	***16.8***	2210	88.5	***9.39***
Peak pressure	2980	88.9	1910	96.0	***7.99***	2340	95.5	***7.42***
Stable debond	3400	86.5	1910	96.0	***11.0***	2490	91.5	***5.78***

Unit: Time -- second, Pressure -- kPa, Error -- % (predicted pressure compared with test data)

5.6 Conclusions

Peninsula blister specimen is an effective way to measure the interfacial fracture toughness of a variety of adhesive bond systems as it offers very high energy release rate values and maintains constant energy release rates over a large range of debond lengths. A three-dimensional cohesive layer model and a corresponding three-dimensional mixed-mode failure (debond) criterion were developed based on the principles of continuum mechanics and fracture mechanics. It was implemented in a finite element code to simulate quasi static debonding in the peninsula blister test. Numerical convergence and stable debond growth were obtained over a fairly large range of debond lengths. The results from FEA simulations were in reasonable agreement with both an analytical solution and test data. Suitable geometries for the peninsula blister specimen were studied by both analytical and FEA approaches and guidelines were reiterated for the design of peninsula blister specimen. FEA simulation results also showed that large deflections, time-dependent material behavior, and residual stresses in the thin film are important factors that should be considered in simulations of the peninsula blister test in order to extract the interfacial fracture toughness of a given adhesive system.

CHAPTER VI

SIMULATION OF TIME-DEPENDENT DEBOND GROWTH

The objective of this chapter is to model the synergistic bond degradation mechanisms that may occur at the interface between a fiber reinforced polymer (FRP) and a substrate. FEA Simulation of a wedge test was conducted, and the time-dependent effect in the adhesive layer was involved in the simulation model. The results predicted by the computational model were benchmarked through comparison with analytical solutions and mixed mode fracture tests. Steady debond growth was obtained after the wedge front entered the originally bonded area, which is consistent with the observations from wedge tests.

6.1 Introduction

Polymeric thin films usually display some time-dependent behaviors due to molecular motion. This effect was also observed in blister test and creep test on a fully clamped polymeric plate. A linear viscoelastic model was introduced to simulate the time-dependent behavior of the polymeric film by peninsula blister test (Chapter V).

Non-Fickian hygrothermal effects on cohesive layer are derived in Chapter IV. It should be noted that in the present approach, expansion of Helmholtz free energy in terms of convolution integrals was not carried out to directly include viscoelasticity in the

cohesive stress-strain law. This is because the use of convolution integrals in addition to temperature and moisture dependence would render the cohesive stress-strain law intractable as far as characterization of the convolution coefficients is concerned. Therefore, in the interest of tractability, a simplified approach is employed where the rate-dependent behavior in the cohesive layer is implemented through the characterization of rate-dependence of the maximum stresses and maximum strains in the cohesive layer as presented in Table 6-1.

The remainder of the polymeric adhesive outside the cohesive layer is modeled as a nonlinear viscoelastic continuum with time-dependent constitutive behavior. The influence of temperature and moisture concentration on the work-of-separation and on crack growth is derived from first-principles. The model is implemented in a test-bed finite element code NOVA-3D. Results predicted by the cohesive layer model are benchmarked through comparison with experimental data from mixed-mode fracture experiments performed using a moving wedge test. Rate-dependent debond process was also investigated with this model under different debond speeds.

6.2 Failure Criterion Based on Work-of-Separation

Several mixed mode failure criteria of the cohesive layer are described in Chapter II. A new failure criterion based on fracture energy was introduced to predict the debond process of a wedge test. Fracture energy 2Γ of the adhesive was extracted from the wedge test. Let the fracture energy 2Γ equal to the work-of-separation of cohesive layer with mixed mode I and mode II fracture, gives

$$2\Gamma = \eta\phi_{sep} = \eta(\alpha\phi_{sep}^{I} + \beta\phi_{sep}^{II}) \tag{6-1}$$

Where ϕ_{sep}^{I} and ϕ_{sep}^{II} are the work-of-separation of pure mode I and mode II debond, respectively (Chapter II and Chapter IV)

For pure mode I fracture under dry conditions ($\Delta m = 0$): $\phi_{sep}^{I} = \frac{9}{16}\sigma_{\max}\varepsilon_{\max}h_c$

For pure mode II fracture under dry conditions ($\Delta m = 0$): $\phi_{sep}^{II} = \frac{9}{16}\tau_{\max}\gamma_{\max}h_c$

ϕ_{sep} is the total work-of-separation of the mixed mode debond. It is easy to derive the relation $\phi_{sep} = \alpha\phi_{sep}^{I} + \beta\phi_{sep}^{II}$, where α and β are constants determined by the failure type (i.e. mode mix) of the cohesive layer. Comparing the idealized cohesive stress-strain curve in Fig. 2-3 with the uniaxial tension test data of the adhesive material in Fig. 6-1, it was found that the actual work-of-separation from the test data is less than the theoretic one predicted by traction-separation law due to the premature failure of epoxy primer. Thus a correction factor $\eta = 0.75$ was introduced to reflect the difference.

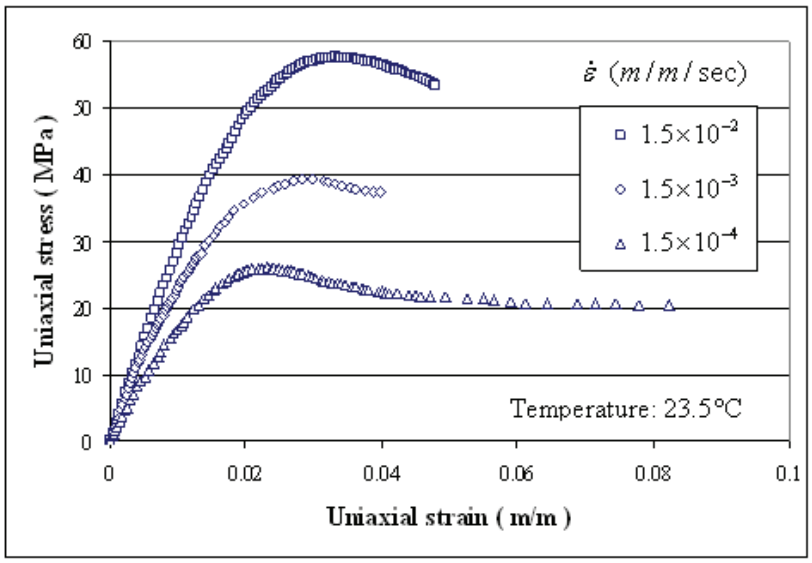

Fig. 6-1 Stress-strain relation of epoxy under different strain rates (test data)

Therefore cohesive layer thickness h_c can be obtained from Eq. (6-1) if the fracture energy 2Γ or work-of-separation ϕ_{sep}, which is the energy necessary to generate unit debond length, is known from experiment or analytical methods.

6.3 Nonlinear Viscoelastic Model and Fracture Energy

A linear viscoelastic model is described in Chapter V, material constitutive equations are listed in Eqs. (5-7, 5-8) and the time-dependent material properties can be expressed with Prony series as shown in Eqs. (5-9, 5-10).

A nonlinear viscoelastic model for the bulk adhesive using modified free volume approach [47] was also implemented in the code. A strain-based formulation proposed by Popelar and Liechti [48] entails a nonlinear shift-factor based on free-volume given by,

$$Log(a) = -\frac{B_d}{2.303 f_d}\left(\frac{\alpha_v \Delta T + \beta_v \Delta c + \delta\theta}{f_d + \alpha_v \Delta T + \beta_v \Delta c + \delta\theta}\right) - \frac{B_s}{2.303 f_s}\left(\frac{\varepsilon_{eff}}{f_s + \varepsilon_{eff}}\right) \tag{6-2}$$

The generalized *J*-integral for large deformation with pseudo-stress model proposed by Schapery [49] is also used for fracture modeling,

$$J_v = \int_\Gamma \left[\Phi dy - T_i^R \frac{\partial u_i^R}{\partial x} dL\right] \tag{6-3}$$

For this case, the critical work input required to initiate the crack (or, the fracture initiation energy) can be expressed in terms of the time-dependent far-field parameter J_v.

$$2\Gamma_i = E_R \int_0^t D(t-\tau)\frac{\partial J_v}{\partial \tau} d\tau \tag{6-4}$$

6.4 Moving Wedge Test

To study the properties of polymer adhesive and its debond process under different environmental conditions and strain-rates, a set of moving wedge tests were performed on the interface between the concrete substrate and the epoxy primer (Wedge test was performed by Dr. Liechti and his co-workers at The University of Texas at Austin). As shown in Fig. 6-2, the specimen for moving wedge test consists of essentially two layers of material: a concrete substrate and an epoxy primer layer. Wedge tests were performed under room conditions (temperature 23.5°C and relative humidity 35%).

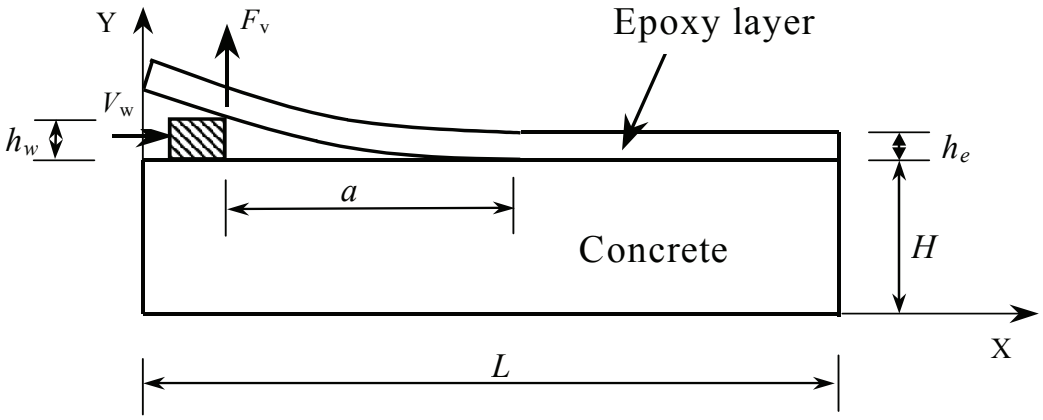

$L = 50mm$, $H = 8mm$, $h_w = 2.0mm$, $h_e = 0.76mm$,

width $B = 18.4mm$, initial $a = 20mm$

Fig. 6-2 Specimen of a moving wedge test

The wedge pushed the epoxy primer coating at a constant wedge speed of $V_w = 0.04mm/\sec$, which is equal to the debond speed during steady debond growth process. The debond length *a*, which is measured from wedge front to debond tip, wedge

displacement, and transverse reaction force F_v were measured as functions of time. The concrete is considered as elastic with a Young's modulus of $37GPa$, and Poisson's ratio of 0.15. The properties of the epoxy in the cohesive layer were obtained using the methodology described below. It should be noted that the FRP layer was not included in the experimental or analytical work presented, because the focus of this research is to obtain the debond strength between the epoxy and the concrete substrate.

6.5 Numerical Simulation of Wedge Test

The proposed cohesive layer model with hygrothermal effect and cohesive layer failure was implemented in a test-bed finite element code (NOVA-3D). Wedge test simulations were successfully conducted with the code and were benchmarked with mixed mode fracture experiments.

A strong time-dependent effect in the epoxy primer was revealed in the wedge tests. In the numerical simulation of wedge tests, the epoxy primer layer was considered as a viscoelastic continuum with time-dependent behavior. At room temperature the viscoelastic material properties, bulk relaxation modulus $K(t)$ and shear relaxation modulus $\mu(t)$, can be expressed with Prony Series, and the Prony Series coefficients are listed in Table 5-3. Test results of steady state debond length and transverse reaction force are shown in Fig. 6-3 and Fig. 6-4. During steady state debond growth, constant debond length $a = 5.5mm$ and vertical reaction force $F_v = 40.0N$.

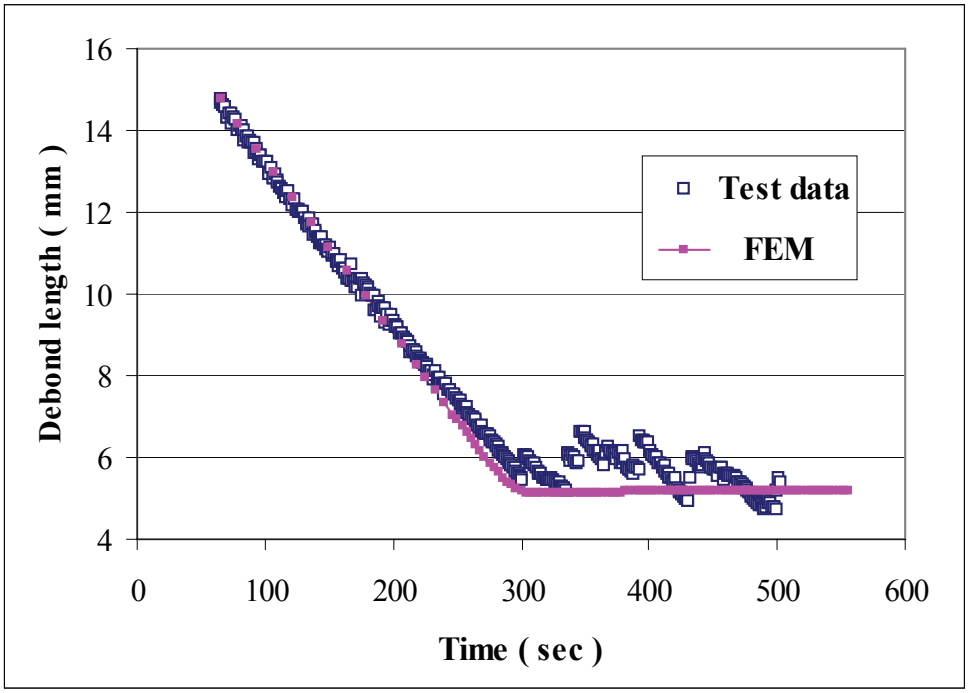

Fig. 6-3 Debond length vs. time (test result and FEA prediction)

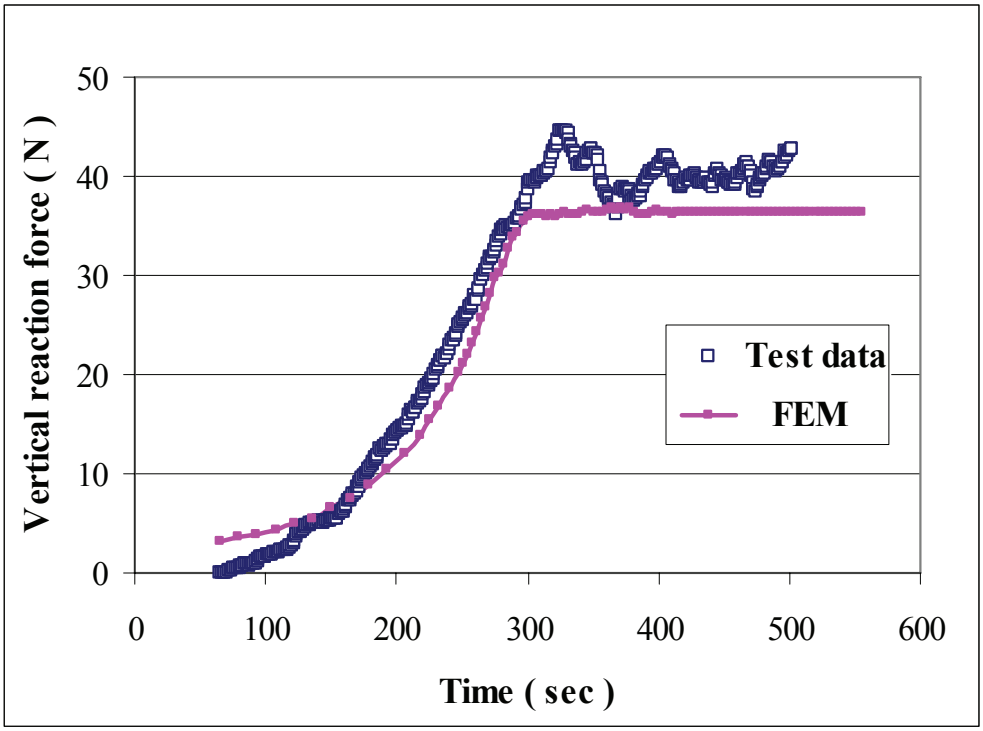

Fig. 6-4 Vertical reaction force vs. time (test result and FEA prediction)

Material properties of the epoxy primer were also tested under different strain rates as shown in Fig. 6-1. Maximum stress σ_{max} under different strain rate and the corresponding strain ε_0, which is the strain at $\sigma = \sigma_{max}$, were extracted from the test curves. According to the cubic traction-separation law for cohesive layer model (shown in Fig. 2-3) maximum strain can be obtained by $\varepsilon_{max} = 3\varepsilon_0$.

Base on the extracted material properties (listed in Table 6-1), the strain rate-dependent traction-separation law for cohesive layer model can be determined under a given strain rate.

Table 6-1 σ_{max} and ε_{max} under different strain rate $\dot{\varepsilon}$

$\dot{\varepsilon}$ $(m/m/\sec)$	σ_{max} (MPa)	ε_0 $(at\ \sigma = \sigma_{max})$	$\varepsilon_{max} = 3\varepsilon_0$
0.00015	26	0.025	0.075
0.0015	38	0.030	0.090
0.015	57	0.035	0.105

FEA simulation of debond growth:

(a). Determination of fracture energy:

Under the measured wedge speed or debond speed at steady stage $da/dt = V_w = 4\times10^{-5}\, m/\sec$, the corresponding fracture energy $2\Gamma = 463 J/m^2$ was obtained by means of a linear fit to the test data shown in Fig. 6-5.

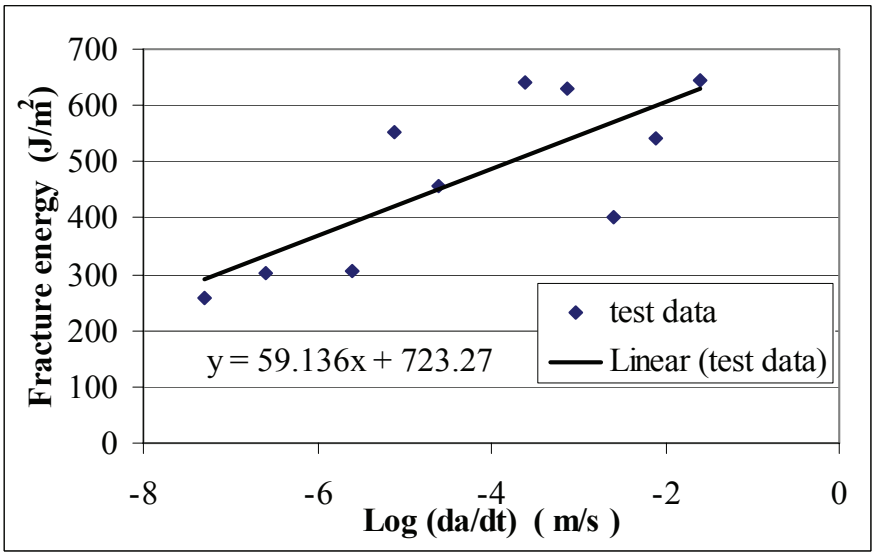

Fig. 6-5 Fracture energy 2Γ vs. debond speed

(b). Estimation of the average transverse strain rate in cohesive layer:

Stress-strain relation of the epoxy primer changes significantly with applied strain-rate (Fig. 6-1). To determine the material properties, transverse strain rate in the cohesive layer during the loading process of the wedge test must be determined. Unfortunately, transverse strain rate in cohesive layer is hard to measure during a wedge test, as it changes with location and time, and is affected by cohesive layer thickness. From FEA results, the average transverse strain rate was found to depend on the debond-speed as given by $\dot{\varepsilon} = p\dfrac{da}{dt}$, with the coefficient $p \approx 10$. Therefore, the estimated average strain rate is $\dot{\varepsilon} \approx 0.0004 m/m/\sec$ for the case of wedge speed or debond speed $da/dt = V_w = 4\times10^{-5}\, m/\sec$.

(c). Determination of the traction-separation law of the cohesive layer:

From the strain rate ($\dot{\varepsilon} \approx 0.0004 m/m/\sec$) derived in the previous section, linear interpolation of the data in Table 6-1 gives,

$$\sigma_{\max} = \tau_{\max} = 31.4 MPa$$

$$\varepsilon_{\max} = \gamma_{\max} = 0.081$$

(d). Determination of cohesive layer thickness:

Only vertical reaction force, the load applied on epoxy primer by wedge at the point of contact, is considered in the present FEA simulation. Actually, horizontal reaction force does exist in the wedge tests between the wedge and epoxy primer due to friction, and this force would weaken the effect of shear stress on the debond process.

The failure criterion for the cohesive layer expressed in Eq. (6-1) is employed in this example. Based on the fact that the shear strain near the debond tip was almost twice as large as the normal strain, $\alpha = 0.5$ and $\beta = 1.0$ were selected for the cohesive layer simulation model. From this, the cohesive layer thickness to be used in the analysis, $h_c = 0.288 mm$, was obtained.

(e). FEA simulation of wedge-test:

Once the traction-separation law and the cohesive layer thickness were determined, FEA simulations could be performed. FEA mesh employed for wedge test simulation is shown in Fig. 6-6.

Predicted debond length and transverse reaction force histories are shown in Fig. 6-3 and Fig. 6-4 for comparison with measured data. At the time $t = 500 \sec$, the wedge front entered the interface zone that was originally bonded, and after that time steady debond growth was observed. Debond length and vertical reaction force were 5.7 mm and 35.5 N respectively at steady-state debond growth, which compares well with the test

data, 5.5 mm and 40.0 N, as shown in Fig.6-3 and Fig. 6-4, respectively. The differences between FEA solutions and test results are probably due to the error in the estimated average strain rate in the cohesive layer and the effect of horizontal reaction force which was ignored in the analysis.

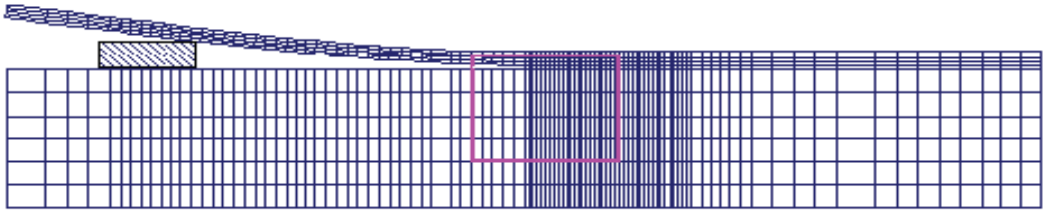

Fig. 6-6 FEA mesh and contour for *J*-integral

Table 6-2 FEA results with various wedge speeds

$V_w = \frac{da}{dt}$ $(m/\sec)$	4×10^{-6}	4×10^{-5}	4×10^{-4}	4×10^{-3}
2Γ (J/m^2)	404	463	522	581
$\dot{\varepsilon}$ $(m/m/\sec)$	0.00004	0.0004	0.004	0.04
$\sigma_{\max} = \tau_{\max}$ (MPa)	15.9	31.4	46.9	62.4
$\varepsilon_{\max} = \gamma_{\max}$ (m/m)	0.066	0.081	0.096	0.111
h_c (mm)	0.608	0.288	0.183	0.133
a (mm)	5.4	5.7	6.0	6.2
F_v (N)	30.6	35.5	38.5	39.6

Wedge tests with various wedge speeds were simulated by the FEA code, and the results are listed in Table 6-2. It can be observed that steady state debond length and reaction force increase with increase in the wedge speed or debond speed.

6.6 Conclusions

A two-dimensional cohesive layer constitutive model with a prescribed traction-separation law is constructed from fundamental principles of continuum mechanics and thermodynamics, taking into account strain-dependent, non-Fickian hygrothermal effects as well as diffusion induced degradation in the cohesive layer. The influence of temperature and moisture concentration on the work-of-separation and on crack growth is derived from first-principles. The model is implemented in a test-bed finite element code and code verification was performed. Results predicted by the computational model are benchmarked through comparison with analytical solutions and mixed mode fracture test. Steady debond growth was obtained after the wedge front enters the originally bonded area, and this is consistent with the observations from wedge tests. Rate-dependent behavior in the cohesive layer was implemented through the characterization of rate-dependence of the maximum stresses and maximum strains in the cohesive layer as presented in Table 6-1.

From the simulation results it can be concluded that stress-strain relation of cohesive layer is obviously rate-dependent and the cohesive layer thickness is an important characteristic parameter of the cohesive layer model, and it is quite sensitive to the fracture toughness and the stress-strain relation of cohesive material. Simulation of wedge tests under different wedge speeds was also presented to demonstrate the rate-

dependent behavior of cohesive layer model and the ability of the cohesive layer model to simulate transient as well as steady-state debond growth at various strain rates.

CHAPTER VII

FRP BONDED STRUCTURE UNDER BLAST LOAD

The objective of this chapter is to study the dynamic responses of fiber reinforced polymer (FRP) bonded structure under blast load by means of cohesive layer model. An exponential distribution of blast pressure was used in the simulation to solve the equations of motion. Long term and short term dynamic responses were obtained and their effects on the failure of the cohesive layer were investigated. This chapter is only a preliminary study, more work needs to be done to address the dynamic debond of FRP structure under blast load.

7.1 Introduction

A structure may experience blast load due to military actions, accidental explosions or terrorist activities. Such load may cause severe damage or collapse due to their high intensity, dynamic nature, and usually different direction compared to common design load [50]. Collapse of one structural member in the vicinity of the source of the explosion, may then create critical stress redistributions and lead to collapse of other members, and eventually, of the whole structure. One example of such a failure is the well-known collapse of the Alfred P. Murrah Federal Building in Oklahoma City, Oklahoma, following a terrorist attack [51, 52].

For some structures blast-resistant design may be required, if their use is such that there is a high risk for such a blast loading incident to be encountered. For such structures, it is desirable to establish design procedure and construction techniques necessary to achieve the required strength to resist the applied blast loads.

The problem can be tackled in several different ways. The approach that more accurately describes the dynamic response of structure to explosive loads is via numerical analysis, usually by means of finite element method. Such analysis can capture the geometry of the structure, the spatial and temporal distribution of the applied blast pressure, as well as the effects of material and geometric nonlinearity, in a satisfactory manner [53, 54].

Fiber reinforced polymer (FRP) bonded structures have been widely used in defense industry and civil engineering for infrastructure repair and retrofit. Not much study on the dynamic response of FRP bonded structures has been conducted, and the dynamic response and failure mechanism of the adhesive layer under blast loading are not clear. This preliminary study focuses on the dynamic response of FRP bonded structure under blast loads by means of cohesive layer model.

7.2 Implicit Integration Methods

The equation of motion for linear structural dynamic problems after spatial description by finite element method can be written as

$$\boldsymbol{M}\ddot{\boldsymbol{U}} + \boldsymbol{C}\dot{\boldsymbol{U}} + \boldsymbol{K}\boldsymbol{U} = \boldsymbol{R} \tag{7-1}$$

where $\boldsymbol{M}$, $\boldsymbol{K}$, $\boldsymbol{C}$ are the system mass matrix, stiffness matrix and damping matrix, $\boldsymbol{R}$ is the externally applied force vector, $\boldsymbol{U}$, $\dot{\boldsymbol{U}} = \frac{d\boldsymbol{U}}{dt}$, and $\ddot{\boldsymbol{U}} = \frac{d^2\boldsymbol{U}}{dt^2}$ are the unknown displacement, velocity, and acceleration vectors, respectively, which generally are functions of time t.

For transient response analysis, the initial conditions at $t = 0$ are given by

$$\boldsymbol{U}\big|_{t=0} = \boldsymbol{u}_0$$

$$\dot{\boldsymbol{U}}\big|_{t=0} = \boldsymbol{v}_0 \tag{7-2}$$

$$\ddot{\boldsymbol{U}}\big|_{t=0} = \boldsymbol{a}_0$$

Base on the known solution at time t, direct integration method can be applied to obtain the solution at time $t + \Delta t$, where Δt is the given discrete time interval. The commonly used effective direct integration methods can be classified into two categories: explicit integration method and implicit integration method. Explicit integration method (e.g. the central difference method) is based on using the equilibrium conditions at time t (Eq. 7-1) to seek the solution at time $t + \Delta t$. On the other hand, implicit integration method including the Houbolt, Wilson, Newmark and HHT methods, which will be introduced in the following sections, uses the equilibrium conditions at time $t + \Delta t$.

7.2.1 Houbolt Method

Focusing attention on the inertial class of dynamical elasticity problems, implicit methods are attractive (although some analysts prefer explicit methods). The implicit Houbolt method [55] was developed in 1950 and is one of the earliest employed for the

calculation of the structural response of an airplane subjected to dynamic loads. It uses the concept of displacement difference equivalents to approximate the velocity and acceleration components, and thereby establishes a recurrence relation that can be used to solve for the step-by-step response of the structure as shown in Eq. (7-3, 7-4). In Houbolt method, the generality and physical aspects of the basic equilibrium are preserved. It's a two-step backward difference method. From a stability and accuracy point of view, it is unconditionally stable, second-order accurate, and is not suitable for higher frequency dynamic problems.

$$\ddot{\boldsymbol{U}}^{t+\Delta t} = \frac{1}{\Delta t^2}(2\boldsymbol{U}^{t+\Delta t} - 5\boldsymbol{U}^{t} + 4\boldsymbol{U}^{t+\Delta t} - \boldsymbol{U}^{t-2\Delta t}) \tag{7-3}$$

$$\dot{\boldsymbol{U}}^{t+\Delta t} = \frac{1}{6\Delta t}(11\boldsymbol{U}^{t+\Delta t} - 18\boldsymbol{U}^{t} + 9\boldsymbol{U}^{t-\Delta t} - 2\boldsymbol{U}^{t-2\Delta t}) \tag{7-4}$$

7.2.2 Newmark Method

In 1959, Newmark [56] introduced an implicit method of computation for the solution of problems in structural dynamics, which is perhaps the most popular algorithm for numerical solutions of structural dynamic problems. The algorithm assumes that the average acceleration is constant over an integration time step

$$\boldsymbol{M}\ddot{\boldsymbol{U}}^{t+\Delta t} + \boldsymbol{K}\boldsymbol{U}^{t+\Delta t} = \boldsymbol{R}^{t+\Delta t} \tag{7-5}$$

$$\dot{\boldsymbol{U}}^{t+\Delta t} = \dot{\boldsymbol{U}}^{t} + \left[(1-\delta)\ddot{\boldsymbol{U}}^{t} + \delta\ddot{\boldsymbol{U}}^{t+\Delta t}\right]\Delta t \tag{7-6}$$

$$\boldsymbol{U}^{t+\Delta t} = \boldsymbol{U}^{t} + \dot{\boldsymbol{U}}^{t}\Delta t + \left[(\frac{1}{2}-\alpha)\ddot{\boldsymbol{U}}^{t} + \alpha\ddot{\boldsymbol{U}}^{t+\Delta t}\right]\Delta t^2 \tag{7-7}$$

There are two free parameters δ and α which control the stability and accuracy of the algorithms. The algorithm is first-order accurate, unconditionally stable and

dissipative if the parameters satisfy the relation $2\alpha \geq \delta > \frac{1}{2}$. For the algorithm to be accurate to second order and unconditionally stable, $\delta = \frac{1}{2}$ and $\alpha \geq \frac{1}{4}$ are required. However, then it is non-dissipative.

7.2.3 Wilson-θ Method

The Wilson-θ method [57] is essentially an extension of the average acceleration approximation in which the variation between time t and $t+\Delta t$ is assumed to be linear. In particular, the Wilson-θ method assumes that the acceleration is linear between t and $t+\theta\Delta t$, with $\theta \geq 1.0$. It is indicated that when $\theta =$ 1.4 the obtained solution is most accurate and stable.

$$\ddot{\boldsymbol{U}}^{t+\tau} = \ddot{\boldsymbol{U}}^{t} + \frac{\tau}{\theta\Delta t}(\ddot{\boldsymbol{U}}^{t+\theta\Delta t} - \ddot{\boldsymbol{U}}^{t}) \tag{7-8}$$

$$\dot{\boldsymbol{U}}^{t+\tau} = \dot{\boldsymbol{U}}^{t} + \ddot{\boldsymbol{U}}^{t}\tau + \frac{\tau^2}{2\theta\Delta t}(\ddot{\boldsymbol{U}}^{t+\theta\Delta t} - \ddot{\boldsymbol{U}}^{t}) \tag{7-9}$$

where $\theta \geq 1.0$, and $0 \leq \tau \leq \theta\Delta t$.

The algorithm is second-order accurate, unconditionally stable and dissipative (high frequency numerical dissipation)

7.2.4 HHT Method

To control the algorithmic damping, Hilber, Hughes and Taylor [58] (called HHT method or α -method) made an extension to the Newmark method. With the HHT method it is possible to introduce numerical dissipation (numerical damping) without

degrading the order of accuracy, and this numerical damping can be continuously controlled. Decreasing α implies increasing the numerical damping. This damping is low for low-frequency modes and high for the high-frequency modes.

$$\boldsymbol{M}^{t+\Delta t}\ddot{\boldsymbol{U}}^{t+\Delta t}+(1+\alpha)\boldsymbol{K}^{t+\Delta t}\boldsymbol{U}^{t+\Delta t}-\alpha\boldsymbol{K}^{t}\boldsymbol{U}^{t}=\boldsymbol{R}^{t+\Delta t} \tag{7-10}$$

$$\dot{\boldsymbol{U}}^{t+\Delta t}=\dot{\boldsymbol{U}}^{t}+\left[(1-\gamma)\ddot{\boldsymbol{U}}^{t}+\gamma\ddot{\boldsymbol{U}}^{t+\Delta t}\right]\Delta t \tag{7-11}$$

$$\boldsymbol{U}^{t+\Delta t}=\boldsymbol{U}^{t}+\dot{\boldsymbol{U}}^{t}\Delta t+\left[(\frac{1}{2}-\beta)\ddot{\boldsymbol{U}}^{t}+\beta\ddot{\boldsymbol{U}}^{t+\Delta t}\right]\Delta t^{2} \tag{7-12}$$

It is second-order accurate and unconditionally stable if $\beta=\frac{1}{4}(1-\alpha)^2$, $\gamma=\frac{1}{2}-\alpha$, and $-\frac{1}{3}\le\alpha\le 0$.

When considering physical damping, the HHT method can be expressed as

$$\boldsymbol{M}^{t+\Delta t}\ddot{\boldsymbol{U}}^{t+\Delta t}+(1+\alpha)\boldsymbol{C}^{t+\Delta t}\dot{\boldsymbol{U}}^{t+\Delta t}-\alpha\boldsymbol{C}^{t}\dot{\boldsymbol{U}}^{t}+(1+\alpha)\boldsymbol{K}^{t+\Delta t}\boldsymbol{U}^{t+\Delta t}-\alpha\boldsymbol{K}^{t}\boldsymbol{U}^{t}=\boldsymbol{R}^{t+\Delta t} \tag{7-13}$$

or

$$\boldsymbol{M}^{t+\Delta t}\ddot{\boldsymbol{U}}^{t+\Delta t}+(1+\alpha)\boldsymbol{C}^{t+\Delta t}\dot{\boldsymbol{U}}^{t+\Delta t}-\alpha\boldsymbol{C}^{t}\dot{\boldsymbol{U}}^{t}+(1+\alpha)\boldsymbol{F}^{t+\Delta t}-\alpha\boldsymbol{F}^{t}=\boldsymbol{R}^{t+\Delta t} \tag{7-14}$$

Where vector $\boldsymbol{R}^{t+\Delta t}$ is the externally applied nodal force in the configuration at time $t+\Delta t$, the vector $\boldsymbol{F}^{t}$ and $\boldsymbol{F}^{t+\Delta t}$ are the nodal point force that corresponding to the element stress in this configuration at time t and $t+\Delta t$, respectively. When $\alpha=0$ the HHT method is reduced to the Newmark method.

Under given initial conditions as shown in Eq. (7-2) and ignoring physical damping, dynamic equilibrium equations can be solved by HHT method as follows:

$$\boldsymbol{U}^{t+\Delta t}=\left(\frac{1}{\beta\Delta t^2}\boldsymbol{M}+(1+\alpha)\boldsymbol{K}^{t+\Delta t}\right)^{-1}\left[\boldsymbol{R}^{t+\Delta t}+\left(\frac{1}{\beta\Delta t^2}\boldsymbol{M}+\alpha\boldsymbol{K}^{t}\right)\boldsymbol{U}^{t}+\frac{1}{\beta\Delta t}\boldsymbol{M}\dot{\boldsymbol{U}}^{t}+\left(\frac{1}{2\beta}-1\right)\boldsymbol{M}\ddot{\boldsymbol{U}}^{t}\right]$$

$$\ddot{\boldsymbol{U}}^{t+\Delta t}=\frac{1}{\beta\Delta t^2}\left(\boldsymbol{U}^{t+\Delta t}-\boldsymbol{U}^{t}\right)-\frac{1}{\beta\Delta t}\dot{\boldsymbol{U}}^{t}-\left(\frac{1}{2\beta}-1\right)\ddot{\boldsymbol{U}}^{t} \tag{7-15}$$

$$\dot{\boldsymbol{U}}^{t+\Delta t}=\dot{\boldsymbol{U}}^{t}+\left[(1-\gamma)\ddot{\boldsymbol{U}}^{t}+\gamma\ddot{\boldsymbol{U}}^{t+\Delta t}\right]\Delta t$$

7.3 Blast Load

A typical blast loading pressure applied on an object can be characterized by its peak reflected pressure P_r and positive phase duration t_d. The peak overpressure of blast loading can be empirically expressed as [59],

$$P_r=\frac{139.97}{Z}+\frac{844.81}{Z^2}+\frac{2154}{Z^3}-0.8034 \qquad KPa \tag{7-16}$$

where $Z=\frac{R}{\sqrt[3]{W}}$ is called the scaled distance, R is the distance from the center of a spherical charge (point source) in meter and W is the charge mass expressed in kilograms of equivalent TNT, as illustrated in Fig.7-1.

The time history of the pressure is very often simplified into a triangular distribution when ignoring the negative phase.

$$P(t)=\begin{cases}P_r\left(1-\dfrac{t}{t_d}\right), & 0\le t<t_d\\ 0, & t<0 \quad or \quad t\ge t_d\end{cases} \tag{7-17}$$

The evolution of blast load pressure P with time t can be simulated more accurately by an exponential distribution [60], which is adopted in the present study.

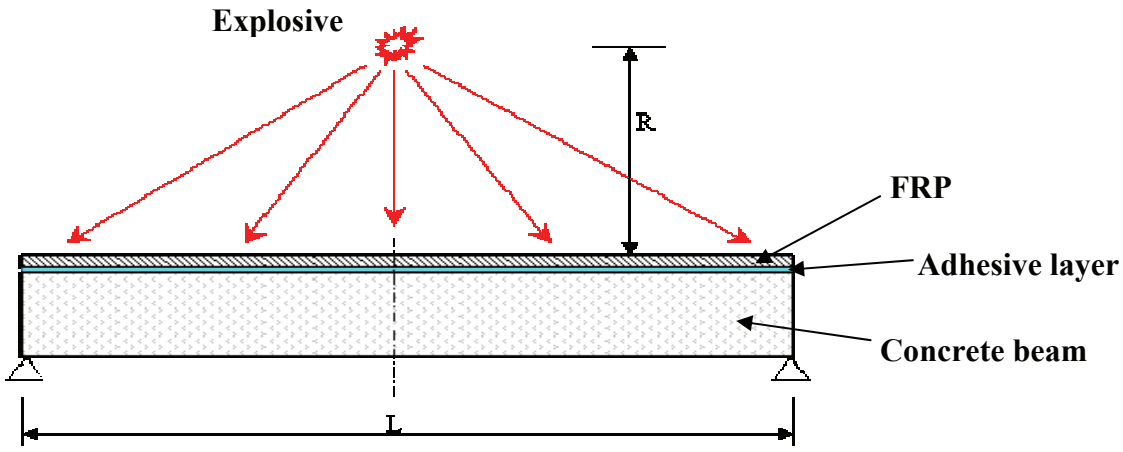

Fig. 7-1 A simply supported concrete beam bonded with FRP under blast load

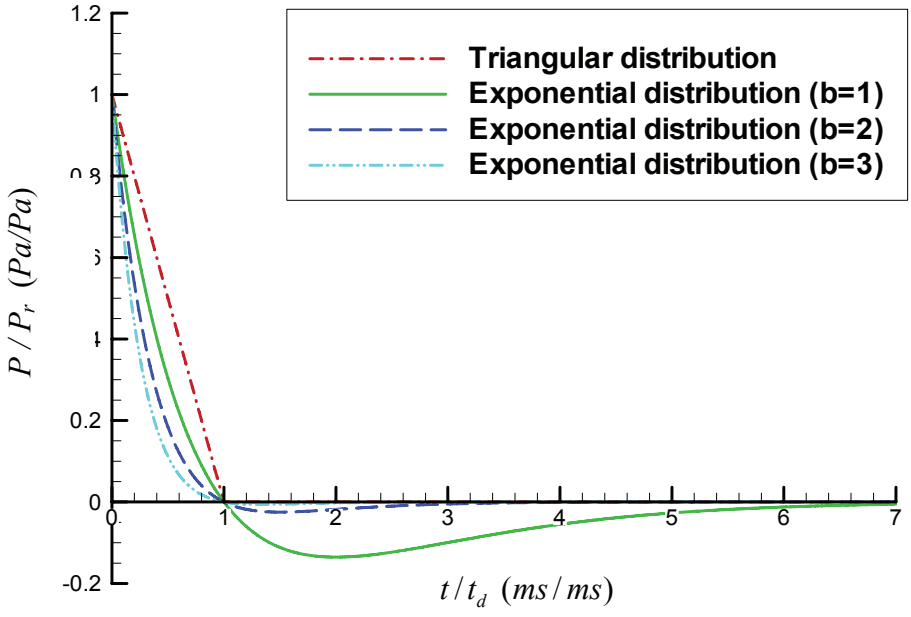

Fig. 7-2 Triangular and exponential distributions of blast load

$$P(t)=\begin{cases} P_r\left(1-\dfrac{t}{t_d}\right)e^{-bt/t_d} & , \quad t\geq 0 \\ 0 & , \quad t<0 \end{cases} \tag{7-18}$$

Where t_d is the time of reversal of direction of pressure, and b is a shape parameter depending on the dimensionless scaled distance Z.

Triangular distribution and exponential distribution histories with different shape parameters are shown in Fig. 7-2, and the shape parameter $b=1$ is used in current study.

The blast loading exerts an impulse on the structure, which is equal to the integral of the total external force over time,

$$I=\int_0^{t_d} P(t)dAdt \tag{7-19}$$

The zero-period impulse ($t_d - 0$) results in an initial velocity v_0 (let initial momentum equal to the input impulse I) prescribed throughout the structure.[60]

Impulses of triangular and exponential loading distribution are listed on Table 7-1 (for comparison, only positive phase duration is considered with exponential loading). It can be found that the triangular distribution is of higher impulse than exponential distribution under the same peak pressure and duration time, and thus is more conservative than exponential distribution.

Table 7-1 Impulses of different load distributions

	Triangular distribution	Exponential distribution		
		$b=1$	$b=2$	$b=3$
Impulse ($N\cdot\sec$)	0.5	0.368	0.284	0.228

7.4 Dynamic Response of FRP Bonded Structure

7.4.1 Short Term and Long Term Responses in Cohesive Layer

A simply supported concrete beam with FRP bonded on the top side or on both top and bottom sides is shown in Fig. 7-1. The schematic finite element mesh and corresponding blast load distribution along beam span is shown in Fig. 7-3 (only half structure is modeled due to symmetric conditions). The length of the beam is $L = 2\ m$, height $H_b = 0.1\ m$, and width $B = 1\ m$ (plane strain conditions), thickness of FRP is $h_p = 5\ mm$, and cohesive layer thickness is $h_c = 0.2\ mm$. Material properties of concrete, FRP, and the epoxy layer are listed in Table 7-2. The explosive was placed at the mid-span$1.0\ m$ above the top surface of the beam, the mass of explosive is $0.5\ kg$ TNT, and the duration time of the explosion pressure is $t_d = 1.0\ ms$.

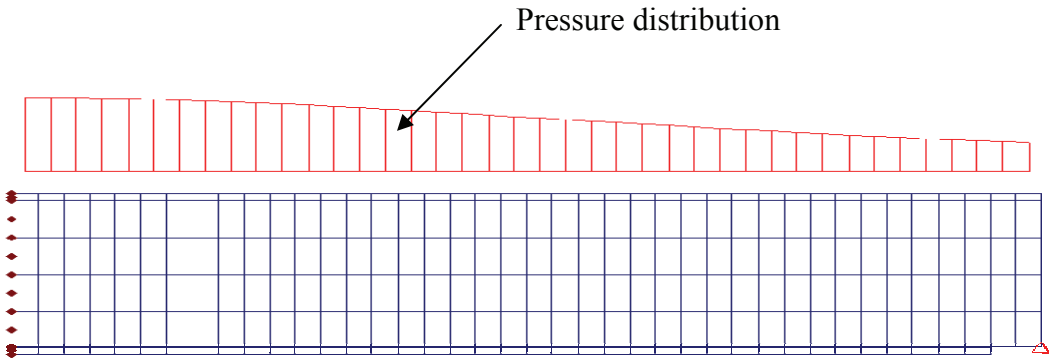

Fig. 7-3 Schematic FEA mesh and distribution of blast load along the beam

Table 7-2 Material properties of concrete, epoxy adhesive and FRP

	Concrete	Epoxy	FRP
Young's Modulus (GPa)	27.5	3.85	3.43
Shear Modulus (GPa)	11.0	1.54	1.29
Poisson's Ratio	0.25	0.25	0.33
σ_{max} (MPa)	--	30.0	--
ε_{max} (m/m)	--	0.0526	--
Density (Kg/m^3)	2500	1100	1600

Two different kinds of responses of FRP plate bonded concrete beam under blast load were observed form the FEA simulation results. One is at the very beginning of the explosion (e.g. $t < 3t_d$), especially within the positive phase $t \leq t_d$. During this period, intense blast load is applied on the beam and results in a forced vibration. This period is too short to allow significant bending displacement or other displacement to develop in the beam. Therefore the only stress component in the cohesive layer is the vertical stress σ_y due to the propagation of stress wave (tensile and compressive vibration in y direction) and the frequencies of vibrations in this direction are much higher than that of bending vibrations. Very small time step ($\Delta t = 0.2 \sim 1.0 \mu s$) was employed in the simulation to capture the stress wave propagating along the height of the beam and reflecting at the top and bottom surfaces of the beam or at the bi-material interfaces. It can be clearly seen in Fig. 7-4 that σ_y decrease with time due to numerical damping of high frequency components by the HHT method used in the simulation.

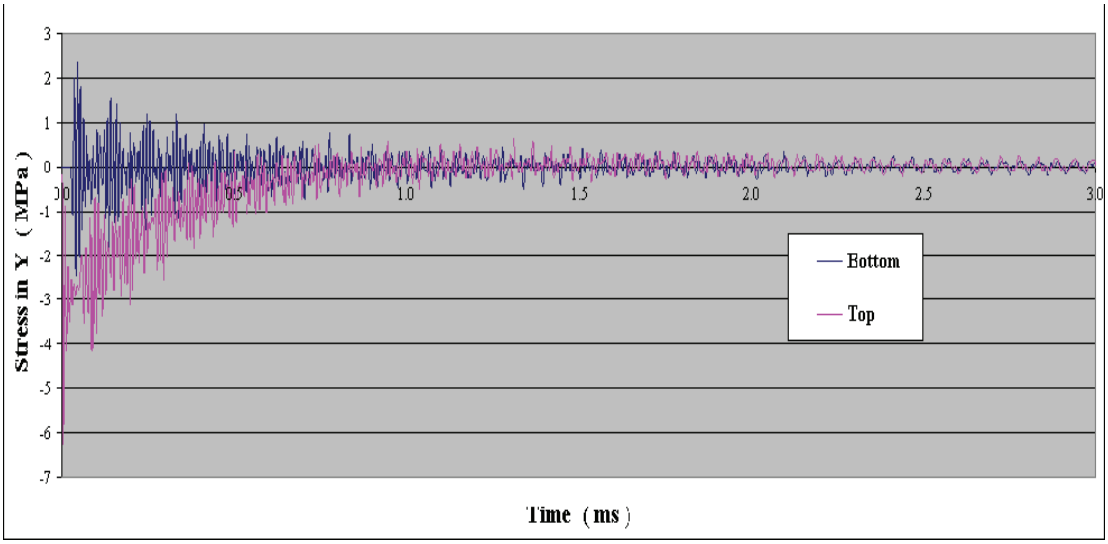

Fig. 7-4 Short term response c_y in the top and bottom cohesive layers at mid-span

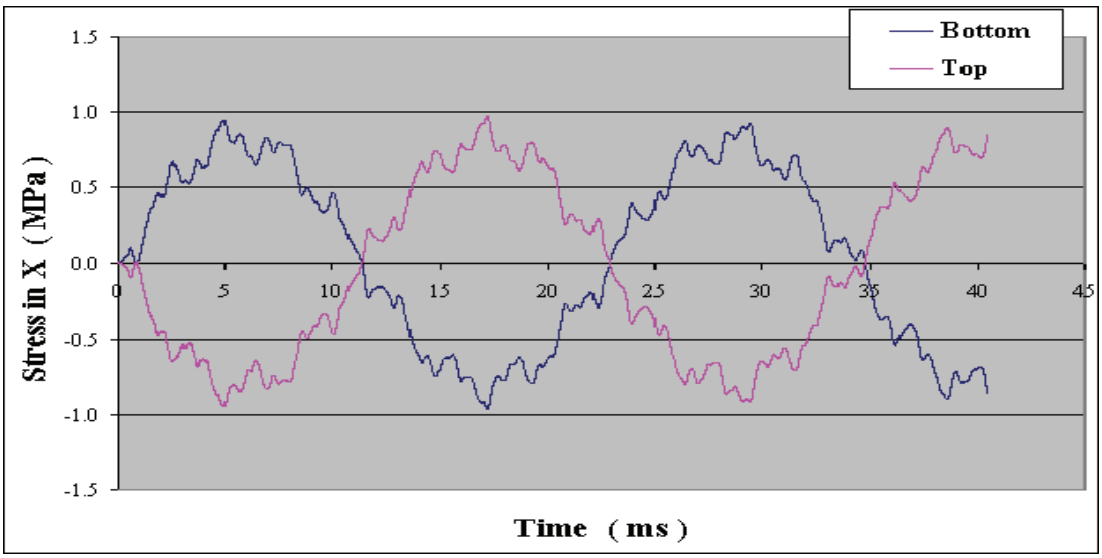

Fig. 7-5 Long term response c_x in the top and bottom cohesive layer at mid-span

After the initial period, blast pressure load decreases with time, at the same time vertical stress c_y also decays because of energy dissipation. When the external load is small enough, stable free vibration (bending deformation) will occur with relatively lower

frequencies. In this period, the dominant stress in cohesive layer is σ_x which is caused by bending deformation while transverse stress σ_y and shear τ_{xy} is relatively small. Large time steps ($\Delta t = 1.0 \sim 20.0 \mu s$) were employed to simulate the bending vibration of the beam and the bending stress σ_x history is shown in Fig. 7-5. It was found that numerical damping is not significant in the relatively low frequency bending vibration.

7.4.2 Critical Debond Locations of FRP Bonded Beam

As discussed in the previous section, there are two sorts of dynamic responses under blast load. Considering the short term response, the distribution of vertical stress σ_y in cohesive layer along the beam is shown in Fig. 7-6. The stress component near the end of the beam is only $\frac{1}{3}$ of that at mid-span. Even considering the moisture degradation of the cohesive layer near the end of the beam, debond is not likely to occur in this area. Therefore debond near the mid-span is the likely failure location for simply supported beam due to the short term response.

As for long term response, bending stress σ_x is negligible at the end of the beam according to the theory of beam and FEA simulation in this study pointed the same result. FEA result of the distribution of stress component σ_x along the beam is shown in Fig. 7-7. Obviously we can conclude that debond is not likely to occur at the end of the beam. The possible debond locations of the FRP bonded beam are near the mid span where the stress components σ_x and σ_y are relatively high under both long term and short term responses.

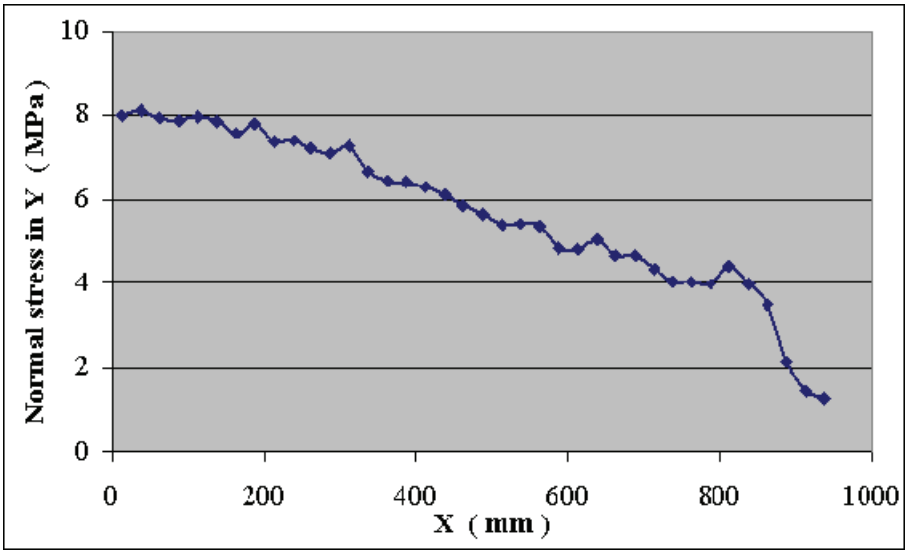

Fig. 7-6 Typical distribution of stress σ_y in a cohesive layer

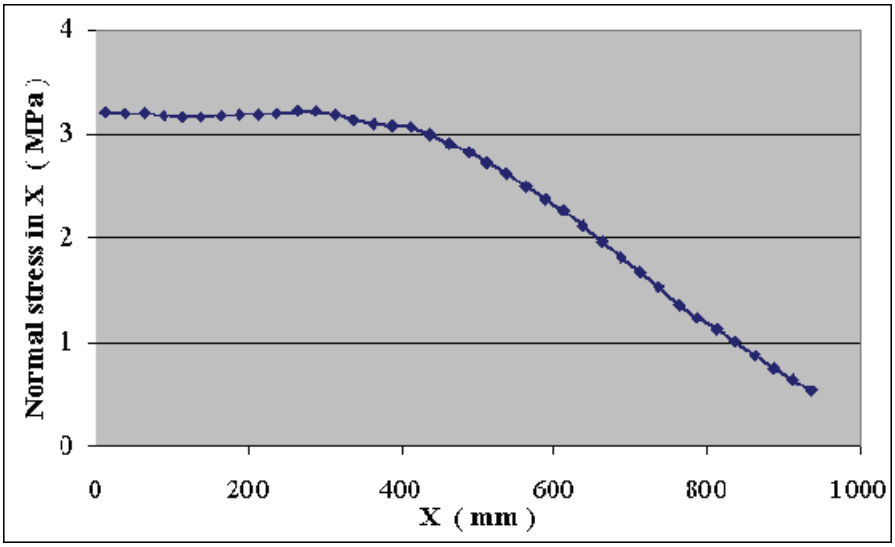

Fig. 7-7 Typical distribution of stress σ_x in a cohesive layer

7.4.3 Explosive at Different Locations

Any load can be decomposed to a sum of a symmetrical load and a skew symmetrical load. The symmetric portion will excite the first mode vibration and other

symmetrical modes (for simply supported beam, the first mode is a symmetric mode). The skew symmetrical portion will excite the second mode vibration and other skew symmetrical modes.

The FEA mesh and load distribution of a simply supported beam under off-center load are shown in Fig. 7-8. The amplitude limits of stress σ_x for explosive loaded at different locations along the beam span are shown in Fig. 7-9. We find that when the explosive is located near mid span, the maximum stress of σ_x occurs at mid span. As location of explosive is moved from mid span towards the end of the beam, σ_x at mid span will decrease while σ_x near $\frac{1}{4}$ span will increase. When the explosive is close to the end (less than $\frac{1}{8}$ span) the overall load acting on the beam decreases very fast, which results in a decrease of the dynamic response. We also find that the maximum dynamic response will be obtained near $\frac{1}{4}$ span of the loading side when the explosive is located between $\frac{1}{8}$ span and $\frac{1}{4}$ span.

For the short term response, the maximum value of transverse peel stress, σ_y, mainly depends on the applied peak pressure P_{cr}, and the location of the maximum σ_y usually occurs directly below the explosive. Therefore the location of maximum σ_y will change with the location of the explosive.

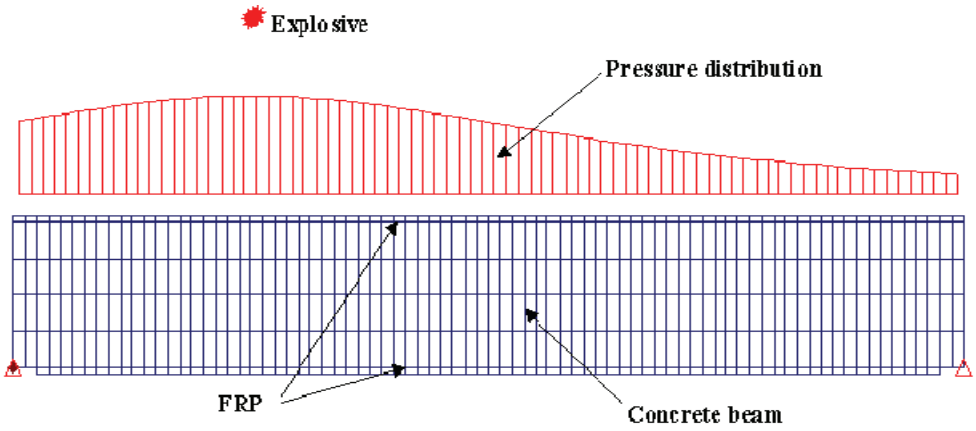

Fig. 7-8 FEA mesh f a simply supported beam under off side load

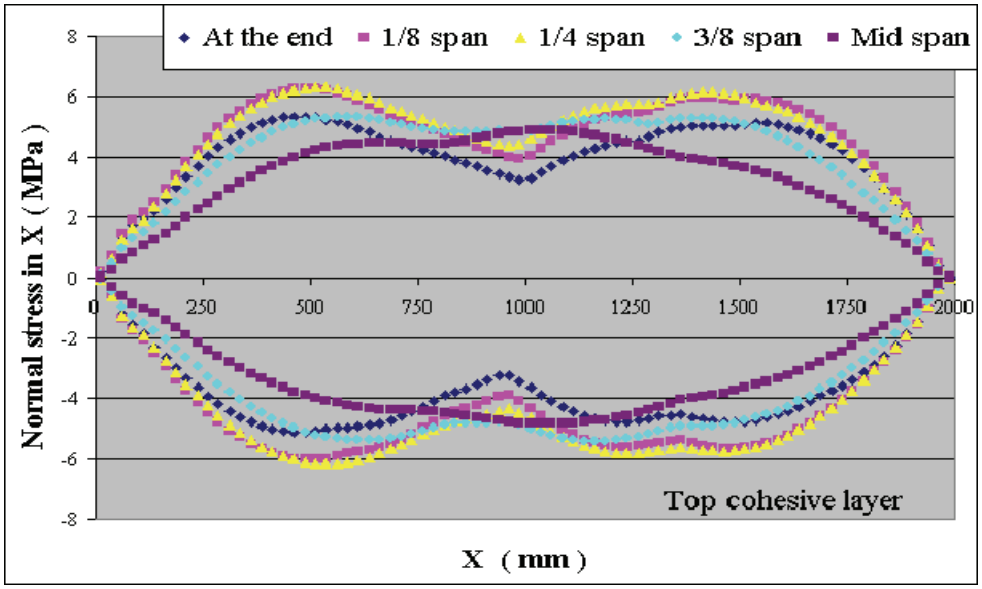

Fig. 7-9 Stress limits of c_x as function of explosive location along beam axis

7.4.4 Concrete Beam with Initial Cracks

Cracks usually exist in most concrete structures during their service life. A demonstration example was study in this simulation to investigate the effect of the cracks

in the concrete beam on the failure of cohesive layer. A single vertical crack with a length of $\frac{1}{4}$ beam height is introduced in the concrete beam as shown in Fig. 7-10.

To clearly depict the effect of the crack, the crack was suddenly introduced at a certain time after the blast load is applied on the beam. Significant changes in the stress were found in those adhesive elements near the crack. Normal stress σ_x in element 1 (Fig. 7-11) and shear stress τ_{xy} in element 2 (Fig. 7-12) experience a big jump when a crack was introduced in concrete beam. These high level stresses would likely induce a mode I or mode II debond initiation and propagation in the cohesive layer.

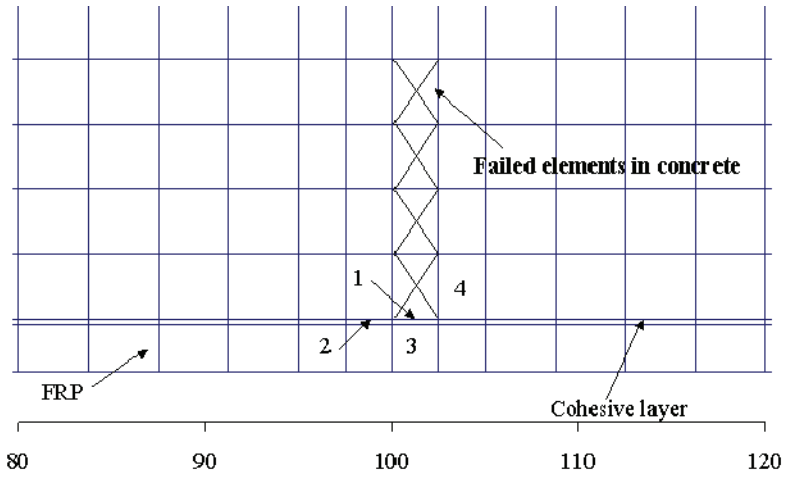

Fig. 7-10 A simply supported FRP bonded beam with an initial crack in concrete

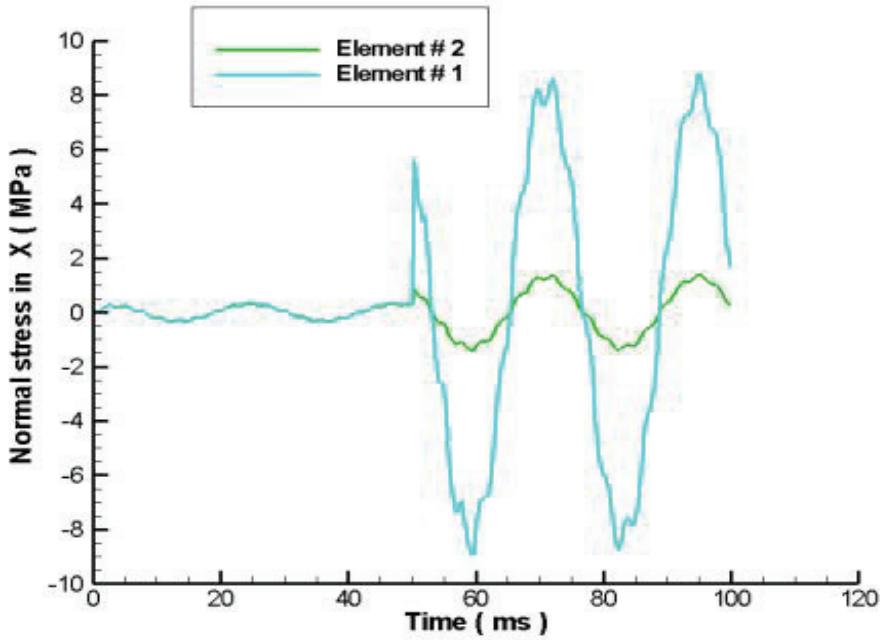

Fig. 7-11 Comparison of axial stress σ_x in the cohesive layer before and after concrete cracking (Cracking occurred at $t = 50ms$)

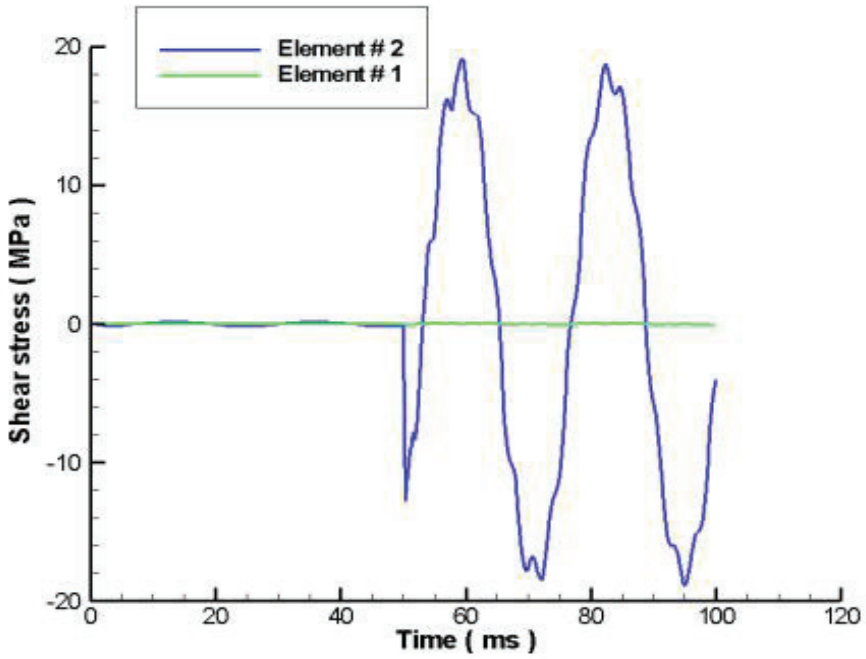

Fig. 7-12 Comparison of shear stress τ_{xy} in the cohesive layer before and after concrete cracking (Cracking occurred at $t = 50ms$)

7.5 Conclusions

For this preliminary study, cohesive layer model under blast load was constructed and implemented into a test-bed FEA code. Implicit HHT method was used in the model to allow better control of numerical damping. Long term responses and short term responses were obtained and their contributions to the debond processes in the cohesive layer were found to be significantly different. Introduction of a crack in the concrete would induce stress concentrations near the crack tip and result in debond initiation in the vicinity of the crack.

CHAPTER VIII

DYNAMIC ANALYSIS WITH MATERIAL AND GEOMETRIC NONLINEARITY

The objective of this chapter is to study the dynamic responses of structures with very large transient displacement and deformation under blast loading. A two-dimensional implicit dynamic finite element formulation including material and geometric nonlinearity was derived and implemented into a test-bed FEA code (NOVA-3D). Model verification was successfully performed through comparison with ABAQUS FEA predictions. Subsequently, the NOVA-3D FEA model was applied to a circular steel plate with a polymer coating subjected to intensive blast loading, and the effect of polymer coating on the nonlinear dynamic response was numerically investigated.

8.1 Modeling of Material and Geometric Nonlinearity

Dynamic loading of structures often cause excursions of stresses well into the inelastic range and the influence of geometry changes on nonlinear response is also significant in many cases. Blast loading applied on a structure usually results in very large displacement and deformation in a short period of time, which also implies a very high strain rate in the structure. Therefore both material and geometric nonlinear effects need to be considered when evaluating the dynamic response under blast load.

8.1.1 Material Nonlinearity

Material behavior under dynamic loading is very complex and experimental information is limited. For example, the instantaneous yield stress is significantly influenced by the rate of strain. Also, the value of the elastic modulus is sometimes found to be dependent on the strain rate. Stress wave generated by dynamic loading usually causes high stress levels and therefore results in significant plastic deformation in the structure. However, in the current study, due a lack of experimental data, we assume that the material properties are rate independent while incorporating elasto-plastic material behavior in the test-bed FEA code.

The situation is complicated by the fact that different classes of materials exhibit different elasto-plastic characteristics. The Tresca and Von Mises yield criteria, which closely approximate metal plasticity behavior, are considered in the current study. After initial yielding, the stress level at which further plastic deformation occurs may be dependent on the current level of plastic strain. Such a phenomenon is termed work hardening or strain hardening. Thus the yield surface will vary at each stage of the plastic deformation, with the subsequent yield surface being dependent on the magnitude of the plastic strains in some way.

Various models which describe strain hardening plasticity in a material are illustrated in Fig. 8-1. A perfectly plastic material is shown in Fig. 8-1(a) where the yield stress level does not depend in any way on the degree of plastic strain. If the subsequent yield surface is a uniform expansion of the original yield surface, without translation as shown in Fig. 8-1(b), the strain hardening model is said to be isotropic. On the other hand if the subsequent yield surface preserves its shape and orientation but translates in the

stress space as a rigid body as shown in Fig. 8-1(c), kinematic strain hardening is said to take place.

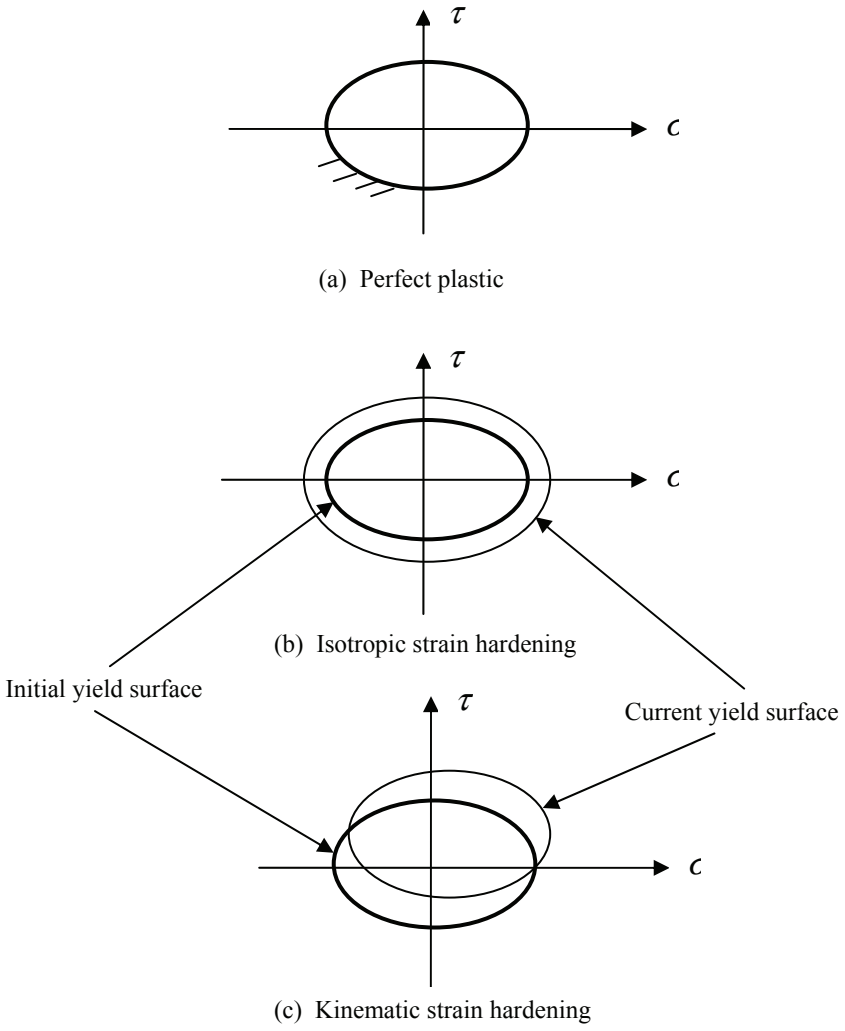

.

Fig. 8-1 Mathematic models for representation of strain hardening behavior

If we ignore the Bauschinger effect due to cyclic loading, isotropic strain hardening material behavior is the simplest way to model strain hardening. Isotropic strain hardening law is expressed as

$$\sigma_{ys}(\bar{\varepsilon}_p) = \sigma_{ys}^{o} + H'\bar{\varepsilon}_p \tag{8-1}$$

where $\bar{\varepsilon}_p = \sqrt{\frac{2}{3} d\boldsymbol{\varepsilon}_{ij}^p d\boldsymbol{\varepsilon}_{ij}^p}$ is the accumulated effective plastic strain. Initial uniaxial yield stress σ_{ys}^o and strain hardening function H' are material properties which can be determined experimentally from a simple uniaxial yield test. The hardening function is defined as [61],

$$H' = \frac{E_T}{1 - \frac{E_T}{E}} \tag{8-2}$$

Where E and E_T are slopes of the stress-strain curve in the elastic and elasto-plastic stage, respectively, as illustrated in Fig. 8-2. Parameter H' is a material property and remains constant for the linear strain hardening material used in this study.

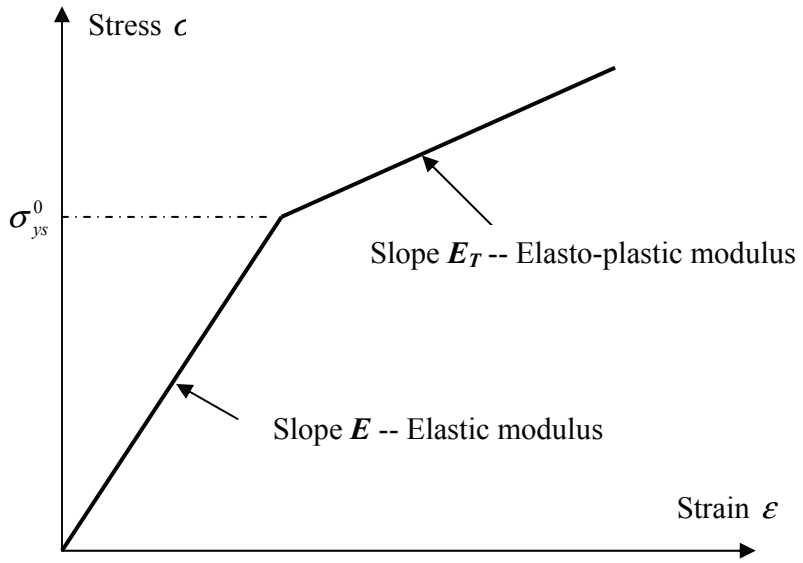

Fig. 8-2 Elasto-plastic linear strain hardening behavior for uniaxial case

When the stress level exceeds yield stress, material yielding will occur and plastic deformation will be generated. The widely used yield criteria are:

(a). The Von Mises yield criterion which can be expressed as

$$\bar{\sigma} = \sqrt{3J_2'} \geq \sigma_{ys} \tag{8-3}$$

Where, $\bar{\sigma}$ is termed the effective stress or equivalent stress, σ_{ys} is the uniaxial tensile yield stress, J_2' is the second deviatoric stress invariant,

$$J_2' = \frac{1}{2}\boldsymbol{\sigma}_{ij}\boldsymbol{\sigma}_{ij} = \frac{1}{6}\left[(\sigma_1-\sigma_2)^2+(\sigma_2-\sigma_3)^2+(\sigma_3-\sigma_1)^2\right] = \frac{1}{2}\left(\sigma_x'^2+\sigma_y'^2+\sigma_z'^2\right)+\tau_{xy}^2 \tag{8-4}$$

Where σ_i ($i = 1,\ 2,\ 3$) are the principal stresses in three orthogonal principal directions.

(b). The Tresca yield criterion has an alternative form,

$$\bar{\sigma} = 2\sqrt{J_2'}\cos\theta \geq \sigma_{ys} \tag{8-5}$$

Where, $\sin 3\theta = -\frac{3\sqrt{3}}{2}\frac{J_3}{(J_2')^{3/2}}$, $-1 \leq \sin 3\theta \leq 1$ and $-\frac{\pi}{2} \leq 3\theta \leq \frac{\pi}{2}$. J_3 is the third stress invariant

$$J_3 = \frac{1}{3}\boldsymbol{\sigma}_{ij}\boldsymbol{\sigma}_{jk}\boldsymbol{\sigma}_{ki} \tag{8-6}$$

8.1.2 Numerical Formulation for Elasto-Plastic Problems

The complete two-dimensional elasto-plastic incremental stress-strain relation can be written as [61],

$$d\boldsymbol{\sigma} = \boldsymbol{D}_{ep}\, d\boldsymbol{\varepsilon} \tag{8-7}$$

Where $\boldsymbol{D}_{ep}$ is the elasto-plastic stiffness matrix

$$\boldsymbol{D}_{ep} = \boldsymbol{D} - \frac{\boldsymbol{d}_D \boldsymbol{d}_D{}^T}{H' + \boldsymbol{d}_D{}^T \boldsymbol{a}}, \qquad \boldsymbol{d}_D = \boldsymbol{D}\boldsymbol{a} \tag{8-8}$$

and $\boldsymbol{D}$ is the elastic stiffness matrix.

In order to calculate the matrix $\boldsymbol{D}_{ep}$, we need to evaluate the flow vector $\boldsymbol{a}$, which can be expressed as,

$$\boldsymbol{a} = C_1 \boldsymbol{a}_1 + C_2 \boldsymbol{a}_2 + C_3 \boldsymbol{a}_3 \tag{8-9}$$

Where,

$$\boldsymbol{a}_1{}^T = \{1, \quad 1, \quad 0, \quad 1\}$$

$$\boldsymbol{a}_2{}^T = \frac{1}{2\sqrt{J_2'}} \{\sigma_x', \quad \sigma_y', \quad 2\tau_{xy}, \quad \sigma_z'\} \tag{8-10}$$

$$\boldsymbol{a}_3{}^T = \left\{\left(\sigma_y'\sigma_z' + \frac{J_2'}{3}\right), \quad \left(\sigma_x'\sigma_z' + \frac{J_2'}{3}\right), \quad -2\sigma_z'\tau_{xy}, \quad \left(\sigma_x'\sigma_y' - \tau_{xy}{}^2 + \frac{J_2'}{3}\right)\right\}$$

And the three scalar constants C_1, C_2, and C_3 are given in Table 8-1 for the Tresca and Von Mises yield criteria.

Table 8-1 Constants defining the yield surface

Yield criterion		C_1	C_2	C_3
Von Mises		0	$\sqrt{3}$	0
Tresca*	$\theta \le 29^\circ$	0	$2\cos\theta(1 + \tan\theta\tan 3\theta)$	$\frac{\sqrt{3}}{J_2'}\frac{\sin\theta}{\cos 3\theta}$
	$\theta > 29^\circ$	0	$\sqrt{3}$	0

*: For Tresca criterion, $\theta = \pm 30^\circ$ results in numerical singularity

Once material stiffness matrix $\boldsymbol{D}_{ep}$ is obtained from Eq. (8-8), elasto-plastic element stiffness matrix $\boldsymbol{K}_T = \int_\Omega \boldsymbol{B}^T \boldsymbol{D}_{ep} \boldsymbol{B} d\Omega$ can be evaluated at each Gauss point.

Under the conditions of plane stress ($\sigma_z = 0$), plane strain ($\varepsilon_z = 0$) or axial symmetry, simplified form of $\boldsymbol{D}_{ep}$ can be derived.

For isotropic plane strain and axisymmetric analysis, elastic stiffness matrix is given by,

$$\boldsymbol{D} = \frac{E(1-\upsilon)}{(1+\upsilon)(1-2\upsilon)} \begin{bmatrix} 1 & \dfrac{\upsilon}{1-\upsilon} & 0 \\ \dfrac{\upsilon}{1-\upsilon} & 1 & 0 \\ 0 & 0 & \dfrac{1-2\upsilon}{2(1-\upsilon)} \end{bmatrix} \tag{8-11}$$

$$\boldsymbol{d}_{\boldsymbol{D}} = \boldsymbol{D}\boldsymbol{a} = \begin{Bmatrix} d_1 \\ d_2 \\ d_3 \\ d_4 \end{Bmatrix} = \begin{Bmatrix} \dfrac{E}{1+\nu} a_1 + M_1 \\ \dfrac{E}{1+\nu} a_2 + M_1 \\ G a_3 \\ \dfrac{E}{1+\nu} a_4 + M_1 \end{Bmatrix}, \qquad M_1 = \frac{E\nu(a_1 + a_2 + a_4)}{(1+\nu)(1-2\nu)} \tag{8-12}$$

Where E , G , and υ are Young's modulus, shear modulus, and Poisson's ratio, respectively. a_i are the components of flow vector $\boldsymbol{a}$.

For plane stress, elastic stiffness matrix is,

$$\boldsymbol{D} = \frac{E}{1-\upsilon^2} \begin{bmatrix} 1 & \upsilon & 0 \\ \upsilon & 1 & 0 \\ 0 & 0 & \dfrac{1-\upsilon}{2} \end{bmatrix} \tag{8-13}$$

$$\boldsymbol{d_D} = \boldsymbol{Da} = \begin{Bmatrix} d_1 \\ d_2 \\ d_3 \\ d_4 \end{Bmatrix} = \begin{Bmatrix} \dfrac{E}{1+\nu} a_1 + M_2 \\ \dfrac{E}{1+\nu} a_2 + M_2 \\ Ga_3 \\ \dfrac{E}{1+\nu} a_4 + M_2 \end{Bmatrix}, \qquad M_2 = \frac{E\nu(a_1 + a_2)}{1 - \nu^2} \tag{8-14}$$

Numerical iteration procedure for elasto-plastic material is described as follow [61]:

1. Solve the simultaneous equations for the r^{th} iteration at a certain load step by Newton-Raphson method and obtain displacement increments $d\boldsymbol{u}^r$ and strain increments $d\boldsymbol{\varepsilon}^r$.

2. Compute stress increments $d\boldsymbol{\sigma}_e^r = \boldsymbol{D} d\boldsymbol{\varepsilon}^r$ (subscript e denotes that fully elastic behavior is assumed initially) as shown in Fig. 8-3.

3. Accumulate the total stress for each Gauss point: $\boldsymbol{\sigma}_e^r = \boldsymbol{\sigma}^{r-1} + d\boldsymbol{\sigma}_e^r$.

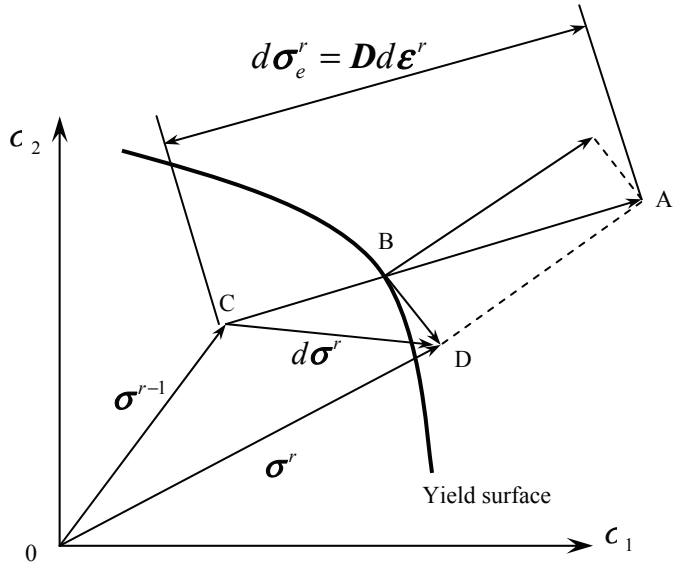

Fig. 8-3 Incremental stress changes at a point in an elasto-plastic continuum

4. Check: $\bar{\sigma}^{r-1} > \sigma_{ys} = \sigma_{ys}^{o} + H'\bar{\varepsilon}_{p}^{\,r-1}$ at each Gauss point. Four possible cases are listed in table bellow:

Previously yielded? Yes		Previously yielded? No	
$\bar{\sigma}_e^r > \bar{\sigma}^{r-1}$?		$\bar{\sigma}_e^r > \sigma_{ys}^o$?	
No (unloading)	Yes (loading)	No	Yes
▪ Gauss point is unloading elastically ▪ Go to step 7	▪ Stress increase ▪ Stress increment must be reduced to the yield surface ▪ Calculate reduction factor $R = \frac{AB}{AC} = 1$ ▪ Go to step 5	▪ Elastic ▪ Go to step 7	▪ Yielding ▪ Extra stress must be reduced to the yield surface ▪ Calculate reduction factor $R = \frac{AB}{AC} = \frac{\bar{\sigma}_e^r - \sigma_{ys}^o}{\bar{\sigma}_e^r - \bar{\sigma}^{r-1}}$ ▪ Go to step 5

5. Update $\boldsymbol{\sigma}^r = \boldsymbol{\sigma}^{r-1} + (1-R)d\boldsymbol{\sigma}_e^r$ (at each yielded Gauss point and satisfy the specified yield criterion)

6. Eliminate the remaining portion of stress $Rd\boldsymbol{\sigma}_e^r$:

a) Determine the number of subincrement m into which the excess stress $Rd\boldsymbol{\sigma}_e^r$ is to be divided, where m is given by the nearest integer of $k\left(\frac{\bar{\sigma}_e^r - \sigma_{ys}}{\sigma_{ys}^o}\right)$, and k is a constant that determines the accuracy of the reduction process. Typically, $5 < k < 10$ can satisfy the requirement of general FEA simulation ($k = 8$ was used in the current study).

b) Iterate over each subincrement m

c) Compute vector $\boldsymbol{a}$ and $\boldsymbol{d_D}$ by Eq. (8-9), Eq. (8-12) or (8-14)

d) Compute $d\lambda = \dfrac{1}{H' + \boldsymbol{a}^T \boldsymbol{D}\boldsymbol{a}} \boldsymbol{a}^T \boldsymbol{d_D} d\varepsilon \geq 0$, where $\boldsymbol{d_D} d\varepsilon = \dfrac{R d\boldsymbol{\sigma}_e^r}{m}$

e) Compute $\boldsymbol{\sigma}^r = \boldsymbol{\sigma}^{r-1} + (1-R) d\boldsymbol{\sigma}_e^r + \dfrac{R d\boldsymbol{\sigma}_e^r}{m} - \dfrac{d\lambda \boldsymbol{d_D}}{m}$

(After the summation process, it will result in $\boldsymbol{\sigma}^r = \boldsymbol{\sigma}^{r-1} + d\boldsymbol{\sigma}_e^r - d\lambda \boldsymbol{d_D}$ to give the stress point that is reduced to the yield surface)

f) Compute effective plastic strain: $\bar{\varepsilon}_p^r = \bar{\varepsilon}_p^{r-1} + \dfrac{d\lambda \boldsymbol{a}^T \boldsymbol{\sigma}^r}{\bar{\sigma}}$

g) End of subincrement iterations over m

h) Compute effective stress $\bar{c}^r$ and current yield stress $\sigma_{ys}^o + H' \bar{\varepsilon}_p^{\ r}$

i) Scale the stress $\boldsymbol{\sigma}^r = \dfrac{\sigma_{ys}^o + H' \bar{\varepsilon}_p^r}{\bar{\sigma}^r} \boldsymbol{\sigma}^r$

7. For elastic Gauss points calculate $\boldsymbol{\sigma}^r$ as $\boldsymbol{\sigma}^r = \boldsymbol{\sigma}^{r-1} + d\boldsymbol{\sigma}_e^r$

In this manner the converged element stresses which satisfy the elasto-plastic stress-strain relation and the yield criterion for the r^{th} load step is obtained.

8.1.3 Geometric Nonlinearity

To allow for geometrically nonlinear elastic and plastic behavior we can use either a Total Lagrangian (TL) or Updated Lagrangian (UL) coordinate system. The UL formulation is based on the same procedures that are used in the TL formulation, but in the solution all static and kinematic variables are referred to the last calculated configuration. Both the TL and UL formulations include all kinematic nonlinear effects

due to large displacement, large rotations, and large strains. The Updated Lagrangian formulation was selected in the current dynamic analysis to model the geometrically nonlinear behaviors as used in Chapter V for simulating peninsula blister test. In addition, Cauchy stress and Almansi strain tensor were used as energy conjugates in present study.

The basic problem in general nonlinear analysis is to find the state of equilibrium of a body corresponding to the applied loads. Assuming that the externally applied loads are described as a function of time (independent of deformation), the equilibrium conditions of a system of finite elements representing the body under consideration can be expressed as

$$\boldsymbol{R}^t - \boldsymbol{F}^t = 0 \tag{8-15}$$

Where $\boldsymbol{R}^t$ is a vector containing externally applied loads and $\boldsymbol{F}^t$ is a vector of the internal nodal forces corresponding to element stress at time t.

The basic approach in an incremental step-by-step solution is to assuming that the solution for the discrete time t is known, and that the solution for the discrete time $t + \Delta t$ is required. Hence, considering Eq. (8-15) at time $t + \Delta t$ we have,

$$\boldsymbol{R}^{t+\Delta t} - \boldsymbol{F}^{t+\Delta t} = 0 \tag{8-16}$$

Since the solution at time t is known, we can write

$$\boldsymbol{F}^{t+\Delta t} = \boldsymbol{F}^t + \boldsymbol{F} \tag{8-17}$$

where $\boldsymbol{F}$ is the incremental in nodal force corresponding to the increment in element displacement and stress from time t to time $t + \Delta t$. This vector can be approximated using a tangent stiffness matrix $\boldsymbol{K}^t$

$$\boldsymbol{F} \cong \boldsymbol{K}^t \boldsymbol{U} \tag{8-18}$$

Where $\boldsymbol{U}$ is a vector of incremental nodal displacements and

$$\boldsymbol{K}^t = \frac{\partial \boldsymbol{F}^t}{\partial \boldsymbol{U}^t} \tag{8-19}$$

Substituting Eq. (8-17) and (8-18) into (8-16), we have,

$$\boldsymbol{K}^t \boldsymbol{U} = \boldsymbol{R}^{t+\Delta t} - \boldsymbol{F}^t \tag{8-20}$$

And solving for $\boldsymbol{U}$, we can get an approximation to the displacement at time $t + \Delta t$

$$\boldsymbol{U}^{t+\Delta t} \cong \boldsymbol{U}^t + \boldsymbol{U} \tag{8-21}$$

We can evaluate the stress and corresponding nodal force according to the approximate displacement solution $\boldsymbol{U}^{t+\Delta t}$ at time $t + \Delta t$. However, because of the assumption in Eq. (8-18), such a solution may be subject to very significant errors. In practice, it is necessary to iterate until the solution of Eq. (8-16) is obtained to sufficient accuracy.

The widely used iteration methods in finite element analysis are based on the classical Newton-Raphson technique (refer to [62] for details). The equations used in the Newton-Raphson iteration are (for iteration step $i = 1,\ 2,\ 3, \cdots\cdots$)

$$\begin{aligned} {}^{(i-1)}\boldsymbol{K}^{t+\Delta t} \Delta^{(i)}\boldsymbol{U} &= \boldsymbol{R}^{t+\Delta t} - {}^{(i-1)}\boldsymbol{F}^{t+\Delta t} \\ {}^{(i)}\boldsymbol{U}^{t+\Delta t} &= {}^{(i-1)}\boldsymbol{U}^{t+\Delta t} + \Delta^{(i)}\boldsymbol{U} \end{aligned} \tag{8-22}$$

with the initial conditions:

$$\begin{aligned} {}^{(0)}\boldsymbol{U}^{t+\Delta t} &= \boldsymbol{U}^t \\ {}^{(0)}\boldsymbol{K}^{t+\Delta t} &= \boldsymbol{K}^t \\ {}^{(0)}\boldsymbol{F}^{t+\Delta t} &= \boldsymbol{F}^t \end{aligned} \tag{8-23}$$

8.1.4 Hilber-Hughes-Taylor (HHT) method for temporal discretization

Now we can derive the incremental formulation of Hilber-Hughes-Taylor (HHT) method (see Chapter VII for details about HHT algorithm) from the classical Newton-Raphson technique. From Eq. (7-10) and (8-22), we have

$$\boldsymbol{M}^{t+\Delta t}\ddot{\boldsymbol{U}}^{t+\Delta t}+(1+\alpha)\boldsymbol{K}^{t+\Delta t}\Delta^{(i)}\boldsymbol{U}=\boldsymbol{R}^{t+\Delta t}-(1+\alpha)^{(i-1)}\boldsymbol{F}^{t+\Delta t}+\alpha\boldsymbol{F}^{t} \tag{8-24}$$

From Eq. (7-12),

$$\ddot{\boldsymbol{U}}^{t+\Delta t}=\frac{1}{\beta\Delta t^{2}}\left(\boldsymbol{U}^{t+\Delta t}-\boldsymbol{U}^{t}\right)-\frac{1}{\beta\Delta t}\dot{\boldsymbol{U}}^{t}-\left(\frac{1}{2\beta}-1\right)\ddot{\boldsymbol{U}}^{t} \tag{8-25}$$

Substituting into Eq. (8-24), we have

$$\hat{\boldsymbol{K}}^{t+\Delta t}\Delta^{(i)}\boldsymbol{U}=\boldsymbol{R}^{t+\Delta t}-(1+\alpha)^{(i-1)}\boldsymbol{F}^{t+\Delta t}+\alpha\boldsymbol{F}^{t}-\boldsymbol{M}^{t+\Delta t}\left[\frac{1}{\beta\Delta t^{2}}\left({}^{(i-1)}\boldsymbol{U}^{t+\Delta t}-\boldsymbol{U}^{t}\right)-\frac{1}{\beta\Delta t}\dot{\boldsymbol{U}}^{t}-\left(\frac{1}{2\beta}-1\right)\ddot{\boldsymbol{U}}^{t}\right] \tag{8-26}$$

Where, $\hat{\boldsymbol{K}}^{t+\Delta t}=(1+\alpha)\boldsymbol{K}^{t+\Delta t}+\frac{1}{\beta\Delta t^{2}}\boldsymbol{M}^{t+\Delta t}$

Eq. (8-26) is the final iteration form of incremental HHT formulation. The right hand side is the residual force term which can be obtained from the equilibrium solution at previous time step t and the latest $(i-1)^{th}$ iteration results of current time step $t+\Delta t$.

8.2 Model Verification

Material and geometric nonlinear models as described in previous section were implemented in a test-bed FEA code NOVA-3D. Model verifications were performed on a single element subjected to uniform extension and simple shear through comparison with predictions by commercial software package ABAQUS version 6.5-1.

8.2.1 Single Element Extension Verification

A single element specimen under uniform extension is illustrated in Fig. 8-4 and plane strain conditions are applied. To verify the capability of NOVA for simulating nonlinear material behavior, a linear strain hardening function was assumed in this study as shown in Fig. 8-2, material properties are: $E = 200GPa$, $E_T = 40GPa$, $\sigma_{ys}^{o} = 400MPa$, $H' = \dfrac{E_T}{1 - \dfrac{E_T}{E}} = 50GPa = constant.$ The loading process used in the simulation consists of three steps: loading to material yield, unloading to zero, and then reloading to material yield again.

8-node quadratic element with 3×3 Gauss integration was used in both NOVA and ABAQUS for accurate comparison. Predicted responses from NOVA-3D were compared with that from commercial software package ABAQUS, and excellent agreement was observed (Fig. 8-5). In Fig. 8-5, some residual Von Mises stresses were observed in both ABAQUS and NOVA-3D due to the constrained extension (plane strain) after the external load was reduced to zero (unloading).

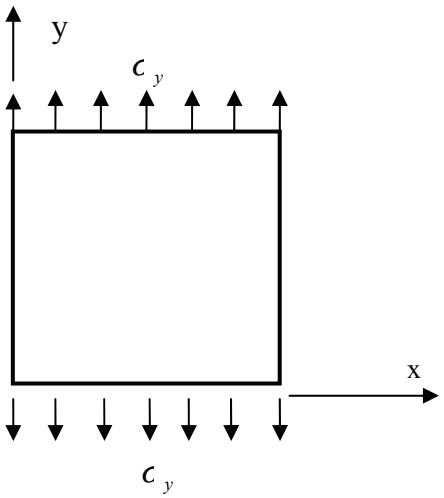

Fig. 8-4 Single element extension (plane strain conditions)

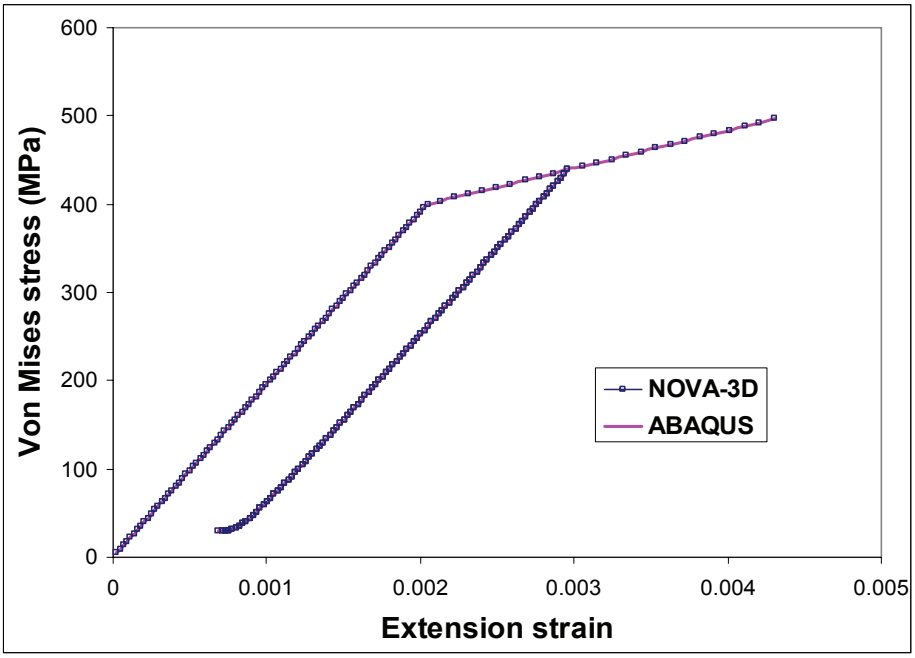

Fig. 8-5 Stress-strain relation comparison between NOVA and ABAQUS

8.2.2 Simple Shear Verification

A single element specimen considering material and geometric nonlinearity was simulated under simple shear conditions (Fig. 8-6). Displacement controlled loading was employed to ensure the stability of the loading process. Material properties were assumed to be the same as in single element extension. Very large shear deformation, up to 300%, was applied to test the capability and robustness of the algorithm described in section 8.1. Simulation results showed that the algorithm used in the study is rather robust to cope with large deformation and nonlinear material behavior as depicted in Fig. 8-7. Good agreement was observed between NOVA-3D and ABAQUS results when the shear strain

is less than 100%. Discrepancy at high strain level is possibly due to the distortion of the single element used in this case.

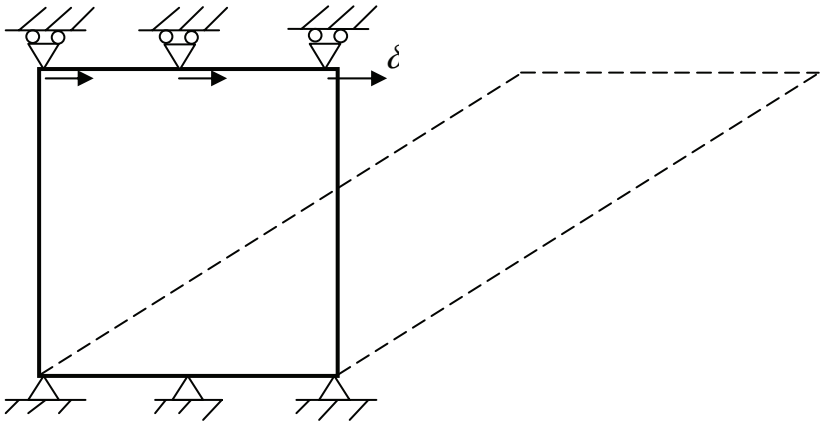

Fig. 8-6 Single element under simple shear (displacement control)

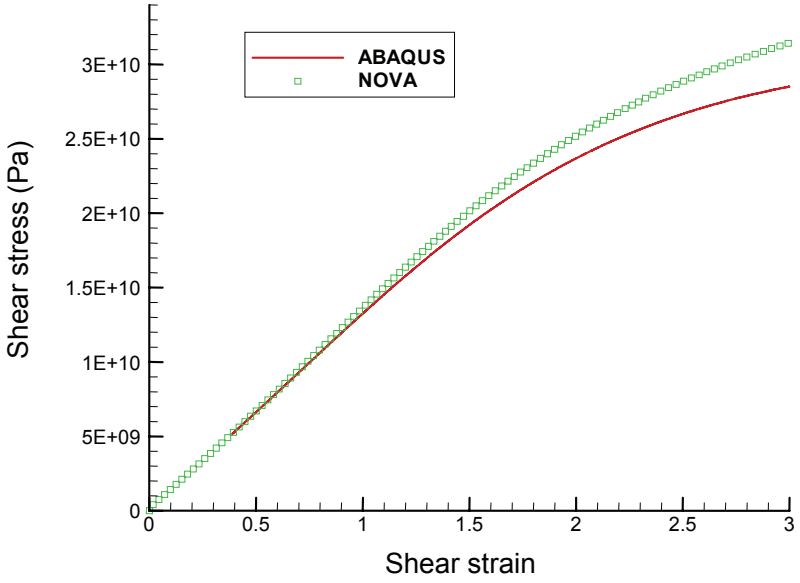

Fig. 8-7 Single element shear stress vs. shear strain for simple shear

To avoid extensive distortion in the single element specimen, a refined FEA mesh (19×19) was used in the simple shear simulation, and better agreement was obtained, as

shown in Fig. 8-8. Global shear stress (or applied shear force), local shear stress and equivalent plastic strain at the center of the specimen are shown in Fig. 8-8, 8-9, and 8-10. It can be concluded that the predictions from NOVA-3D match very well with that from ABAQUS especially when the global shear strain is less than 100%. The deformed shape of the specimen with 200% shear deformation is shown in Fig. 8-11.

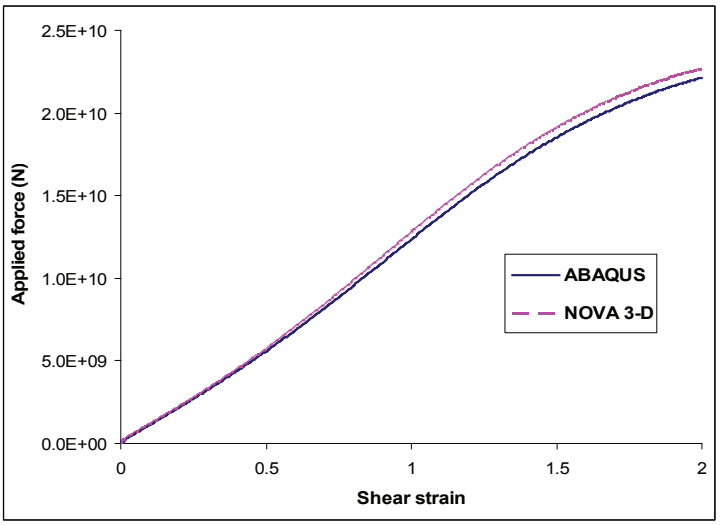

Fig. 8-8 Applied shear force vs. shear strain (global comparison, 19×19 mesh)

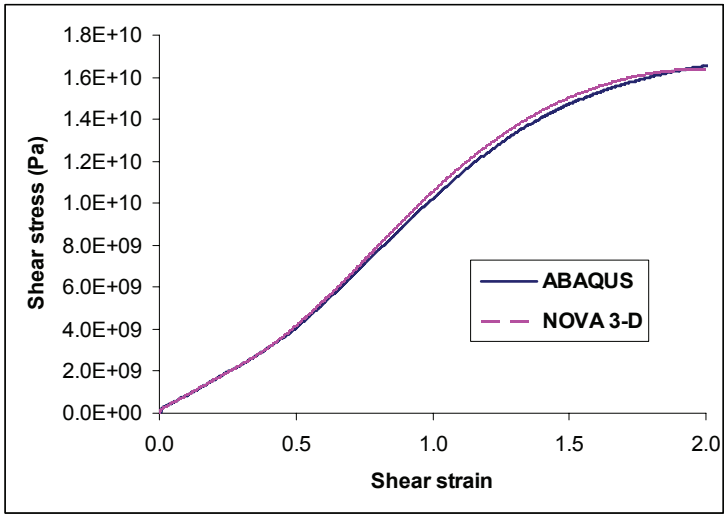

Fig. 8-9 Shear stress at the center of the specimen (local comparison, 19×19 mesh)

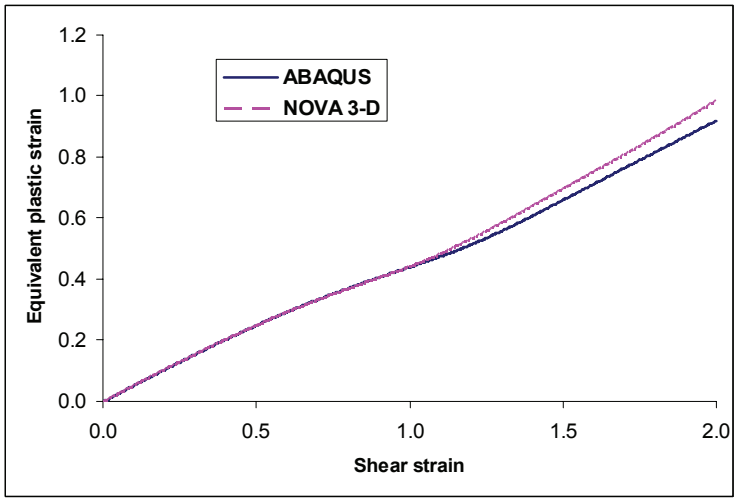

Fig. 8-10 Equivalent plastic strain at the center of the specimen (19×19 mesh)

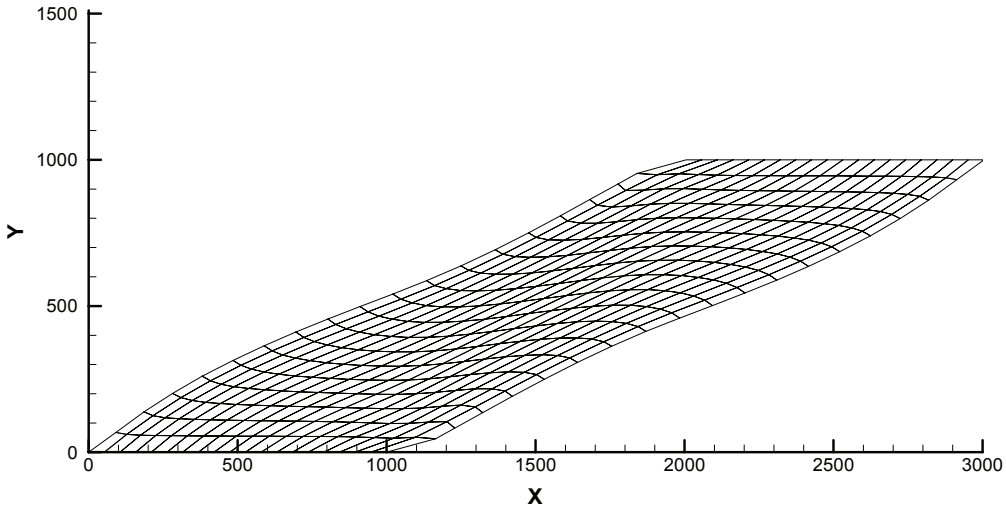

Fig. 8-11 Deformation of a simple shear specimen with 200% shear strain (19×19 mesh)

8.3 Dynamic Response of a Circular Steel Plate with Coating under Blast Load

8.3.1 Modeling of a Clamped Circular Steel Plate with Coating

In the current simulation, blast loading of a clamped circular steel plate with polymer coating on both sides was considered. The axisymmetric two-dimensional model is shown in Fig. 8-12. Because of the intense pressure of the instantaneous blast load, both steel plate and polymeric coating are considered as linear strain hardening elasto-plastic materials, and the material properties are listed in Table 8-2. Uniformly distributed pressure was applied at the center of the plate with a diameter of 50*mm* to simulate blast loading, which corresponding to a circular-shaped explosive directly placed above the center of the plate. A peak pressure $P_r = 70MPa$ with exponential time history, duration time $t_d = 1\ ms$, and shape factor $b = 1$ were assumed in the simulation (see Chapter VII and Fig. 7-2 for details of the blast load).

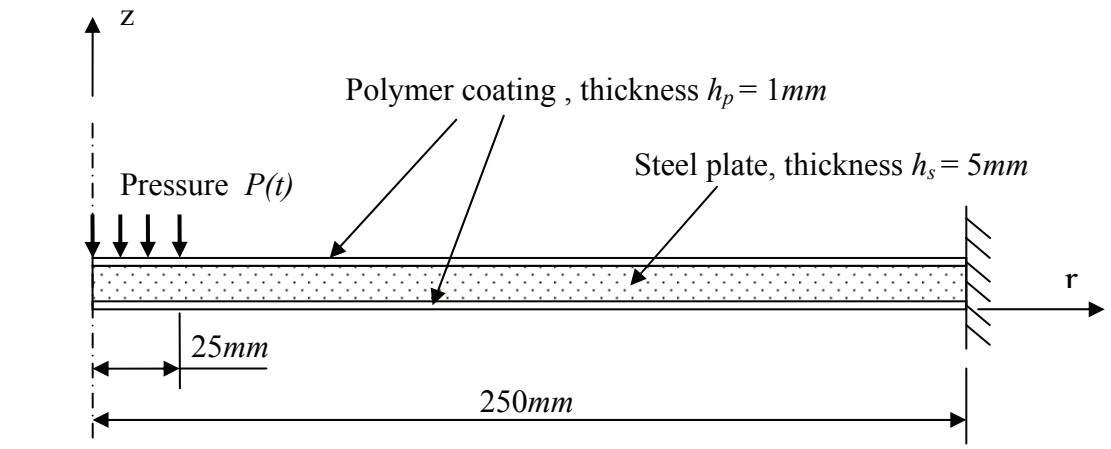

Fig. 8-12 Axisymmetric model of a circular steel plate with coating

An FEA mesh (as shown in Fig. 8-13) with 408 (51×8) eight-node quadratic element (one element for each coating layer and 6 elements for steel plate in the vertical direction to capture the large deformation of the plate) was used in the simulation performed by FEA code NOVA-3D. To capture the contribution of high frequency vibration modes and to adapt to the high strain-rate in the plate, a very small time step $\Delta t = 0.2\mu s$ was employed at the beginning of the simulation. Subsequently, step size was gradually increased to save computation time.

Table 8-2 Material properties of steel plate and polymer coating

Material	$E\ (GPa)$	$E_T\ (GPa)$	υ	$H'\ (GPa)$	$\sigma_{ys}^0\ (MPa)$	$\rho\ (Kg/m^3)$
Steel	200	2.5	0.28	2.532	400	7800
Coating*	8	4	0.40	8	30	1200

*: Coating material is glass fiber reinforced polyurethane.

Fig. 8-13 FEA mesh for simulating steel plate with coating (dimensions not scaled)

8.3.2 Numerical Damping of HHT Method

In HHT method (Eq. 8-26), constant α ($-\frac{1}{3}\le\alpha\le0$) is a parameter that can continuously control the numerical damping of the structure; with $\alpha=0$ this algorithm is reduced to Newmark method which is non-dissipative. Numerical damping of HHT

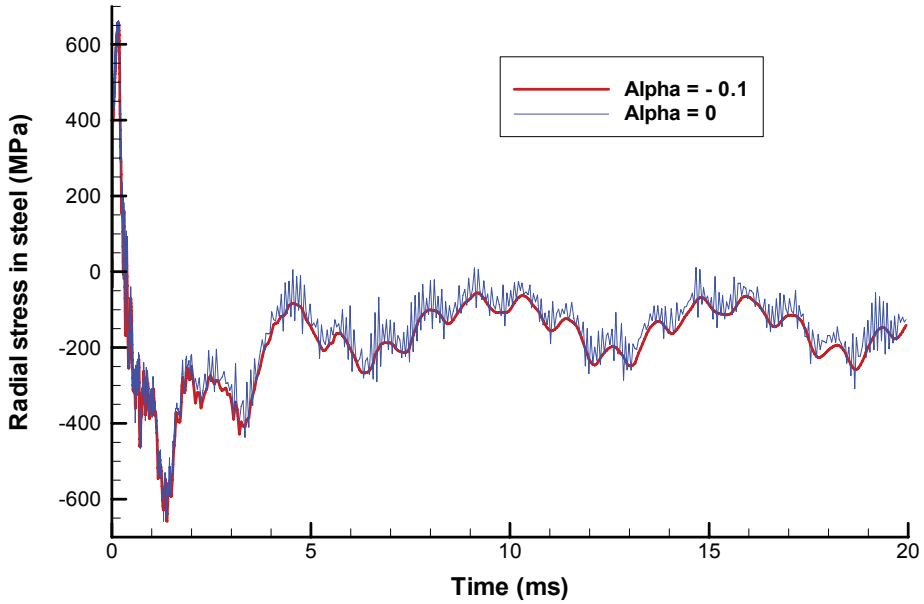

(a) Radial stress history in steel, with and without numerical damping

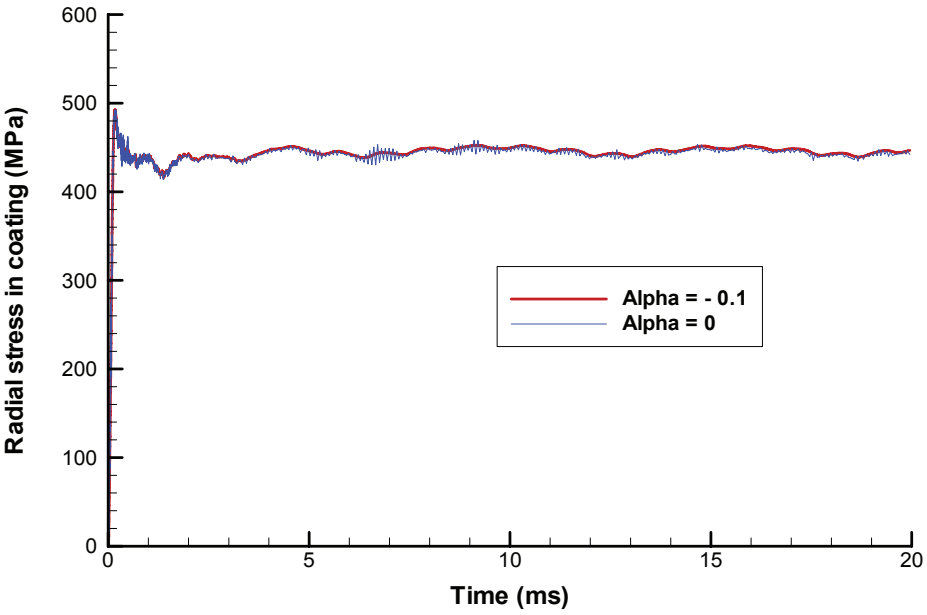

(b) Radial stress history in coating, with and without numerical damping

Fig. 8-14 Numerical damping of HHT method on high-frequency modes

method on high-frequency modes was found to be effective in the current simulation of the dynamic responses. High frequency components in the stress responses were damped out when the numerical damping $\alpha = -0.1$ was introduced in the dynamic simulation. Smoother curves of stress history in both steel plate and coating were obtained as shown in Fig. 8-14.

It was also observed that the influence of parameter α on plate deflection (Fig. 8-15) is insignificant. The reason is that the stress is the first derivative of displacement and therefore is more sensitive to the numerical noise due to the high frequency vibration modes.

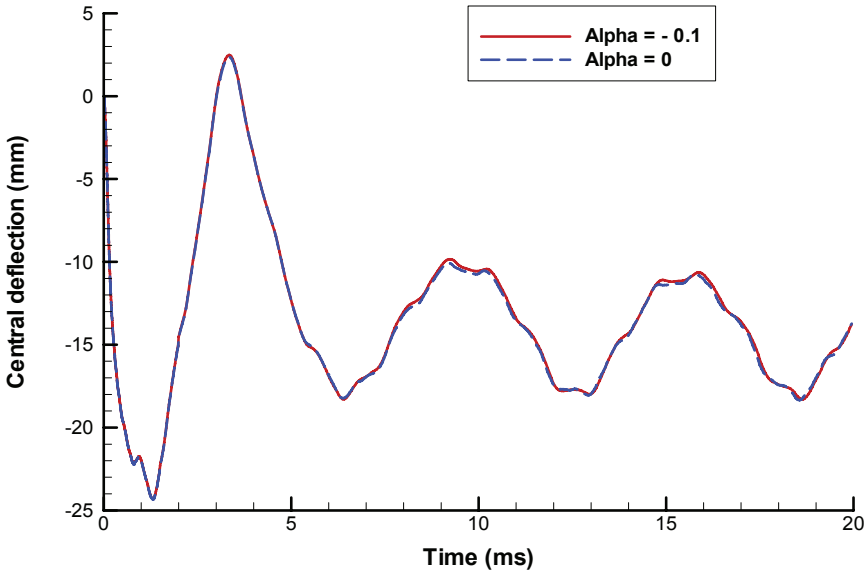

Fig. 8-15 Numerical damping of HHT method on plate deflection

8.3.3 Dynamic Responses under Different Load Levels

Dynamic response is very complex when material and geometric nonlinearity are involved in the structure. Large displacement and large deformation may change the system mass matrix and the nonlinear material properties will result in a continuous change in system stiffness matrix as plastic straining occurs and develops in the structure. Therefore different vibration profiles of the plate with different frequency spectrum will be observed under different load levels as illustrated in Fig. 8-16.

When peak pressure $P_r \leq 10MPa$, the plate is in an elastic state without any plastic deformation occurring in the steel plate and polymeric coating. The plate vibrates around the equilibrium position which is the original position before the load was applied. As peak pressure is increased, plastic deformation occurs in the steel plate first, and then, in the polymeric coating. Maximum equivalent plastic strains in the steel plate and polymeric coating at the center of the plate increase with the applied peak load as shown in Fig. 8-17. The variation in minimum and maximum deflections with the applied peak pressure is shown in Fig. 8-18. As plastic deformation progresses, plate becomes stiffer and stiffer due to the strain hardening effect of both the steel plate and polymeric coating and therefore results in the increase of fundamental frequency of the plate structure as clearly revealed in Fig. 8-16.

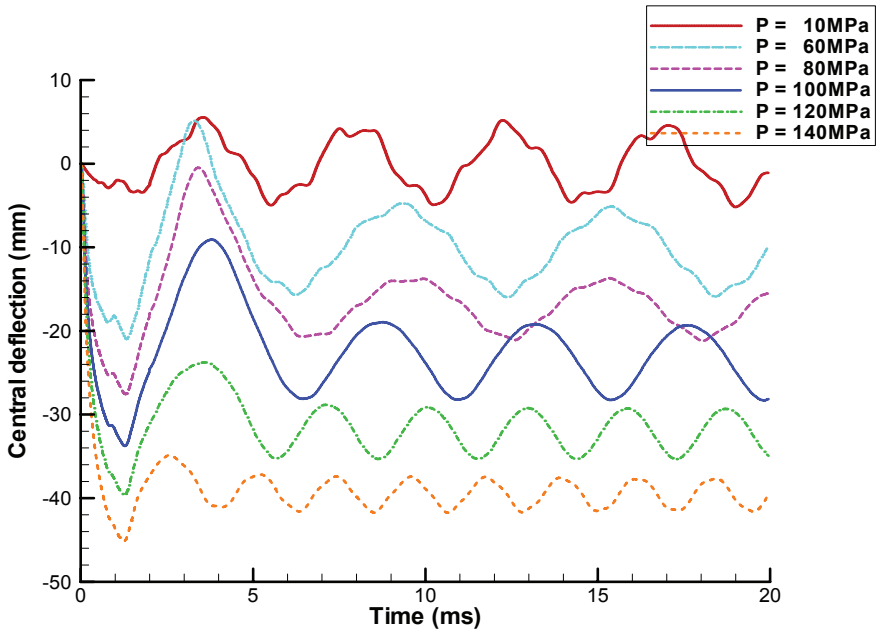

Fig. 8-16 Central deflection history under various peak pressure levels

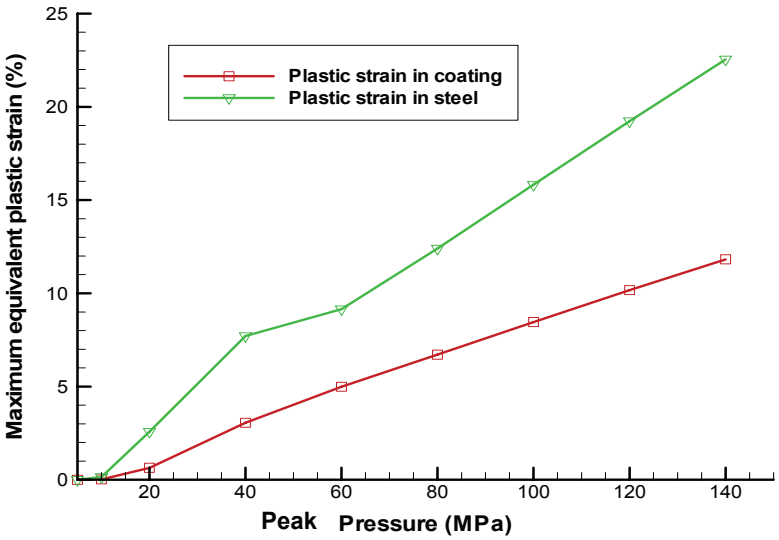

Fig. 8-17 Maximum equivalent plastic strain at plate center under various peak pressure levels

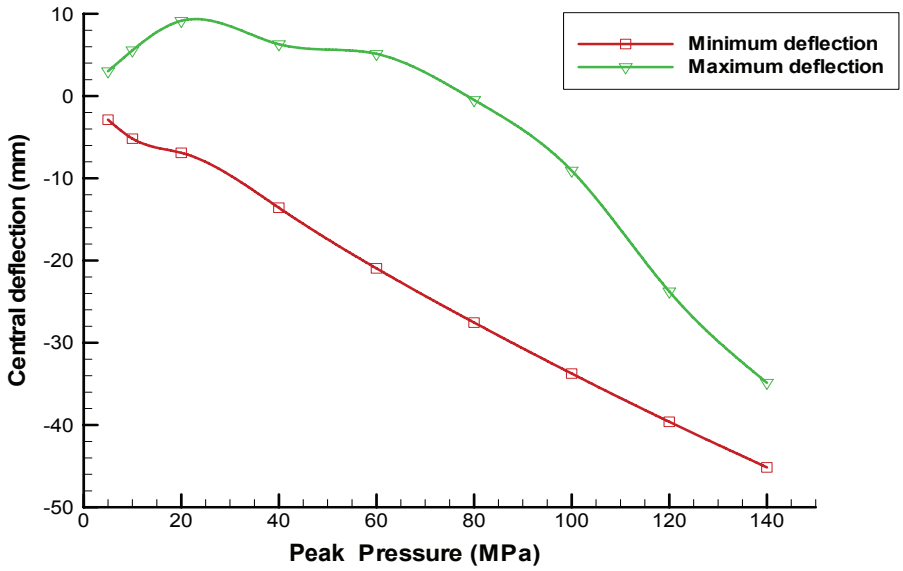

Fig. 8-18 Minimum and maximum deflections under various peak pressure levels

8.3.4 Effects of Coating on Plate Responses

To study the effect of the polymeric coating on the dynamic response of the steel plate, steel plate with elastic coating, elasto-plastic coating and without any coating were simulated under blast loading for comparison. Significant changes of central deflection of the plate (Fig. 8-19), radial stress in the polymer coating at the plate center (Fig. 8-20), and equivalent plastic strain at the center, bottom surface of the steel plate (Fig. 8-21) were observed from FEA simulation. Maximum equivalent plastic strains at the bottom surface of the steel plate plotted along the radial direction are shown in Fig. 8-22. Highest plastic strain occurred in the steel plate without any coating, while about 20% reduction of plastic strain in the steel plate was observed at the center of the plate after 1*mm* thick elasto-plastic coatings were applied on both sides of the steel plate. Compared with elasto-plastic coating, elastic coating can sustain higher stress (Fig. 8-20) and provide

stronger constraining effect on the steel plate, and therefore, allow lower plastic strain to occur in the steel plate. But it is usually not realistic for polymer material to stay in elastic state under large deformation. Elasto-plastic material behavior of the polymer coating is a practical approach to simulate the effect of polymer coating on steel plate.

It was also observed from Fig. 8-20 and 8-21 that the maximum stress and plastic straining usually occur at the very beginning of the blast loading process, i.e. $t < \frac{1}{2} t_d = 0.5ms$. After that period, no further plastic deformation occurs and the plate vibration will gradually decay due to energy dissipation. Equivalent plastic strain (PEEQ) distribution in steel plate and polymer coating as well as their permanent deformation is shown in Fig. 8-23.

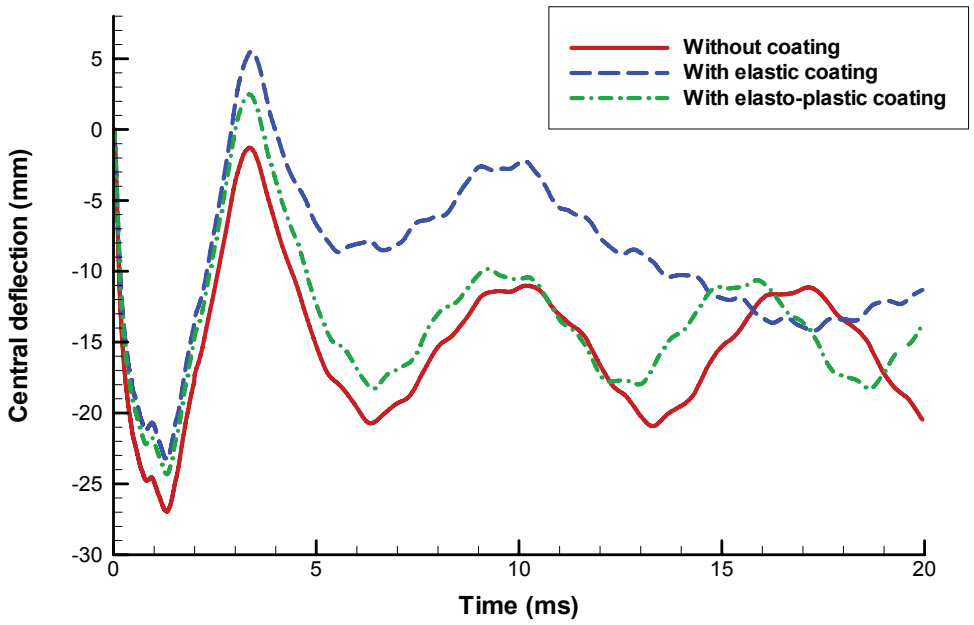

Fig. 8-19 Central deflection history of the plate

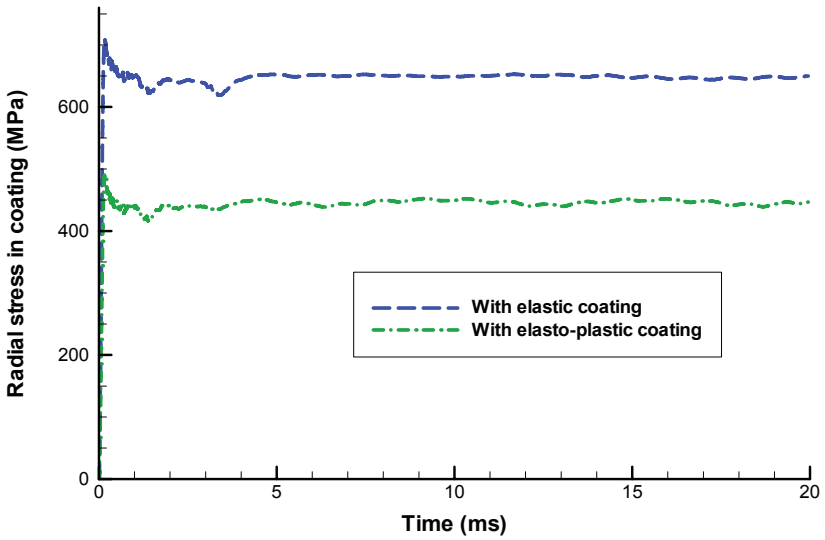

Fig. 8-20 Radial stress history in polymer coating

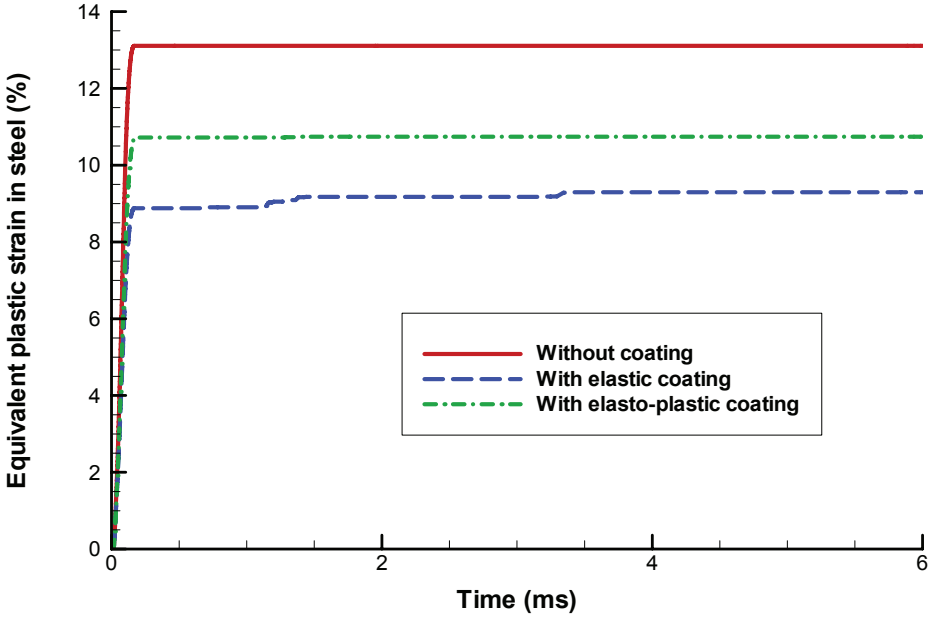

Fig. 8-21 History of equivalent plastic strain in steel plate

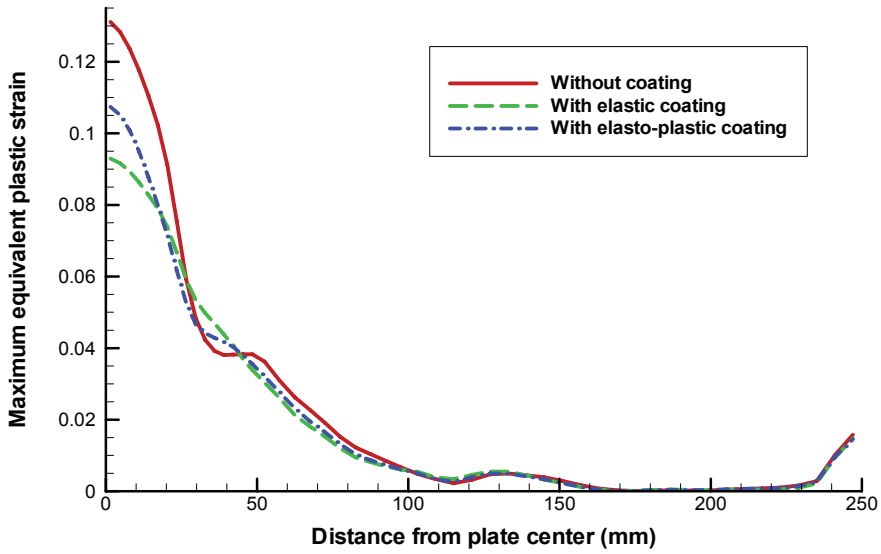

Fig. 8-22 Maximum equivalent plastic strain at the bottom surface of steel plate (Strain values are 0.131, 0.107, and 0.0929 for the three cases at the plate center)

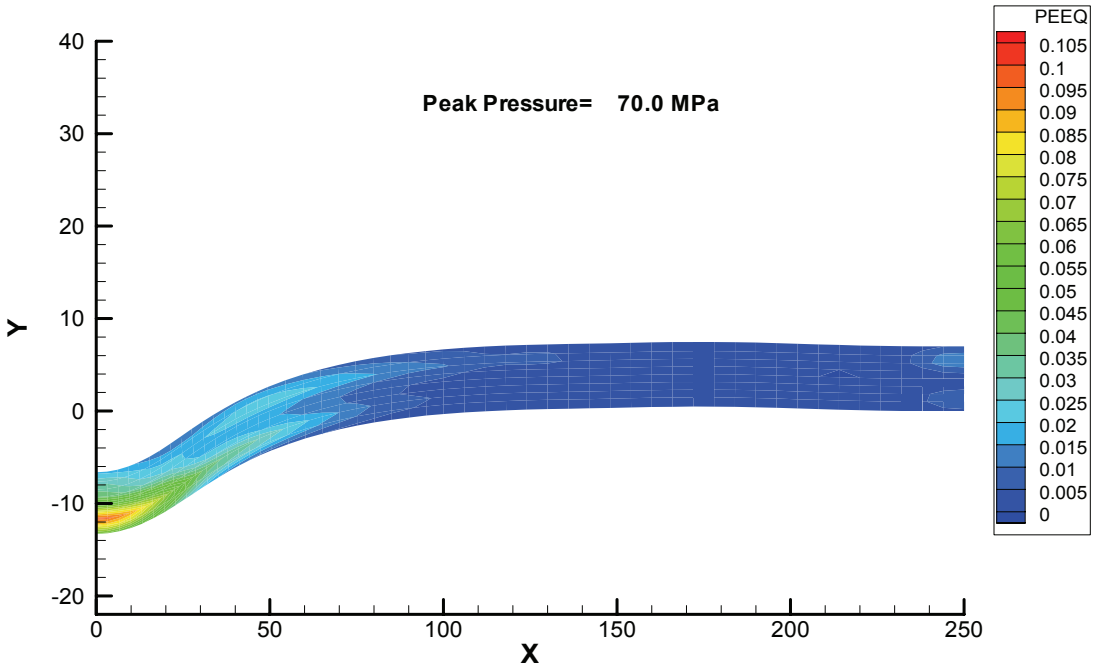

Fig. 8-23 Equivalent plastic strain in steel plate and permanent deformation (not scaled)

8.3.5 Time-Dependent Effect of Polymeric Coating

Polymeric materials usually display some time-dependent behavior due to molecular motion. To investigate the time-dependent effect of the coating material on the plate responses, a viscoelastic coating material with Prony series as listed in Table 5-3 was considered in the simulation. For comparison, a corresponding elastic coating was constructed as follow: its material properties are identical to the instantaneous values of the viscoelastic tensile relaxation modulus, $E(t)$, and Poisson's ratio, $\upsilon(t)$, at the time $t = 0$, i.e.

$$E_0 = E(t)\big|_{t=0} = 3.372GPa$$

$$\upsilon_0 = \upsilon(t)\big|_{t=0} = 0.391$$

Very small differences in plate deflection (Fig. 8-24) and stress in steel plate (Fig. 8-25) at the center of the plate were observed between elastic and viscoelastic coatings due to the very short time period of the blast loading. An interesting phenomenon is that a significant stress relaxation in viscoelastic coating was observed in NOVA-3D predictions as shown in Fig. 8-26. Similar results were also observed from ABAQUS FEA predictions. This might be due to the existence of high frequency oscillation in the viscoelastic coating, which dissipated part of the strain energy that was stored in the viscoelastic coating, thereby causing stresses to relax.

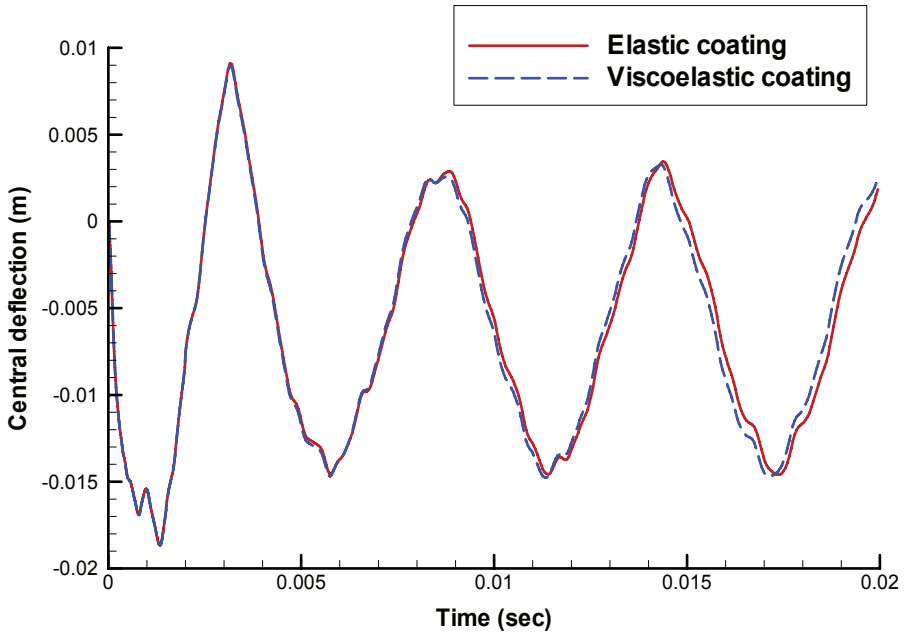

Fig. 8-24 Central deflection history of the plate

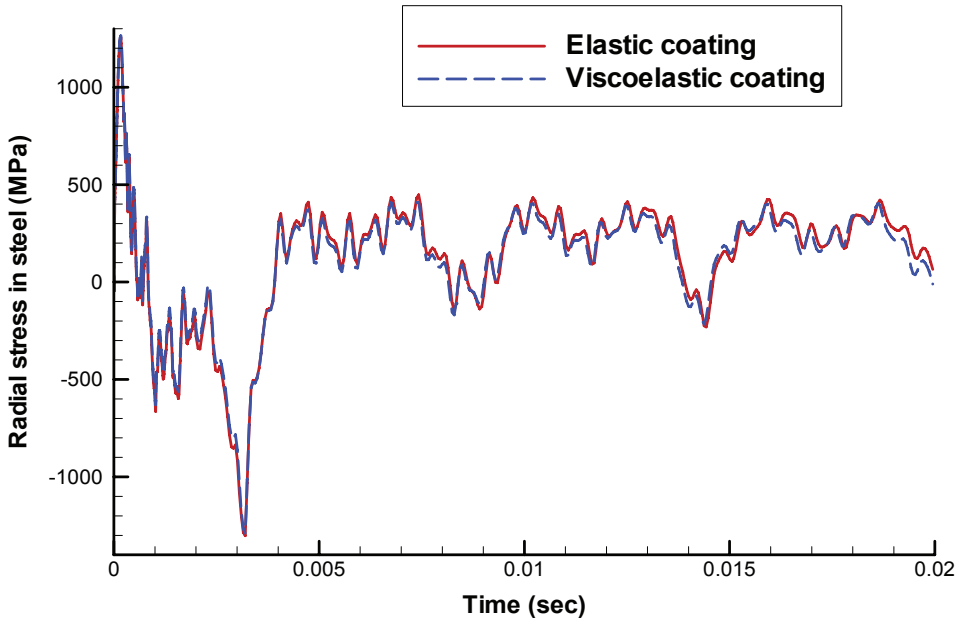

Fig. 8-25 Radial stress history in steel plate at the plate center

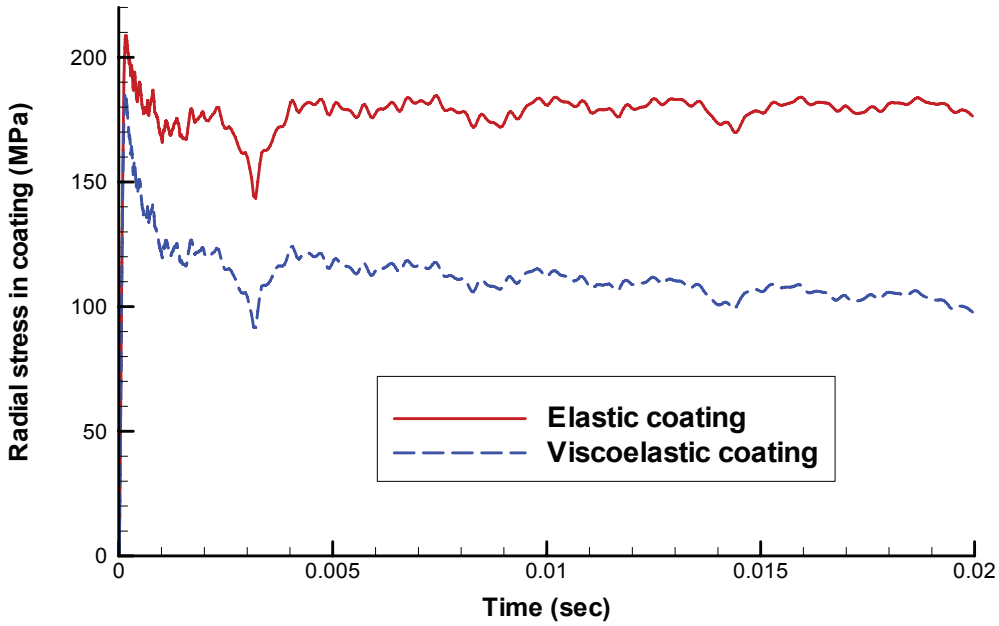

Fig. 8-26 Radial stress history in polymer coating at the plate center

8.4 Conclusions

Material and geometric nonlinearity consideration are often essential when evaluating the structural dynamic responses under blast loading. The Updated Lagrangian (UL) formulation was chosen to handle the large displacement, large rotations, and large deformations in the current study. Isotropic linear strain hardening law combined with Tresca and Von Mises yield criteria was used to capture the material nonlinearity. Material and geometric nonlinear models were implemented into a test-bed FEA code NOVA-3D. Code verification under very large deformation showed that the nonlinear model used in current study is accurate and robust. HHT algorithm involving nonlinear kinematics and material behavior was implemented and used to predict the dynamic responses of a steel plate with polymeric coating under blast load. It was observed that

polymer coating applied on the steel plate would significantly decrease the plastic strain in the steel plate (~20%). The effects of the factors such as the numerical damping, time-dependent behavior of polymeric coating, and different external pressure levels were found to be important to the dynamic responses under blast load.

CHAPTER IX

CONCLUSIONS

To simulate the debond initiation and propagation in the adhesive layer of FRP bonded concrete structures, two-dimensional and three-dimensional cohesive layer constitutive models with prescribed traction-separation laws were constructed from fundamental principles of continuum mechanics and thermodynamics, taking into account non-Fickian hygrothermal effects that are likely to occur within a cohesive layer. Based on debond tip deformation or strain energy release rate, failure criteria for mixed mode I and mode II debond (and even mode III) were developed to predict the debond of FRP.

The cohesive layer model was implemented into a test-bed finite element code NOVA-3D and code verification was performed on a double cantilever beam (DCB). Benchmark comparisons of finite element predictions of global load and local stress field with the analytical solutions for a DCB specimen resulted in a good agreement after modifications were made to the original Williams' solution. Simulations were also successfully performed on blister test and wedge test, which demonstrates the ability of the cohesive layer model to simulate adhesive debond and debond growth in different structures and under different loading conditions.

From the study of the DCB specimen, it can be concluded that both local and global cohesive layer parameters are fairly sensitive to the cohesive layer thickness,

whereas the correction factor (k) to Williams' original solution significantly influences the local stress distribution and damage length.

Numerical simulation of a wedge-test involving debond growth caused by synergistic interactions between local stress and diffusing moisture was performed to demonstrate the ability of the cohesive-layer model to simulate environmental cracking.

A finite element code based on cohesive layer model was developed to simulate the complex process of the peninsula blister test. Convergence and stable debond growth were obtained over a fairly large debond length, FEA simulation results are in good agreement with both analytical solution and test data. Geometry of peninsula blister specimen was studied by both analytical and FEA approaches and recommendations were made toward the design of peninsula blister specimens. FEA simulation results also showed that large deflections, time-dependent material behavior, and residual stresses in the thin film are important factors that should be considered in simulations of the peninsula blister test in order to extract the interfacial fracture toughness of a given adhesive system.

From the simulation results of wedge test it can be concluded that stress-strain relation of cohesive layer is rate-dependent. The cohesive layer thickness is an important characteristic parameter of the cohesive layer model, and it is quite sensitive to the fracture toughness and the stress-strain relation of cohesive material. Simulation of wedge tests under different wedge speeds was also presented to demonstrate the rate-dependent behavior of cohesive layer model and the ability of the cohesive layer model to simulate transient as well as steady-state debond growth at various strain rates.

Implicit HHT method with numerical damping was used in current study to study the dynamic response of FRP plated concrete structure under blast load. Long term responses and short term responses were obtained and their contributions to the debond of FRP from concrete were found to be significantly different. Introduction of a crack in the concrete would induce stress concentration near the crack tip and therefore result in debond initiation in the vicinity of the crack.

Material and geometric nonlinear consideration are often essential when evaluating dynamic response of structures under blast loading. Code verification under very large deformation showed that the nonlinear model used in current study is accurate and robust. HHT algorithm involving nonlinear kinematics and material behavior was implemented and used to predict the dynamic responses of a steel plate with polymer coating under blast loads. It was found that polymer coating applied on steel plate would decrease the plastic strain in the steel plate (~20%). The effects of the factors such as the numerical damping, time-dependent behavior of polymeric coating, and different external pressure levels were found to be important to the dynamic responses under blast load.

BIBLIOGRAPHY

1. Hag-Elsafi, O., Alampalli, S., and Kunin, J. (2000), "Application of FRP Laminates for Strengthening of a Reinforced-Concrete T-Beam Bridge Structure", *Composite Structures*, 52, pp. 453-466.
2. Ritchie, P. A., Thomas, D. A., Lu, L. W., and Connely, G. M. (1991), "External Reinforcement of Concrete Beams using Fiber Reinforced Plastics", *ACI Structure Journal*, 88(4), pp. 490-500.
3. Miller, T. C., Chajes, M. J., Mertz, D. R., and Hastings J. N. (2001), "Strengthening of a Steel Bridge Girder using CFRP Plates", *Journal of Bridge Engineering-ASCE*, 6(6), pp. 524-522.
4. Barenblatt, G. I. (1962), "The Mathematical Theory of Equilibrium of Cracks in Brittle Fracture", *Advances in Applied Mechanics*, 7, pp.55-129.
5. Dugdale, D. S. (1960), "Yielding of Steel Sheets Containing Slits", *Journal of Mechanics and Physics of Solids*, 8, pp.100-108.
6. Hillerborg, A, Modeer, M, and Petersson, P. E. (1976), "Analysis of Crack Formation and Crack Growth in Concrete by Means of Fracture Mechanics and Finite Elements", *Cement Concrete Research*, 6, pp.773-782.
7. Needleman, A. (1987), "A Continuum Model for Void Nucleation by Inclusion Debonding," *Journal of Applied Mechanics*, 54, pp. 525-531.

8. Needleman, A. (1990), "An Analysis of Decohesion Along an Imperfect Interface," *Journal of the Mechanics and Physics of Solids*, 38(3), pp. 289-324.
9. Tvergaard, V., and Hutchinson, J. W. (1993), "The Influence of Plasticity on Mixed Mode Interface Toughness," *Journal of the Mechanics and Physics of Solids*, 41, pp. 1119-1135.
10. Tvergaard, V., and Hutchinson, J. W. (1994), "Effect of T-stress on Mode I Crack Growth Resistance in a Ductile Solid," *International Journal of Solids and Structures*, 31, 823-833.
11. De Borst, R. (2003), "Numerical Aspects of Cohesive-Zone Models," *Engineering Fracture Mechanics*, 70, pp. 1743-1757.
12. Song, S. J., Wass, A. M. (1995), "Energy-Based Mechanical Model for Mixed Mode Failure of Laminated Composites," *AIAA*, 33(4), pp. 739-745.
13. Shawan, K., Waas, A. M. (1997), Non-self-similar decohesion along a finite interface of unilaterally constrained delaminations. *Proc R Soc London*, 453, pp. 515-550.
14. El-Sayed, S., and Sridharan, S. (2001), "Predicting and Tracking Interlaminar Crack Growth in Composites Using a Cohesive Layer Model," *Composites Part B: Engineering*, v. 32, n 6, pp. 545-553.
15. Knauss, W. G. and Losi, G. U. (1993), "Crack Propagation in a Nonlinearly Viscoelastic Solid with Relevance to Adhesive Bond Failure," *Journal of Applied Mechanics*, Vol. 60, pp. 793-801.
16. Ma, Q., Tran, Q., Pan, C., Fujimoto, H., and Chiang, C. (1998), "Polymer/Metal Interfaces in Interconnect Structures: Moisture Diffusion and Stress Corrosion

Effects," *Proceeding of the Material Research Society Symposium*, Vol. 511, pp. 329-339.

17. Roy, S., Lefebvre, D. R., Dillard, D. A. and Reddy, J. N. (1989), "A Model for the Diffusion of Moisture in Adhesive Joints. Part III: Numerical Simulations," *Journal of Adhesion*, Vol. 27, pp. 41-62.
18. Roy, S. (1999), "Modeling of Anomalous Diffusion in Polymer Composites: A Finite Element Approach," *Journal of Composite Materials*, Vol. 33, No. 14, pp. 1318-1343.
19. Roy, S., Xu, W., Park, S. J., and Liechti, K. M. (2000), "Anomalous Moisture Diffusion in Viscoelastic Polymers: Modeling and Testing", *Journal of Applied Mechanics*, Vol. 67, June, pp. 391-396.
20. Roy, S., Xu, W., Patel, S., and Case, S. (2001), "Modeling of Moisture Diffusion in the Presence of Bi-axial Damage in Polymer Matrix Composite Laminates," *International Journal of Solids and Structures*, Vol. 38, issue 42-43, pp. 7627 – 7641.
21. Shirani, A., and Liechti, K. M. (1998), "A Calibrated Fracture Process Zone Model for Thin Film Blistering," *International Journal of Fracture*, 93, pp. 281-314.
22. Kutlu, Z, and Chang, F. K. (1995), "Composites Panels Containing Multiple Through-the-Width Delaminations and Subjected to Compression. Part II: Experiments and Verification," *Composite Structures*, 31(4), pp. 297-315.
23. Williams, J. G., and Hadavinia, H. (2002), "Analytical Solutions for Cohesive Zone Models," *Journal of the Mechanics and Physics of Solids*, 50, pp. 809-825.

24. Gurtin, M. E., Yatomi, C. (1979), "On a Model for Two Phase Diffusion in Composite Materials", *Journal of Composite materials*, 13, pp.126-130.

25. Carter, H. G., Kibler, K. G. (1978), "Langmuir-Type Model for Anomalous Diffusion in Composite Resins", *Journal of Composite Materials*, 12, pp.118-130.

26. Shirrell, C. D., Lersler, W. H., and Sandow, F. A. (1979), "Moisture-Induced Surface damage in T300/5208 Graphite/epoxy Laminates", In: Pipes, R. B. (Ed.), *Nondestructive Evaluation and Flaw Criticality for Composite Materials*, ASTM STP 696, American Society for Testing and Materials, pp.53-78.

27. Weitsman, Y. (1991). "Moisture in Composites: Sorption and Damage," in *Fatigue of Composite Materials*, K. L. Reifsnider, ed., Elsevier Science Publishers B.V., pp. 385-429.

28. Weitsman, Y. 1987. "Coupled Damage and Moisture Transport in Fiber-Reinforced, Polymeric Composites," *International Journal of Solids and Structures*, 23(7): pp. 1003-1025.

29. Gao, H., and Ji, B. (2003), "Modeling Fracture in Nanomaterials via a Virtual Internal Bond Method," *Engineering Fracture Mechanics*, 70, pp. 1777-1791.

30. Spies, G. J. (1953), "The Peeling Test on Redux-Bonded Joints", *Journal of Aircraft Engineering*, 25, pp. 64-70.

31. Kim, K-S., and Kim, J. (1988), "Elasto-plastic Analysis of the Peel Test for Thin Film Adhesion", *Journal of Engineering Materials and Technology*, 110, pp. 266-273.

32. Kinloch, A. J., Lau, C. C., and Williams, J. G. (1994), "The Peeling of Flexible Laminates", *International Journal of Fracture*, 66, pp. 45-70.

33. Wei, Y. and Hutchinson, J. W. (1997), "Steady-State Crack Growth and work of Fracture for Solids Characterized by Strain Gradient Plasticity", *Journal of the Mechanics and Physics of Solids*, 45, pp. 1253-1273.

34. Williams, M. L. (1970), "The Fracture Threshold for an Adhesive Interlayer", *Journal of Applied Polymer Science*, 14, pp. 1121-1126.

35. Dannenberg, H. (1961), "Measurement of Adhesion by Blister Method", *Journal of Applied Polymer Science*, 13, pp. 29-40.

36. Allen, M. G., and Senturia, S. D. (1989), "Application of the Island Blister Test for Thin Film Adhesion Measurement", *Journal of Adhesion*, 29, pp. 219-231.

37. Napolitano, M. J., Chudnosky, A., and Moet, A. (1988), "The Constrained Blister Test for the Energy of Interfacial Adhesion", *Journal of Adhesion Science and Technology*, 27, pp. 311-323.

38. Chang, Y-S, Lai, Y-H, and Dillard, A. (1989), "The Constrained Blister – A Nearly Constant Strain Energy Rate Test for Adhesion", *Journal of Adhesion*, 27, pp. 197-211.

39. Dillard, D. A., and Bao, Y. (1991), "The Peninsula Blister Test: A high and Constant Strain Energy Release Rate Test for Adhesion", *Journal of adhesion*, 33, pp. 253-272.

40. Liechti, K. M., and Shirani, A. (1994), "Large Scale Yielding in Blister Specimens", *International Journal of Fracture*, 67, pp. 21-36.

41. Shirani, A., and Liechti, K. M. (1998), "A Calibrated Fracture Process Zone Model for Thin Film Blistering", *International Journal of Fracture*, 93, pp. 281-314.

42. Xu, D., and Liechti, K. M., A Closed Form Analysis of the Peninsula Blister Test, *Journal of Adhesion* (in press).

43. De Lumley Woodyear, T. H. (2001), "A Critical Analysis of the Peninsula Blister for Thin Film Adhesion", *Research Center for the Mechanics of Solids, Structures & Materials Report CSSM-01/8,* University of Texas at Austin, 2001.

44. Timoshenko, S., and Woinowsky-Kreiger, S. (1987), "Theory of Plates and Shells", McGraw-Hill, New York, 2nd Edition.

45. Bathe, K. J. (1996), "Finite Element Procedures", Prentice-Hall, Inc., New Jersey.

46. Park, S. J., Liechti, K. M., and Roy, S. (2004), "Simplified Bulk Experiments and Hygrothermal Nonlinear Viscoelasticity", *Mechanics of Time Dependent Materials*, 8, pp. 303-344.

47. Knauss, W. G., and Emri, I. (1987), "Volume Change and the Nonlinear Thermo-Viscoelastic Constitution of Polymers", *Polymer Engineering and Science*, 27, pp. 86-100.

48. Popelar, C. F., and Liechti, K. M. (2003), "A Distortion-Modified Free Volume Theory for Nonlinear Viscoelastic Behavior", *Journal of Time-Dependent Materials*, 7(2), pp. 89-141.

49. Schapery, R. A. (1984), "Correspondence Principles and a Generalized J Integral for Large Deformation and Fracture Analysis of Viscoelastic Media", *International Journal of Fracture*, 25, pp. 195-223

50. Gantes, J. C., Pnevmatikos, G. N. (2004), "Elastic-plastic response spectra for exponential blast loading", *International Journal of Impact Engineering*, 30, pp. 323-343.

51. Prendergast, J. (1995), "Oklahoma City Aftermath", *Civil Engineering*, October, New York, pp.42-45.

52. Sozen, M. A., Thornton, C. H., Corley, W. E., and Mlakara, P. F. (1998), "The Oklahoma City Bombing: Structure and Mechanisms of the Murrah Building", *ASCE Journal of Performance of Construction Facilities*, 12(3), pp.120-136.

53. Louca, L. A., Punjani, M., and Harding, J. E. (1996), "Non-Linear analysis of Blast Walls and Stiffened Panels Subjected to Hydrocarbon Explosion", *Journal of Construction Steel Research*, 37(2), pp.93-113.

54. Otani, R. K., Krauthammer, T. (1997), "Assessment of Reinforcing Details for Blast Containment Structures", *ACI Structure Journal*, 94(2), pp124-132.

55. Houbolt, J. C. (1950), "A Recurrence Matrix Solution for the Dynamic Response of Elastic Aircraft", *Journal of Aerospace Science*, 17, 540.

56. Newmark, N. M. (1959), "A Method of Computation for Structural Dynamics", *Journal of Engineering Mechanics*, 85, 67-94.

57. Wilson, E. L. (1968), "A Computer Program for Dynamic Stress Analysis of Underground Structures", *SESM*, Univ. California, Berkeley.

58. Hilber, H. M., Hughes, T. J. R. and Taylor, R. L. (1977), "Improved Numerical Dissipation for Time Integration Algorithms in Structural Dynamics", *Earthquake Engineering and Structural Dynamics*, 5, pp. 283-292.

59. Low, H. Y., Hao, H. (2001), "Reliability analysis of reinforced concrete slabs under explosive loading", *Structural Safety*, 23, pp. 157-178.

60. Xue, Z. Y., Hutchinson, J. W. (2003), "Preliminary assessment of sandwich plates subject to blast loads", *International Journal of Mechanical Science*, 45, pp. 687-705.

61. Owen, D. R. J., Hinton, E. (1980), "Finite Elements in Plasticity", Pineridge Press Limited, Swansea, U. K.

62. Kreyszig, E. (1983), "Advanced Engineering Mathematics", 5th ed., John Wiley, New York.

VITA

Yong Wang

Candidate for the Degree of

Doctor of Philosophy

Thesis: A COUPLED HYGROTHERMAL COHESIVE LAYER MODEL FOR SIMULATING DEBOND GROWTH IN BIMATERIAL INTERFACE

Major Field: Mechanical Engineering

Biographical:

Personal Data: Born in Luzhou, Sichuan Province, China, on November, 18, 1963, the son of Xuewen Wang and Qiongbin Yang.

Education: Graduated from Second High School, Luzhou, Sichuan, China in June, 1981. Received Bachelor of Science degree in Mechanical Engineering from Tsinghua University, Beijing, China in June,1986. Received Master of Science degree in Engineering Mechanics from Tsinghua University, Beijing, China in December, 1989. Completed the requirements for the Doctor of Philosophy degree with a major in Mechanical Engineering at Oklahoma State University, Stillwater, Oklahoma, in July, 2006.

Experience: Faculty of Department of Bridge and Structural Engineering, Chongqing Jiaotong University, Chongqing, China, December, 1989 – January, 2001. Graduate research assistant in School of Mechanical and Aerospace Engineering, Oklahoma State University, Stillwater, Oklahoma, August, 2002 – July, 2006.

Professional Membership: American Society of Mechanical Engineer